University of Southampton

Faculty of Engineering and Physical Sciences

Electronic and Computer Science

Waveguide Integrated Metasurfaces for On-Chip Vortex Beam Generation

By

Jianzhi Huang

ORCID 0009-0009-2156-9064

Thesis for the degree of Doctor of Philosophy

Oct 2024

University of Southampton

Abstract

Faculty of Engineering and Physical Sciences

Electronic and Computer Science

Doctor of Philosophy

Waveguide Integrated Metasurfaces for On-Chip Vortex Beam Generation

by

Jianzhi Huang

Optical orbital angular momentum (OAM) is a property of light that describes the rotation of its electromagnetic field as it travels through space. Light with OAM, also known as a vortex beam, exhibits a helical phase front and often a doughnut-shaped intensity distribution. Based on these properties, OAM has garnered much attention in areas such as optical sensing, optical communication, optical tweezers, quantum information processing, and imaging. On the other hand, metasurfaces, which are ultrathin layers of judiciously designed nanostructures, possess impressive light manipulation capabilities. This thesis of mine presents two methods of using metasurfaces to generate optical vortex beams, one based on phase gradient manipulation and the other based on amplitude gradient manipulation.

For the phase gradient manipulation, I have proposed and analysed a novel hybridisation approach of metasurfaces and microring resonators. This hybridisation approach allows for nanostructure-based OAM tuning, which is a new tuning method for control the topological charge of microring resonators. It allows a single device to generate identical or two completely different sets of OAM values by only switching the input mode direction. The work further presents an OAM spectrum sorting method to analyse the electromagnetic field of a vector vortex beam.

For the amplitude gradient manipulation, a novel metasurface design approach is proposed for extracting a guided THz wave into free space and shaping its wavefront. By compensating the energy decay in the guided mode, this approach allows for positioning many meta-atoms along a single waveguide, as demonstrated in several 100- and 1000-unit devices. Three different off-chip wavefront shaping functionalities are consequently demonstrated: (1) the generation of a plane wave, where the beam width can reach $275\lambda_0$, equivalently a factor above 900 in width expansion; (2) the generation of a Bessel-beam focus with a FWHM of $0.59\lambda_0$; (3) the generation of OAM-carrying vortex beams, where the topological charge can be tuned from -5 to -30.

In addition to these two pieces of theoretical work, I have also fabricated several types of nanophotonic devices. The first device is a conventional integrated vortex beam generator. I have solved the problems of mask misalignment and undefined small gaps. The second device is an enlarged grating coupler that can reduce the difficulty of chip-fibre alignment and can simplify the fabrication process. The last device is a set of transmissive metasurfaces for OAM emissions. All these devices can be used for experimentally testing the generation of vortex beams in the future.

Table of Contents

Table of Tables

Table of Figures

List of Publications

Conference Publication:

[1] Siyu Chen, Milan Milosevic, Jianzhi Huang, Harold Chong and Xu Fang 'Waveguide-based metasurfaces for light focusing and beam deflection.' *ICNN 2022: International Conference on Nano-photonics and Nano-optoelectronics, Yokohama, Japan*. 18 - 22 Apr 2022. 1 pp.

[2] Jianzhi Huang, Wangke Yu, Zihang Zheng, Jize Yan and Xu Fang. "Metasurface-integrated microring resonators for off-chip vortex beam generation." *Nanophotonics and Micro/Nano Optics IX*. Vol. 12773. SPIE, 2023.

Journal Publication:

[1] Wen Lyu*, Jianzhi Huang*, Shengqi Yin, Xukang Wang, Jiaming Liu, Xu Fang and Hua Geng "Amplitude gradient-based metasurfaces for off-chip terahertz wavefront shaping." *Photonics Research* 11.9 (2023): 1542-1552.

[2] Jianzhi Huang*, Wangke Yu*, Hailong Pi, Yin Shen, Jize Yan and Xu Fang "Asymmetric vortex beam emission from a metasurface-integrated microring with broken conjugate symmetry." *Optics Express* 31.25 (2023): 42549-42561.

[3] Siyu Chen, Jianzhi Huang, Shengqi Yin, Milan M. Milosevic, Hailong Pi, Jize Yan, Harold M.H. Chong and Xu Fang. "Metasurfaces integrated with a single-mode waveguide array for off-chip wavefront shaping." *Optics Express*, 2023, 31(10): 15876-15887.

* The authors claimed that they have equal contribution to this work.

Research Thesis: Declaration of Authorship

Print name: Jianzhi Huang

Title of thesis: Waveguide Integrated Metasurfaces for On-Chip Vortex Beam Generation

I declare that this thesis and the work presented in it are my own and has been generated by me as the result of my own original research.

I confirm that:

1. This work was done wholly or mainly while in candidature for a research degree at this University;
2. Where any part of this thesis has previously been submitted for a degree or any other qualification at this University or any other institution, this has been clearly stated;
3. Where I have consulted the published work of others, this is always clearly attributed;
4. Where I have quoted from the work of others, the source is always given. With the exception of such quotations, this thesis is entirely my own work;
5. I have acknowledged all main sources of help;
6. Where the thesis is based on work done by myself jointly with others, I have made clear exactly what was done by others and what I have contributed myself;
7. Parts of this work have been published as journal papers and conference contributions in the List of Publications.

Signature: Date:

Acknowledgements

I would like to express my deepest appreciation to my supervisors, Dr. Xu Fang, Prof. Harold H.M. Chong, Dr. Hailong Pi, and Dr. Milan Milosevic. Dr. Xu Fang offered me endless guidance and provided me with valuable opportunities. Without his help, the work in this thesis can never be accomplished. Prof. Harold H.M. Chong, Dr. Hailong Pi, and Dr. Milan Milosevic, their invaluable insights about designing photonic devices, relentless support, and practical suggestions assisted me in reaching my goals, which cannot be underestimated.

I would also like to extend my deepest gratitude to my co-workers, Dr. Wangke Yu and Dr. Wen Lyu. Collaborating with them on projects has significantly broaden my knowledge. Their expertise and dedication contributed greatly to the success of our work together.

Additionally, I am grateful to my seniors, Dr. Shengqi Yin, Dr. Fei He, and Dr. Yue Fan, who generously shared their experience with me, not only in the academic area but also in adapting to live in Southampton.

I am also grateful to Prof. Jize Yan and his PhD student Sun Chuang, who give me loads of suggestions and help with nanofabrication.

I also want to thank the technicians in the SNC, TRC, and IPC cleanrooms, Dr. Owain Clark, Dr. Kiang Kian Shen, Dr. Anushka Gangnaik, Dr. Libe Arzubiaga Totorika, Dr. Ying Tran, and Xiangjun Wang, for their training and ongoing support in nanofabrication using the cleanroom facilities.

Many thanks to my flatmates, Tongjun Zhang, Yihong Wu, and Dongkai Guo, who I spent most time with, they provided me with a lot of support, especially during the pandemic period.

I very much appreciate my friends, Tianyi Gao, Jiale Zeng, Zibo Yan, Bohao Ding, Bingkai Ding, Yaxin Zhan, Ruixiao Zhang, Weilin Jin, Zihang Zheng, Yuxin Du, Siyu Chen, Wenjie Wang, and Jiapei Zhang. Their presence has enriched my life excessively over the past four years, making it enjoyable and memorable.

Finally, I want to express my sincere gratitude to my entire family. From the moment I was born, they have consistently shown me unconditional love and support, helping me grow into a strong and confident individual. Their unwavering presence and encouragement have been instrumental shaped me into who I am today. Thank you, from the depths of my heart, for everything you have done for me.

Definitions and Abbreviations

BIC ..... Bound state in the continuum

BOX ..... Buried oxide

EBL ..... Electron beam lithography

FDTD ..... Finite-difference time-domain

FP ..... Fabry-Pérot

FSR ..... Free-spectral range

FWHM ..... Full width at the half maximum

ICP ..... Inductively coupled plasma

LG ..... Laguerre-Gaussian

LHCP ..... Left-handed circularly polarised

LiDAR ..... Light detection and ranging

MDM ..... mode-division-multiplexing

NA ..... Numerical aperture

NMP 1-methyl-2-pyrrolidone

OAM ..... Orbital angular momentum

PB ..... Pancharatnam-Berry

PECVD ..... Plasma-enhanced chemical vapour deposition

RHCP ..... Right-handed circularly polarised

RIE ..... Reactive ion etching

SAM ..... Spin angular momentum

SEM ..... Scanning electron microscopy

SOI ..... Silicon-on-insulator

STED ..... Stimulated Emission Depletion

TC ..... Topological charge

TE ..... Transverse electric

TEM ..... Transverse electromagnetic

THz ..... Terahertz

TM ..... Transverse magnetic

WGM ..... Whispering gallery mode

Chapter 1 Introduction to thesis structure

1.1 Introduction

Optical orbital angular momentum (OAM) is a property of light that describes the rotation of its electromagnetic field as it travels through space. Light with OAM, known as a vortex beam, exhibits a helical phase front and often a doughnut-shaped intensity distribution. Since OAM was measured and defined in 1992, this area has attracted tremendous interest from researchers in various fields [1]. Compared to spin angular momentum (SAM), OAM offers the advantage of possessing infinite and orthogonal states. This property provides an additional degree of freedom for a light beam, as beams with different OAM states can be utilised as independent channels for data transmission in wireless communication. Consequently, OAM is useful in a range of applications, from free-space optical components to integrated devices. Vortex beams can exhibit polarisation-varying patterns based on the generating methods, referred to as vector vortex beams. These beams contain additional polarisation information beyond conventional OAM states. Vector vortex beams have garnered significant attention in areas such as optical sensing, optical communication, optical tweezers, quantum information processing, and imaging.

In parallel, a metasurface, an ultra-thin layer of subwavelength structures, can manipulate the properties of light, including intensity, phase polarisation, and OAM. Compared to conventional bulky optical devices, metasurfaces offer greater potential to integrate optical components. With their impressive flexibility in manipulating light, metasurfaces have become a prevailing research area for scientists. It has been explored in various applications, such as beam deflectors, beam splitters, metalenses, mode converters, and metasurface holograms.

Nowadays, the utilisation of metasurfaces to generate vortex beams remains prevalent [2, 3]. However, simply employing metasurfaces for vortex beam generation has limitations, as the emitted beam from a fabricated device may not cover a wide range of topological charge manipulations. To address this challenge, integrated microring vortex beam emitters were initially proposed in 2012 [4]. These emitters enable manipulations of the topological charge by adjusting the input mode wavelength. In this thesis, I propose placing metasurfaces on top of microring resonators for vortex beam generation. To the best of our knowledge, this metasurface-based microring emitter has not been discussed previously. With the assistance of metasurfaces, the emitted vortex beam exhibits an intrinsic phase change, which overcomes the symmetry limitation observed in conventional microring vortex beam emitters. This approach introduces a novel method to control the OAM states of the emitted beam. Additionally, I explore

the use of metasurfaces to manipulate the intensity of the emitted beam on a microring-like waveguide in the THz frequency range. This manipulation facilitates three different wavefront shaping techniques: beam expansion, light focusing lens, and vortex beam generation.

1.2 Overview

The contents of each following chapter are summarized below. In Chapter 2, the characteristics of optical vortex beams, metasurfaces, silicon waveguides, and silicon microring resonators are discussed. This chapter also introduces analyses of scalar Laguerre-Gaussian mode and vector vortex beams. Chapter 3 presents the first demonstration of a metasurface-based microring emitter for vortex beam generation. An analytical method for analysing the purity of the emitted light based on Laguerre-Gaussian mode decomposition is proposed. Chapter 4 proposes a novel amplitude-gradient-oriented design approach, enabling both a large device aperture and advanced off-chip wavefront shaping in the THz regime. Chapter 5 demonstrates a metasurface device for vortex beam generation. Chapter 6 summarises the main achievements of my PhD study and suggests future work that can be derived from this research.

Chapter 2 Background and demonstrations of concepts

This thesis introduces two novel devices that focus on metasurface-decorated microring resonators designed for on-chip vortex beam generation. Consequently, this chapter presents four key concepts relevant to this topic: optical vortex beams, metasurfaces, silicon waveguides, and silicon microring resonators.

2.1 Optical Vortex beam

Unlike traditional light beams with planar wavefronts, a vortex beam is characterised by a helical wavefront. As it propagates, the vortex beam twists around a central axis, imparting a phase singularity at its centre in the transverse field. This singularity occurs because the vortex beam carries orbital angular momentum (OAM). The following section provides an introduction to OAM, explores its applications, and discusses methods for generating it. Given that I am employing microring resonators for vortex beam generation, a detailed discussion of the emitted beam is provided in the following part.

2.1.1 Orbital angular momentum

In both classical mechanics and quantum mechanics, OAM is a type of angular momentum. The concept of angular momentum was first observed by Beth RA et al. in 1936, who noticed its presence when circularly and elliptically polarised light passed through a crystal plate. Then, in 1992, Allen L. et al. successfully generated the OAM experimentally and provided an explanation for it under the paraxial approximation. Since then, research related to OAM has flourished and garnered significant interest. Today, the concept of OAM finds application in various fields and areas, including optical communication, optical tweezers, microscopy, quantum information processing, etc.

2.1.1.1 Orbital angular momentum of a vortex beam

A beam carrying OAM, also called a vortex beam, possesses a helical phase front and typically exhibits a phase singularity along the propagation direction. The Laguerre-Gaussian mode (LG mode) represents one of the simplest forms of a vortex beam. This mode is a solution to the paraxial scalar Helmholtz equation in cylindrical coordinates. Following [5, 6], the scalar Helmholtz equation is given by

$$(\nabla^2 + k^2)E = 0 \tag{2.1}$$

where $k = 2\pi/\lambda$ is the wavenumber. E denotes the electric field, and ∇ represents the three-dimensional gradient operator. The expression of a paraxial solution of electric field in cylindrical coordinates is given by:

$$E(\rho, \varphi, z, t) = u(\rho, \varphi, z)\exp\left[i(kz - \omega t)\right] \tag{2.2}$$

where $u(\rho, \varphi, z)$ is the amplitude distribution, and ω is the angular frequency. Substituting this equation into the scalar Helmholtz equation yields:

$$\nabla^2 u + \frac{\partial^2}{\partial z^2}u + 2ik\frac{\partial}{\partial z}u = 0 \tag{2.3}$$

Assuming the profile of beams changes only slowly in the z direction, these two approximations can be used:

$$\frac{\partial^2 u}{\partial z^2} \ll \nabla^2 u, \qquad \frac{\partial^2 u}{\partial z^2} \ll \frac{\partial u}{\partial z} \tag{2.4}$$

Therefore, Eq. 2.3 can be approximated to

$$\frac{1}{\rho}\frac{\partial}{\partial \rho}\left(\rho\frac{\partial u}{\partial \rho}\right) + \frac{1}{\rho^2}\frac{\partial^2 u}{\partial \varphi^2} + 2ik\frac{\partial u}{\partial z} = 0 \tag{2.5}$$

Based on this equation, the Laguerre-Gaussian modes LG_p^l can be derived as:

$$\begin{aligned} LG_p^l &= u_p^l(\rho, \varphi, z) \\ &= \sqrt{\frac{2p!}{\pi(p+|l|)!}}\frac{1}{w(z)}\left[\frac{\rho\sqrt{2}}{w(z)}\right]^{|l|} exp\left[\frac{-\rho^2}{w^2(z)}\right] L_p^{|l|}\left(\frac{2\rho^2}{w^2(z)}\right)\exp[il\varphi] \\ &\cdot exp\left[\frac{-ik\rho^2 z}{2(z^2 + z_R^2)}\right] exp\left[-i(2p + |l| + 1)tan^{-1}(\frac{z}{z_R})\right] \end{aligned} \tag{2.6}$$

where $w(z) = w(0)[(z^2 + z_R^2)/z_R^2]^{1/2}$ is the $1/e$ radius of the Gaussian term. Here, $w(0)$ is the beam width and z_R is the Rayleigh range. $L_p^{|l|}$ represents the generalised Laguerre polynomials. The term $(2p + |l| + 1)tan^{-1}(\frac{z}{z_R})$ is the Gouy phase. Two key parameters determine the LG mode profiles: p and l. p determines the number of concentric rings in the intensity distribution. While l is relates to the azimuthal phase term $\exp[il\varphi]$, indicating how many times the helical wavefront twists along the optical axis. Figure 2.1 illustrates corresponding electric field and phase distributions of different LG modes. The integer l is referred to as the topological charge (TC).

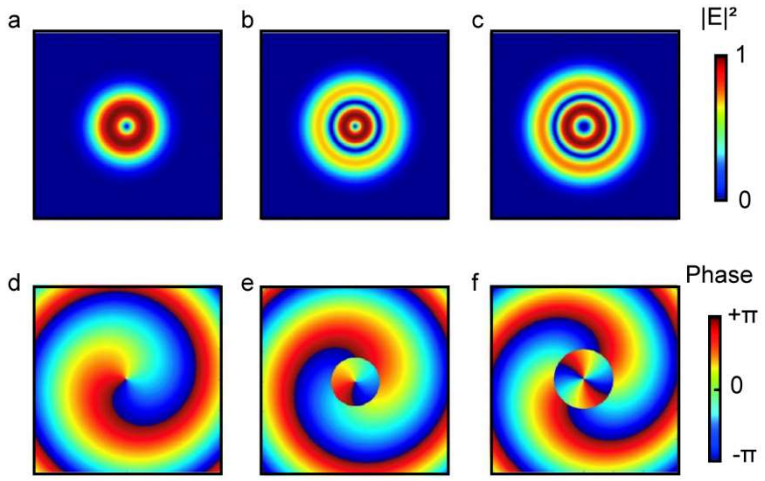

Figure 2.1 Electric field distributions of LG modes. (a-c) The intensity profile of different LG modes. (d-f) The azimuthal phase profile of different LG modes. (a) and (d) is LG_0^1. (b) and (e) is LG_1^1. (c) and (f) is LG_1^2, modified figures from [6].

2.1.2 Applications of OAM

Due to its unbounded orthogonal states and doughnut-shaped field distribution, OAM finds widespread application in various fields, including optical communication, optical tweezers, microscopy, and quantum information processing.

2.1.2.1 Optical communication

Because OAM has intrinsically orthogonal and unbounded states, it adds another degree of freedom to increase communication capacity, in addition to the phase, intensity, and polarisation of a beam. In Ref. [7], the authors demonstrated an application of OAM in long-distance communication. OAM modes transmitted over $143\ km$ achieved, as illustrated in Figure 2.2.(a). The author also developed an algorithm that was able to distinguish different mode superpositions up to the third order with more than 80% accuracy and decode the transmitted message with an error rate of 8.33%. However, while promising, this work may not be sufficient for real-life applications. This is because conventional OAM beams have the disadvantage of enlarging beam size along the propagation direction, particularly for large topological charges. This enlargement complicated beam capture at the receiver side and led to a decreased intensity within the effective area due to light divergence. Furthermore, it raises the difficulty when OAM is subject to turbulence. To overcome these issues, Ref. [8] considered restructuring the OAM beam to reduce the light divergence.

2.1.2.2 Optical tweezer

Optical tweezers are a powerful technique used to trap and manipulate microscopic particles or biological specimens using a single, tightly focused laser beam. The trapping range of a single beam is determined by the spot size of the Gaussian beam. This trapping range serves as a crucial parameter in the design of optical tweezers. While it may seem intuitive to increase the trapping range by enlarging the spot size directly, this approach has limitations. A larger spot size leads to a decrease in the intensity gradient, potentially disrupting the steady trapping condition. Hence, it is essential to find methods to enlarge the trapping range while maintaining the stability of single-beam optical tweezers [9]. Using a vortex beam has proven to be an effective solution to this challenge. The reason is that a vortex beam carries OAM and has a doughnut-shaped intensity distribution. The gradient force acting on the doughnut-shaped intensity can trap particles, while the OAM induces particle rotation through the formation of optical spanner action [9, 10], as illustrated in Figure 2.2.(b). Consequently, we can control the trapping range by changing the OAM states.

2.1.2.3 Microscopy

In classical optical microscopy, resolution is constrained by diffraction, approximately determined by the formula $\lambda/(2 \times NA)$, where λ is the free-space wavelength and NA is the numerical aperture of the microscopic objective. To overcome this limitation, numerous super-resolution imaging systems have been developed. One successful example is stimulated emission depletion (STED) microscopy. STED microscopy achieves high spatial resolution, with a value as low as $20\ nm$ [11], by utilising vortex beams as depletion beams [Figure 2.2.(c)]. In this technique, the sample is initially illuminated with an excitation laser beam for fluorescence emission. Subsequently, a vortex beam is employed to deplete the excited state of the fluorophores, forcing them back to the ground state in the undesirable region. By controlling the size of the dark centre of the vortex beam, the effective excitation area of the sample is reduced, leading to improved resolution [12, 13].

2.1.2.4 Quantum information processing

Quantum information processing involves utilising fundamental quantum theories for information processing. Photons, compared to electrons, offer an effective system for processing information due to their fast propagation, minimal interaction with the environment, and ease of manipulation. In quantum information processing, OAM plays a crucial role by introducing another degree of freedom to the quantum bit (qubit), in addition to polarisation, number, and time. OAM values can span from negative infinity to positive infinity, and distinct OAM states are mutually orthogonal. This property provides an important practical advantage because it allows

for reducing the required number of photons in a process, thereby significantly reducing noise and losses arising from imperfect generation and detection efficiency [14, 15].

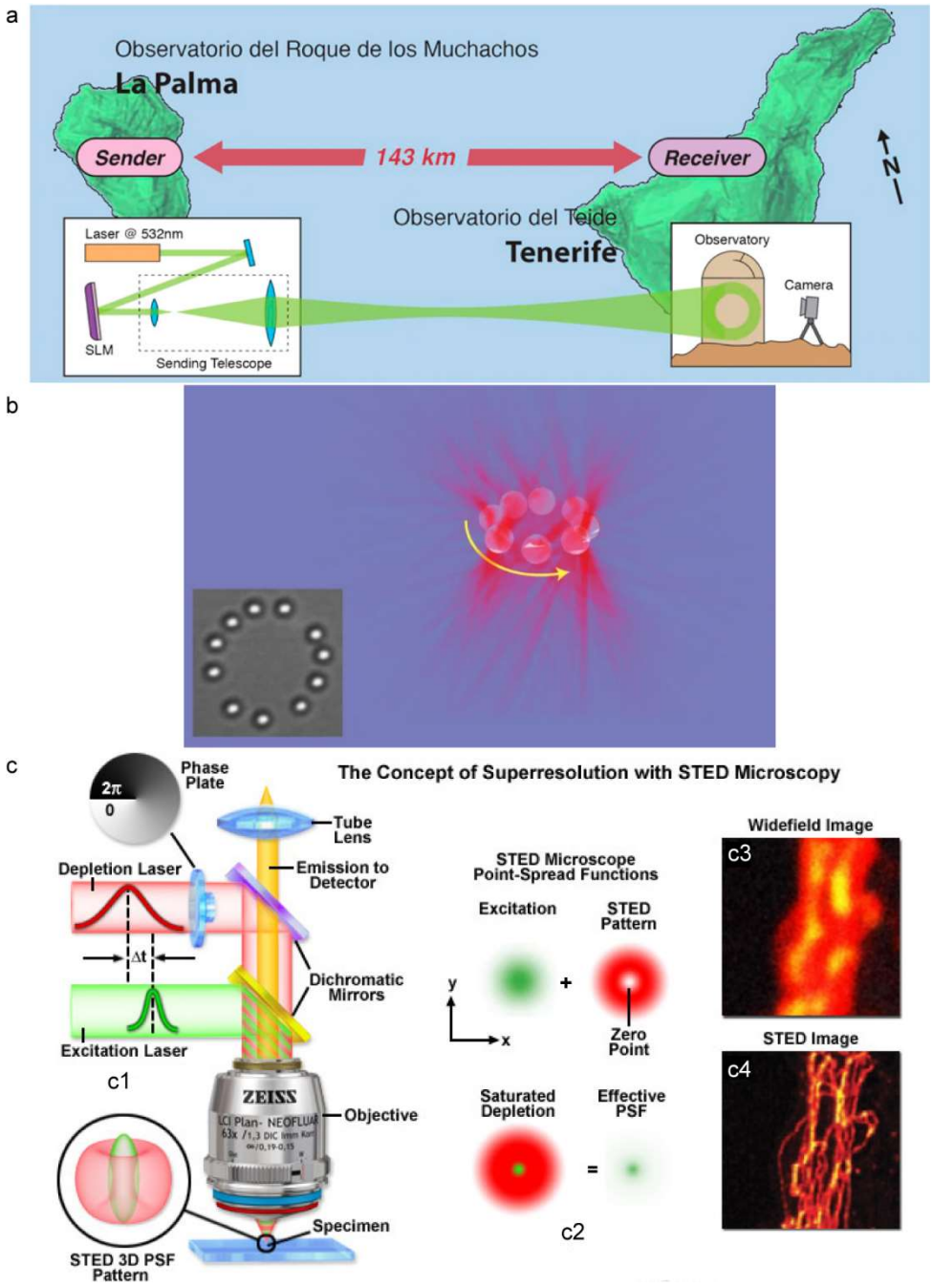

Figure 2.2 Demonstrations of OAM applications. (a) Sketch about using OAM for optical communication: the light is magnified with a sending telescope and sent over $143\ km$ to the receiver [7]. (b) A micrograph related to using OAM as an optical tweezer to trap particles. The scattering force drives particles around the ring of the vortex beam [16]. (c) Illustration of a STED microscopy device from ZEISS [17]. (c1) Depict how a vortex beam is utilised in a STED system. (c2) Demonstration of the reduced effective excitation area of the beam. (c3) and (c4) are the comparisons of widefield and STED images of microtubules.

2.1.3 Generation of vortex beam

Given the significant potential of OAM discussed above, numerous methods are designed for generating vortex beams. These methods vary depending on the specific application, the desired OAM states, and the characteristics of the incident light.

2.1.3.1 Spiral Phase Plate

For example, the spiral phase plate is a straight-forward method to generate vortex beam[18, 19]. It uses bulk material with a fixed refractive index and a variable thickness, as illustrated in Figure 2.3. The height difference increases as the topological charge of the emitted vortex beam rises. However, it's challenging to use them for generating vortex beams with high-frequency waves, and the continuous modulation for different OAM eigenmodes is yet to be achieved.

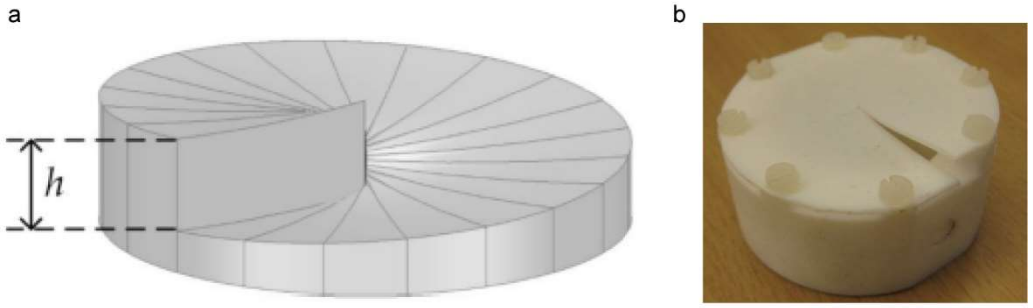

Figure 2.3 Vortex beam generation by spiral phase plates. (a) The schematic design of a spiral phase plate operating at 60 GHz in [19]. (b) Image of a practical model of a spiral phase plate [18].

2.1.3.2 Diffraction grating

Another method for producing a vortex beam is through the use of a diffraction grating, as demonstrated in Ref. [18]. This kind of grating, known as a holographic plate, is illustrated in Figure 2.4.(a). It consists of parallel slits or lines arranged in a flower-shaped pattern at the centre. When light hits the surface of the grating, it will be diffracted by the grating, resulting in the generation of multiple beams in different directions. A vortex beam can be visualised within the interference pattern formed by the combination of diffracted beams and incident beams.

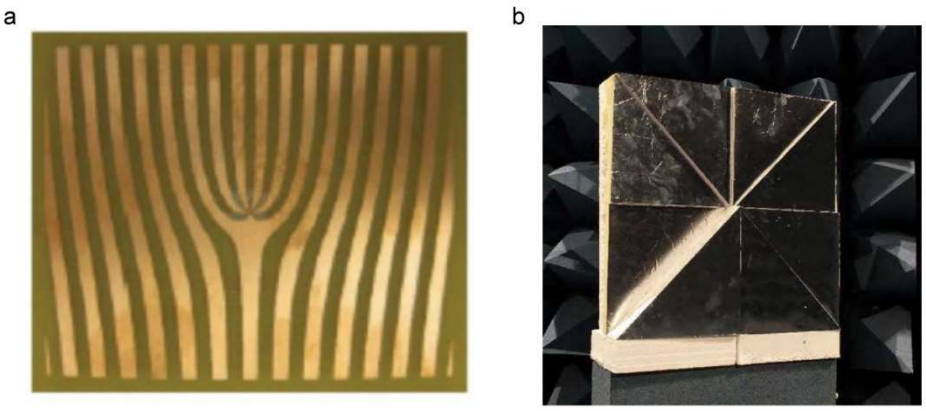

Figure 2.4 Vortex beam generation by gratings and reflectors. (a) Holographic plate for vortex beam generation [18]. (b) The spiral reflector, which generates a vortex beam by reflection, was made from Styrofoam blocks, trimmed into a staircase-like structure with eight steps [20].

The reflection of a light beam can also serve as a method for generating a vortex beam. A discrete eight-step staircase phase mask, as depicted in Figure 2.4.(b), can introduce a non-focused 2π phase shift to the incident beam.

However, these conventional methods typically involve the use of bulk optical materials, which can be impractical for commercial uses because it is challenging to integrate them with other devices: requiring a long propagating path for integration.

2.1.3.3 Metasurfaces

Metasurfaces, defined as thin layers of subwavelength structures for manipulating optical behaviours, are thoroughly discussed in Section 2.2. Given their remarkable capability for light manipulation, researchers have utilised them for vortex beam generation. Depending on the light propagation path, they can be categorised into two main groups: reflective metasurfaces [21, 22] and transmissive metasurfaces [23-28].

In Ref. [22], a reflective metasurface is designed for vortex beam generation. Each super-unit cell contains three dipoles, with a 2π phase-change coverage achieved by adjusting both the length of each dipole and the distance between adjacent dipoles. Using a configuration of 20×20 unit cells, a vortex beam with $l = 2$, was generated at $5.8\ GHz$, as illustrated in Figure 2.5.(a). Comparatively, the Pancharatnam-Berry (PB) phase is simpler to implement. PB metasurfaces can convert spin angular momentum (SAM) to OAM. A detailed discussion of the PB phase is provided in Section 2.2.1. for vortex beam generation. Figure 2.5.(b) depicts an application of a reflective PB-phase metasurface [21], consisting of multiple super-unit cells. When the incident circularly polarised terahertz waves are reflected back from the metasurfaces,

the amplitude and phase of the wave are altered. After optimisation, the reflected wave can carry OAM states.

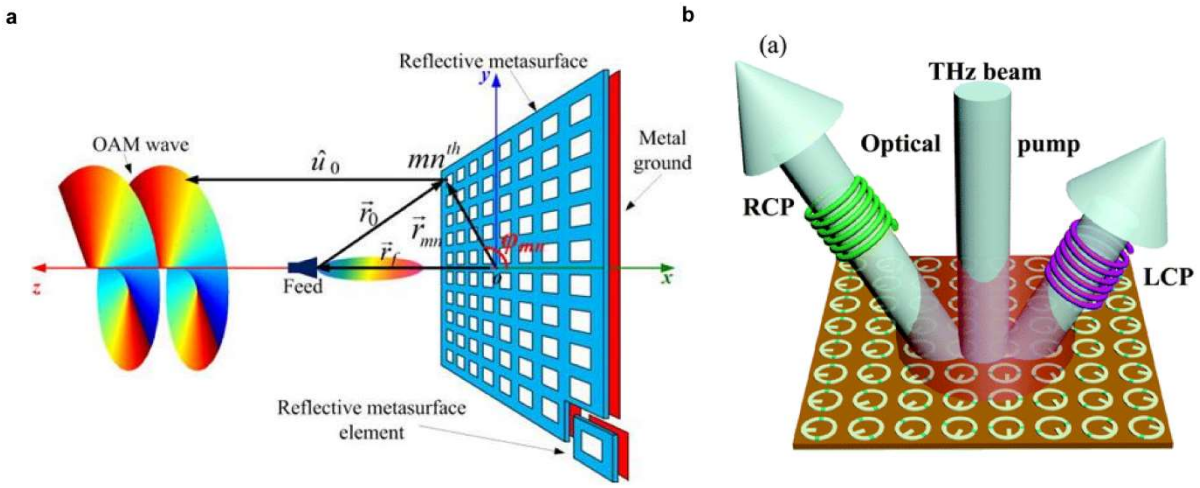

Figure 2.5 Vortex beam generation by reflective metasurfaces. (a) Schematic of the unit structure of a reflective OAM metasurface which is based on propagation phase [22]. (b) Schematic of the optical pumped asymmetrical reflection of circularly polarized terahertz beam realized by the 3-bit Pancharatnam-Berry coding metasurface [21].

Reflective metasurfaces often achieve high working efficiencies, but they commonly face challenges associated with wave interferences, limiting their practicality for certain applications. Transmissive metasurfaces offer a solution to these challenges [23, 27, 28]. Figure 2.6.(a) illustrates a transmissive metasurface device for OAM generation. It uses three layers for each super-unit cell (Figure 2.6.(b)). Each metasurface layer allows for adjustment of amplitude, azimuthal phase, and propagation direction when a linearly polarised wave passes through it. In Figure 2.6.(c) and (d), these two works utilised 'rotated' meta-atoms to generate OAM after the beams passed through the metasurfaces. However, constructing a high-efficiency metasurface in transmission mode requires identifying meta-atoms that are nearly transparent for electromagnetic (EM) waves while providing a full 2π phase-change coverage.

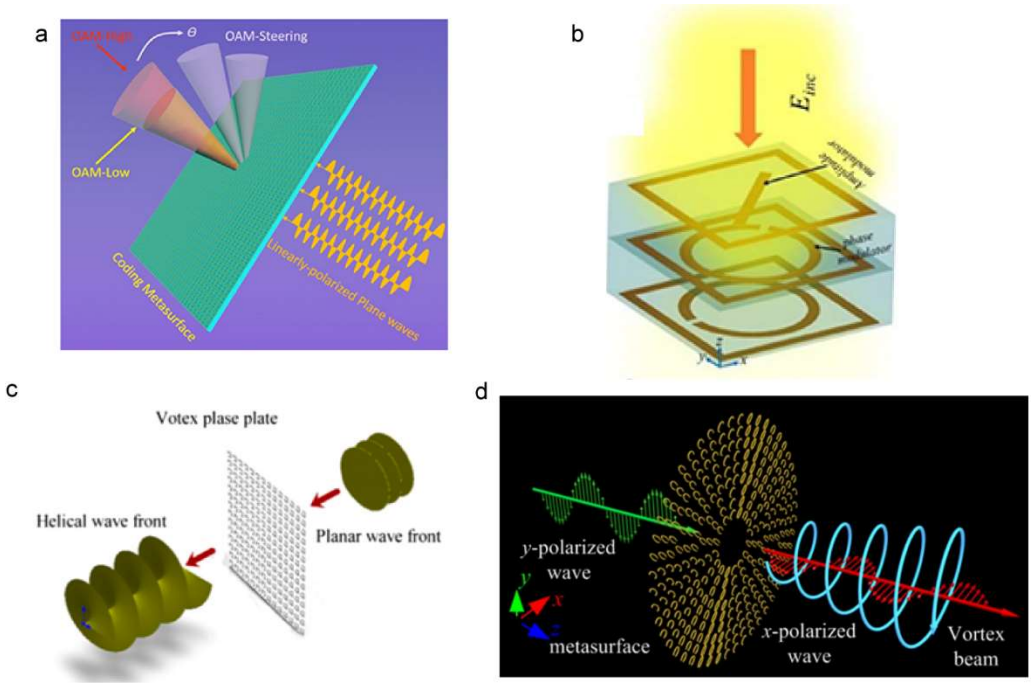

Figure 2.6 Vortex beam generation by transmissive metasurfaces. (a) Schematic illustration of the power modulation of OAM beams by using the designed phase/amplitude adjustable coding metasurfaces. The vortex beam in red and yellow in the axial direction shows two OAM vortex beams with different transmitted powers. The grey-coloured vortex beams show the deflected OAM vortex beams. [23] (b) Schematic view of the coding meta-atoms [23]. (c) Schematic of generation of a helical wavefront from the designed optical vortex phase plate [28]. (d) Schematic diagram for generating the OAM vortex beam using the metasurfaces [27].

2.1.3.4 Integrated emitter

Different from the generating methods discussed previously, utilising ring resonators as vortex beam generators has garnered considerable attention from researchers for three reasons: the scalability of ring resonators to several micrometres, their operation at small incident wavelengths (such as 1550nm), and their ability to achieve continuous modulations of OAM eigenstates by gently shifting the incident wavelength. As this method serves as the primary generation method in this thesis, a detailed discussion is provided below. A detailed discussion about the properties of microring resonators is given in Section 2.4.

The general concept involves arranging scattering elements located on top of the ring resonator based on a circular grating strategy. At a resonance wavelength, a whispering gallery mode (WGM) propagates inside the ring waveguide. Each scattering element then scatters the light into free space. Similar to bending a straight waveguide into a ring waveguide, the concept of the propagation angle of the phase front for the straight waveguide corresponds to a specific topological charge (l) for the azimuthal phase of the vortex beam, as illustrated in Figure 2.7.

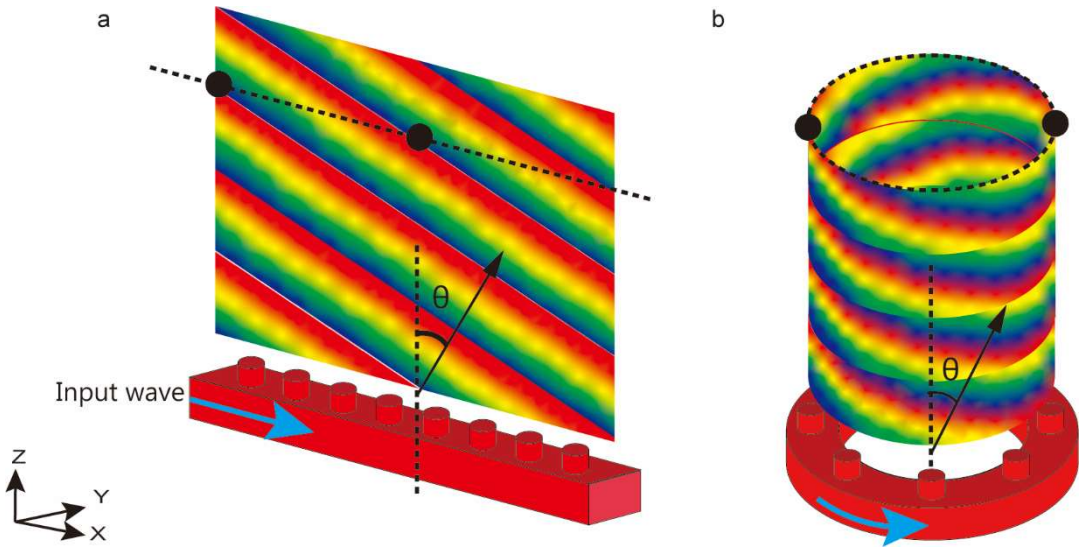

Figure 2.7 Schematic illustration of emitted waves from a strip waveguide and a microring waveguide. (a) Schematic of a strip waveguide with a conventional grating on top. (b) Schematic of a microring vortex beam emitter. For both figures, the patterns on top of the structures represent the phase profiles of the diffracted or emitted beams.

The OAM (l) here is determined by the WGM in the ring waveguide (m) and the number of scattering elements (q):[6, 29, 30]

$$l = \pm(m - gq) \tag{2.7}$$

where g is the diffraction order. The evenly distributed scattering elements pick up the wave from the WGM at where they are positioned, all of them are in the same phase, when $m = gq$. The sign indicates the influence of changing input mode direction, which will be discussed in Chapter 3.1. As a result, the interfered emitted field from all the elements has a uniform phase front, meaning that the OAM is zero. When $m \neq gq$, a phase difference between two adjacent elements is introduced. As shown in Figure 2.7(b), the generated phase front possesses phase shift in the transverse plane, resulting in a finite OAM value.

Numerous articles have conducted thorough analyses of ring-resonator-based vortex beam generators [4, 29, 31-42]. Depending on the positions of the grating elements, they can be classified into two categories. In the first category, the grating elements are placed on the inner side wall of the ring resonator [4, 32, 38, 43] (Figure 2.8.(a)). In the second category, they are placed on top of the ring waveguide [29, 31, 44, 45] (Figure 2.8.(c)). These positions determine the dominant polarisation of scattered light from each element. When the scattered elements are placed on top of the ring resonator, they can be considered as truncated waveguides, and the emitted electric waves have the same polarisation as the WGM inside the ring resonator. On the contrary, elements located on the inner side of the ring resonator can emit light with different polarisations because the cross-section of the ring resonator is not symmetric. As depicted in

Figure 2.8.(b), when the WGMs inside the ring correspond to the quasi-transverse electric mode (TE mode), elements positioned on the inner side of the ring predominantly emit the electric field in the azimuthal direction [43]. Differently, when relocating the grating elements to the top of the microring, the dominant emitted wave is radially polarized [45]. This analysis applies similarly to TM modes as well.

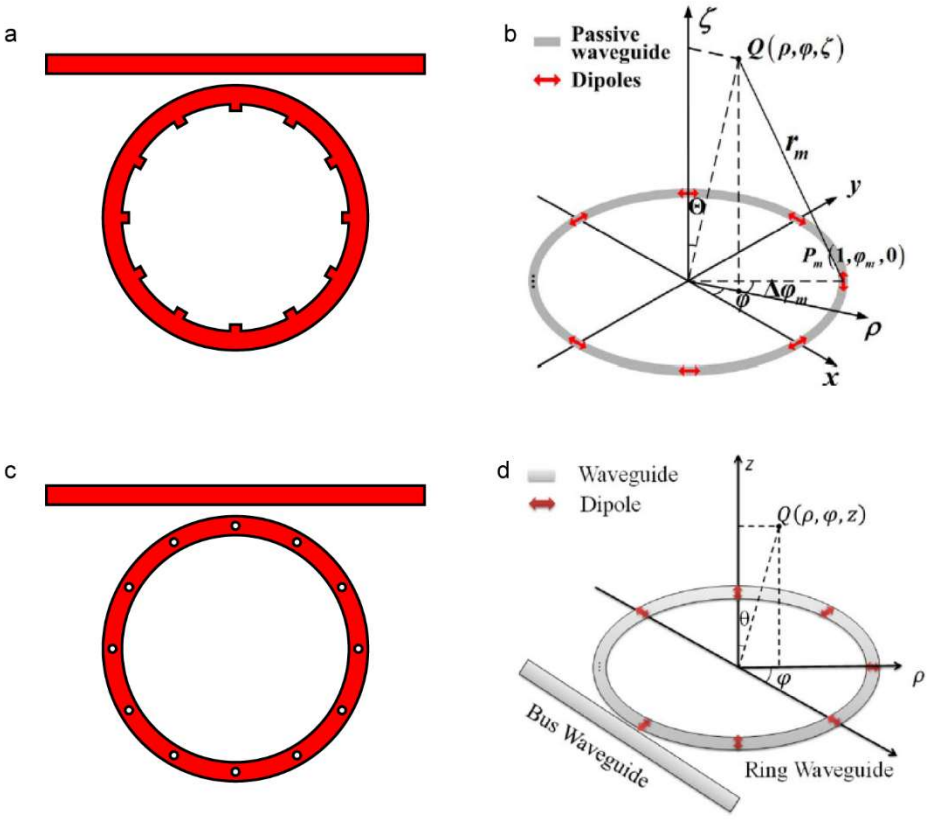

Figure 2.8 Top-down views of two different positions of grating structures on ring waveguide and their corresponding analytical models. (a) Schematic diagram when the scattering elements are placed by the side of the waveguide. (b) Corresponding azimuthal dipoles in the waveguide, which are most easily described in cylindrical coordinates. The dipoles are evenly distributed along the ring with azimuthal polarisation [43]. (c) Schematic diagram when the scattering elements are placed on top of the waveguide. (d) Corresponding dipoles distribution, which has radial polarisation [45]. It is assumed that the input mode is the TE mode in both models.

By simultaneously applying both quasi-TE mode and quasi-TM mode at the input port, such devices can manipulate both polarisations and OAM states by shifting the input wavelength, enabling the generation of both radially and azimuthally polarised vortex beams simultaneously. Since both generated vortex beams are vector vortex beams, the emitted beam is essentially a superposition of the radial vortex beam and the azimuthal vortex beam, which can be described as a point in the higher-order Poincaré sphere. The corresponding polarisation states in the

Poincaré sphere are depicted in Figure 2.9.(c). In this Poincaré sphere, any antipodal points are orthogonal, and every polarisation state in the Poincaré sphere can be expressed by the linear combination of those two points. In Ref. [39, 46], the authors designed higher-order Poincaré sphere beam emitters, as illustrated in Figure 2.9.(a) and (b). By controlling the intensity ratio and phase contrast of the TE and TM modes, all the polarisation states in the higher-order Poincaré sphere can be generated.

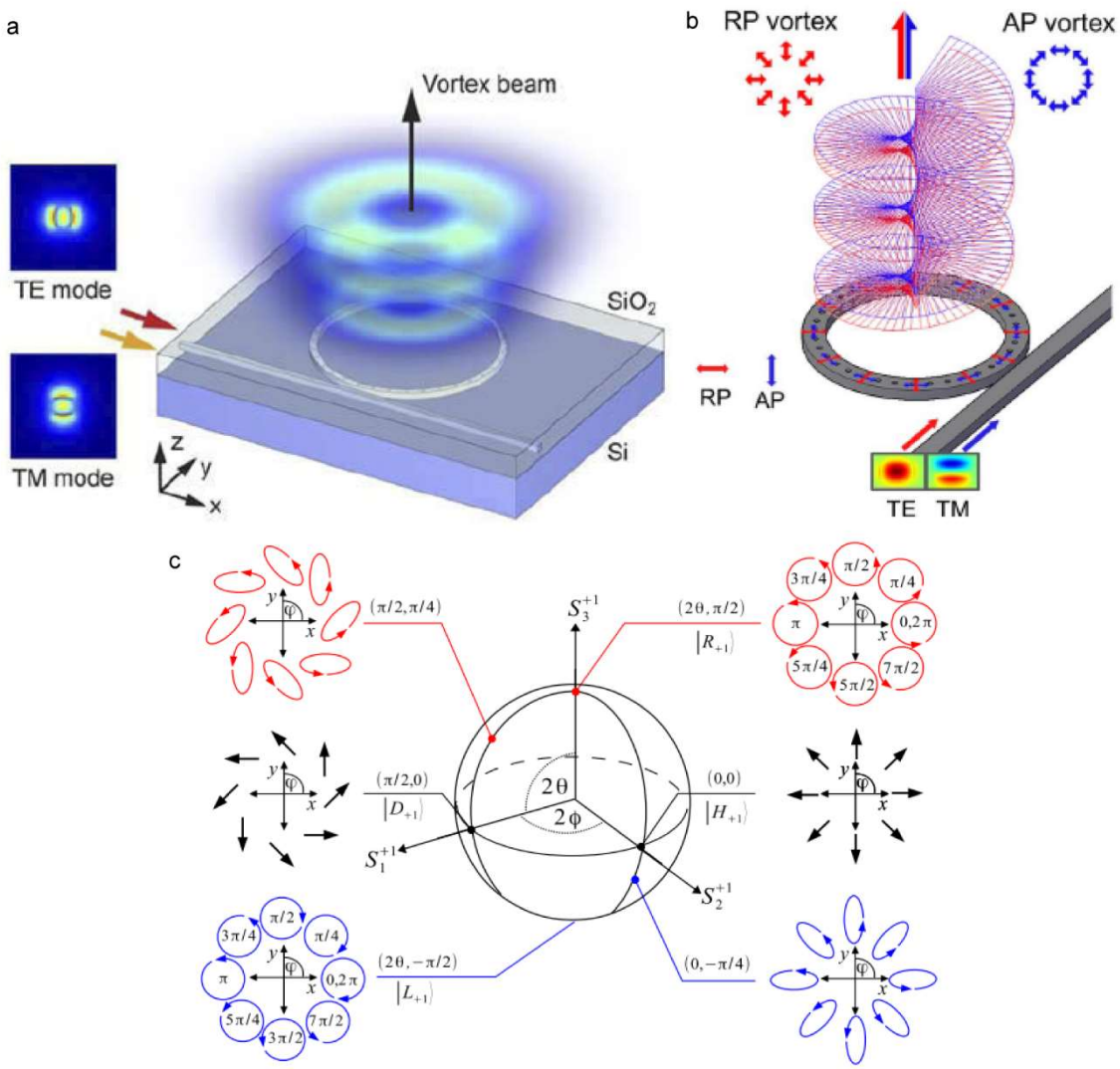

Figure 2.9 Using integrated microring emitter to control the polarization of the emitted beam which can be described in Poincaré sphere. (a) Schematic of a higher-order Poincaré sphere beam emitter, which is illuminated by the fundamental TE mode and fundamental TM mode. The generated radial and azimuthal polarisation can form a pair of eigenstates in the higher-order Poincaré sphere. [46] (b) Another schematic of a higher-order Poincaré sphere beam emitter, while the scattering elements are placed on the inner side of the ring resonator [39]. (c) Poincaré sphere illustration. The poles represent right and left circular polarisation, while the equator represents linear polarisation. The northern and southern hemispheres separate right (red) and

left (blue)-handed ellipticity. Antipodal points are orthogonal, and any state of polarisation is given as their linear combination [47]. It is worth highlighting that, different from the first-order Poincaré sphere where the polarisation is uniform across the beam cross section for any point on the sphere, a higher-order Poincaré sphere does not have such polarisation uniformity.

Although the vortex beam generated from the ring resonator can possess a different OAM value by shifting the incident wavelength, achieving high emission efficiency remains a challenge. To generate a well-defined doughnut beam in the intensity profile, the WGM in the ring should ideally have the same amplitude, resulting in emitted fields from each element having uniform intensity. However, in real cases, when the scattering elements emit the waves into free space, they will introduce attenuation to the WGM. In Figure 2.10.(a) and (b) [45], two numerically simulated results illustrate that when the radiation efficiency of the scattering elements is sufficiently high, the intensity profile degrades, leading to a degraded OAM purity. However, simply reducing the attenuation of the WGM may not always be the better solution. Lower attenuation implies lower emission efficiency, which is not practical for real applications. Therefore, when designing a vortex beam emitter using a ring resonator, considerations of the energy attenuation of the scattering elements are necessary.

As the emission efficiency of the integrated vortex beam emitter is considerably lower than that of metasurfaces and other generating methods, several modification methods are given to enhance the emission efficiency of the conventional integrated vortex beam emitter. The first effective approach is to couple more light into the ring waveguide to enhance the energy of WGM. In Ref. [31, 32, 36], access waveguides were curved for improving coupling efficiency, as illustrated in Figure 2.10. (c) and (d). In Ref. [34], as shown in Figure 2.10.(e), the access waveguide is placed in a different plane than the ring resonator. The results demonstrate that the quality of the generated vortex beam is unaffected by this layout, and it exhibits better coupling efficiency than the side-coupled structure.

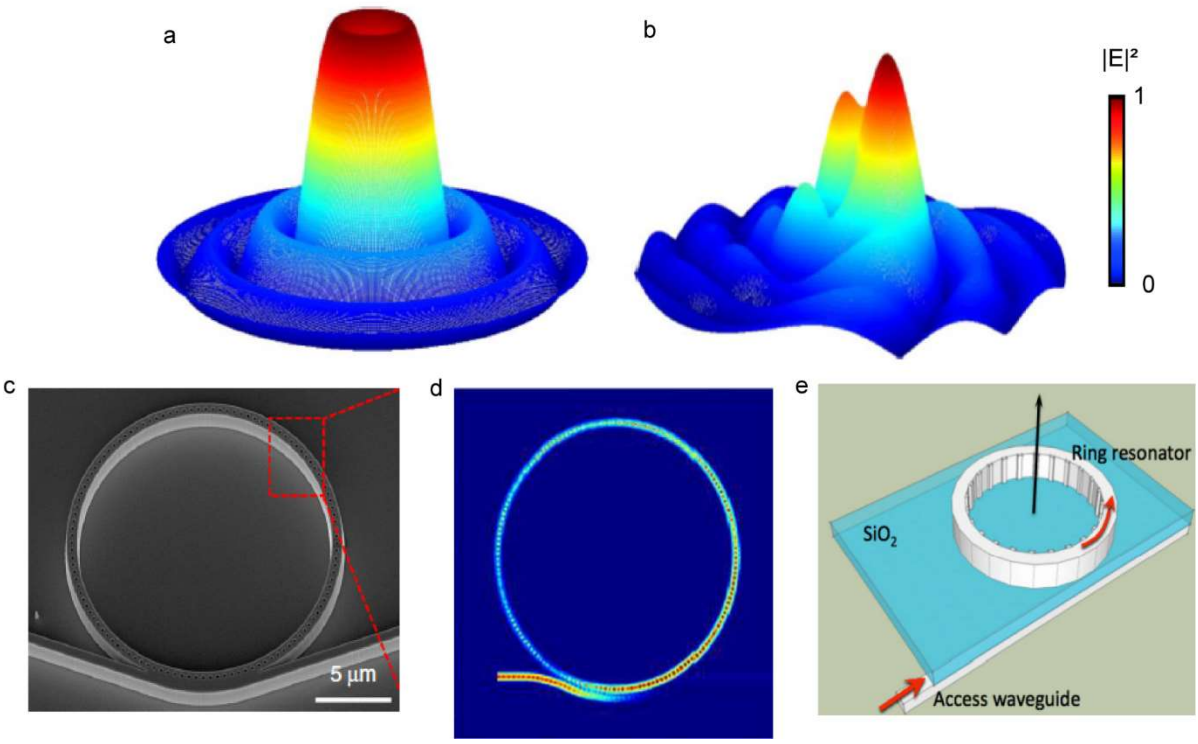

Figure 2.10 Demonstrations of integrated vortex beam generators. (a, b) Simulation results demonstrate the influence of the energy attenuation of each pillar. There are 540 pillars in total [45]. These two maps share the same colour bar, which is nominal to the maximum intensity value in (a). In (a), the energy attenuation is zero, which means each element is illuminated with the same-energy light source. While in (b), the energy attenuation is 0.01. In other words, when the light passes through the scattering elements, only 99% of the light remains. When the light propagates to the last element, there is only 0.44% of light remaining in the underlying waveguide. (c) Schematic of a vortex beam emitter with a curved waveguide for increasing coupling efficiency [31]. (d) Electric field profile of a vortex beam emitter, in which the access waveguide is configured in a so-called "pulley coupling" scheme [36]. (e) Schematic of an integrated ring resonator with a $275\text{-}nm$-thick SiO_2 film between the access waveguide and the ring resonator [34].

The second method involves reducing the appearance of concentric annuli in the far-field profile. In Refs. [29, 32, 34], it was observed that the emitted vortex beams exhibited concentric ring patterns near the original 'doughnut ring'. These additional beams follow the Bessel function and have amplitudes proportional to the lth-order Bessel function of the first kind or to its first derivative [43]. The appearance of these concentric rings, as depicted in Figure 2.11.(b), is attributed to the scattering elements. In the ideal scenario, with extremely well-confined elements, it is possible to obtain a vortex beam with only one value of the topological charge l ($LG_0^{|l|}$). Li S. et al. proposed a new design to address this issue by incorporating an aluminium

layer below the ring resonator, acting as a mirror to concentrate the main lobe of the emitted beams and reduce the intensity of side lobes, as illustrated in Figures 2.11.(a) and 2.11.(b) [43].

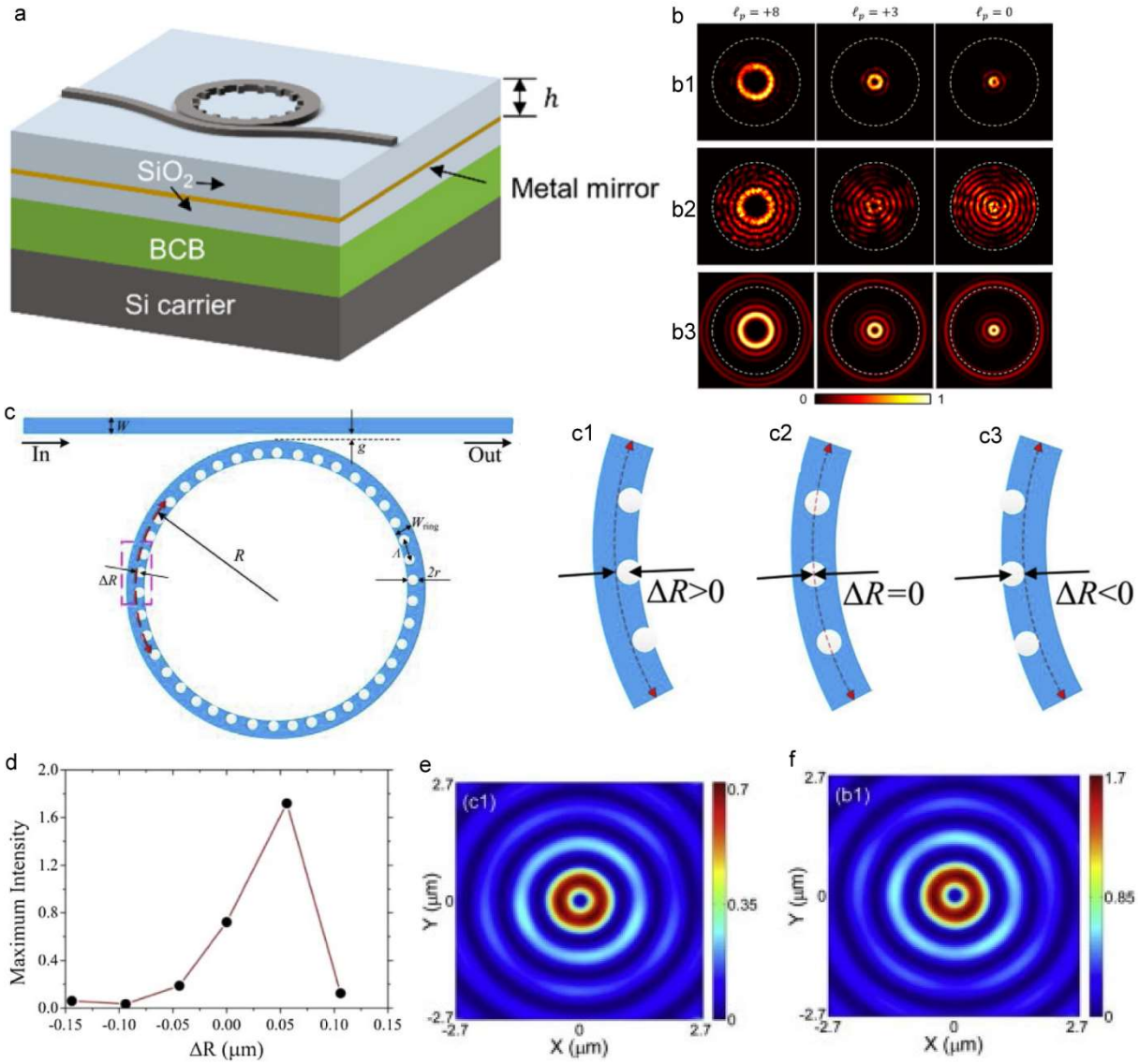

Figure 2.11 Demonstrations of methods for enhancing the emission efficiency of integrated vortex beam generators. (a) Schematic of a high-efficiency vortex beam emitter with a metal mirror in the silica layer, used for reflection to eliminate the effect of the concentric ring and reinforce the main lobe of the vortex beam [32]. (b) Simulation results with different topological charges. Left columns, $l = +8$; middle columns $l = +2$; right columns, $l = -1$). (b1) and (b2) The generated vortex beam with and without a mirror, respectively. (b3) Corresponding simulation results with a mirror. The white dotted circles indicate the positions of a 48-degree diffraction angle corresponding to $NA = 0.75$ [32]. (c) Schematic of the vortex beam emitter, followed by the zoom-in view of the ring waveguide for different values of ΔR, marked in the red-dotted rectangle[29]. (c1) $\Delta R > 0$ (c2) $\Delta R = 0$ (c3) $\Delta R < 0$. (d) The maximum intensity of interference patterns versus the radius difference ΔR [29]. (e) and (f) The normalised

simulation results of the vortex beam emitter with different ΔR, 0 and $+0.044\ \mu m$ respectively [29]. The intensity is normalised to the maximum intensity of the whispering gallery mode in the microring.

The third method, designed by Yuan G. et al., involves shifting the centre deviation of scattering elements (ΔR) to enhance emission efficiency, as depicted in Figures 2.11.(c-f). They found that increasing the centre deviation could lead to a significant enhancement in emission efficiency, as indicated by the curve in Figure 2.11.(d). For instance, when the centre deviation is $0.05\ \mu m$, the maximum intensity of the emitted wave increases to 1.7 times the maximum intensity observed in the WGMs. However, when no centre deviation is used, the maximum intensity is only 0.7 times the maximum intensity observed in the WGM.

In addition to those methods for enhancing the emission efficiency of the integrated vortex beam emitters, the properties of the generated vortex beam can also be controlled by modifying the geometric structure. Sebbag Y. et al. proposed that by altering the geometric structure of the emitter, the emitted vortex beam shifts to a different angle, as illustrated in Figure 2.12.(b) [30]. The far-field intensity profiles shown in Figures 2.12.(c) and 2.12.(d), illustrate that varying the width of the ring waveguide along the propagation direction leads to changes in the emission angle of the generated vortex beam.

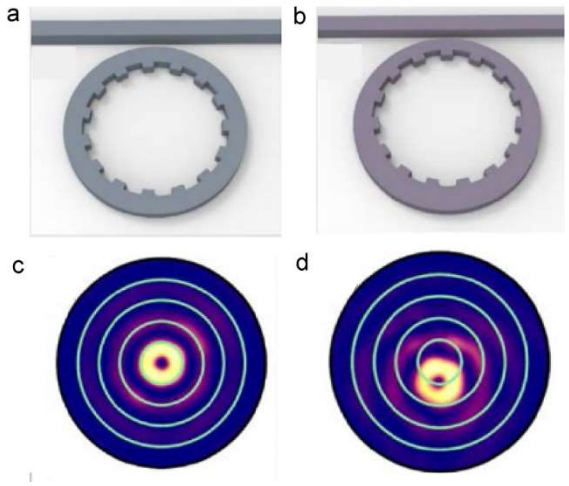

Figure 2.12 Demonstration of altering the emission direction of the generated vortex beam. (a) Schematic of a conventional vortex beam emitter [30]. (b) Schematic of a vortex beam emitter with width variation in the ring resonator [30]. (c) Far-field intensity profile for the conventional emitter [30]. (d) Far-field intensity profile for the width-varying emitter. As illustrated in (c) and (d), the doughnut beams have a 10-degree shift when there is width variation in the ring resonator [30].

2.1.4 Vector vortex beam

In this section, a detailed discussion about vector vortex beams is given, as it helps to understand the emitted beam from a microring-resonator-based vortex beam emitter.

A vector vortex beam represents a distinctive form of structured light beam characterised by its polarisation and phase characteristics. Unlike traditional scalar vortex beams, which maintain uniform polarisation across their cross-section, a vector vortex beam has spatially varying polarisation properties. This unique feature allows vector vortex beams to carry additional information compared to scalar vortex beams. This makes them highly beneficial in optical communication systems, where they can be used to increase data transmission rates by encoding information in both the polarization and the phase. The concept of higher-order Poincaré sphere was developed as an analytical tool utilising the vector vortex beams. In the case of the higher-order Poincaré sphere, we can change the polarisation of the emitted vector vortex beam by shifting the corresponding intensity or phase offset of input modes, as illustrated in Figure 2.9 [39, 46].

Given that this thesis utilises an integrated ring resonator for generating vortex beams, the following section will theoretically discuss the emitted waves of integrated vortex beam generators [43, 45, 48, 49].

For a ring resonator, the input TE mode from the access waveguide is coupled into the ring waveguide. Without any modification, the majority of light circulates within the ring waveguide at resonance wavelengths. To initiate vortex beam generation, grating elements, such as pillars or holes, must be placed on the ring resonator. These elements disrupt total inner reflection within the waveguide, leading to the emission of beams.

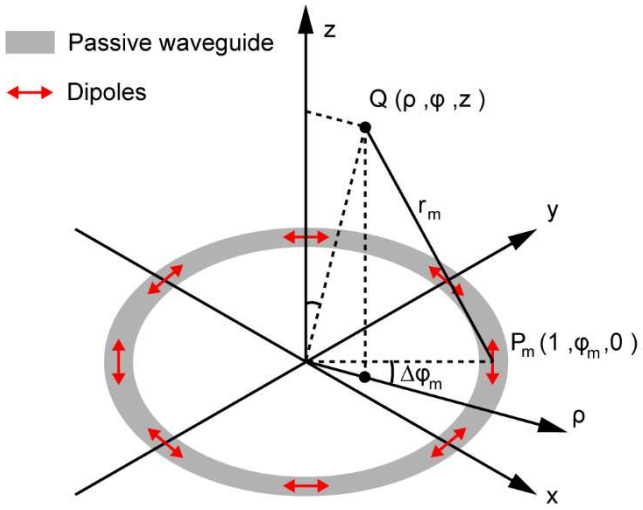

Figure 2.13 Schematic diagram when the scattering elements are placed on top of the waveguide. The corresponding dipoles have azimuthal polarisation in cylindrical coordinates [43]. Assuming the input mode is TE mode.

To comprehend the role of grating elements in generating the final emitted vector vortex beams, each element can be regarded as an electric dipole with linear polarisation. Here, I assume all the dipoles are in azimuthal orientation, as illustrated in Figure 2.13. Subsequently, the electric field of any point can be calculated as the supervision of the radiative waves of each element. An analytical model is built within normalised cylindrical coordinates (ρ, φ, z), where $R = 1$ is the polar radius of the waveguide and z denotes the distance from a point Q (located in the upper hemisphere, $z > 0$) to the resonator plane. Assuming all the dipoles are uniform, the moment of the dipole can be written as [48]

$$P(t) = P_0 e^{-j\omega t} \tag{2.8}$$

A phase delay should be considered, as the electromagnetic field created by the dipole will travel outward with a phase velocity $k = 2\pi/\lambda$, where λ is the vacuum wavelength [48]:

$$e^{jkr} \tag{2.9}$$

Each dipole will have an intrinsic phase related to the WGM inside the waveguide [48]:

$$e^{jl\varphi} \tag{2.10}$$

where the topological charge $l = p - gq$. Here, p is the azimuthal order of the WGM, q is the number of grating dipoles, and g is the grating order. To simplify the analysis process, g is set to one.

Therefore, the electric field of a point Q can be regarded as the sum of the contribution to Q from each dipole [43, 48]:

$$\boldsymbol{E}_l(\rho,\varphi,z) = \frac{P(t)}{4\pi\varepsilon_0}\sum_{m=1}^{q}\left\{e^{jkr_m}\cdot e^{jl\varphi_m}\right.$$
$$\cdot\left[\left(\frac{k^2}{r_m} - j\frac{k}{r_m^2} - \frac{1}{r_m^3}\right)\cdot(\widehat{\boldsymbol{r_m}}\times\widehat{\boldsymbol{\varphi_m}})\times\widehat{\boldsymbol{r_m}} - \left(j\frac{2k}{r_m^2} + \frac{2}{r_m^3}\right)\right. \quad (2.11)$$
$$\left.\left.\cdot(\widehat{\boldsymbol{r_m}}\cdot\widehat{\boldsymbol{\varphi_m}})\cdot\widehat{\boldsymbol{r_m}}\right]\right\}$$

where r_m is the distance between P_mQ, $r_m = \sqrt{\rho^2 + z^2 + R^2 - 2*R*\rho*\cos(\varphi_m - \varphi)}$ and the m_{th} dipole point P_m (1 ,r_m,0), and $\widehat{r_m}$ is the unit vector in the direction of P_mQ, pointing from P_m.

In the far-field zone, i.e., $z \gg \lambda/R$, the near-field terms ($\sim 1/r^2$ and $\sim 1/r^3$) can be neglected. The electromagnetic field of the emitter comes from the interference of far-field radiation from all dipoles [49]:

$$\boldsymbol{E}_l(\rho,\varphi,z) = \frac{P(t)\cdot k^2}{4\pi\varepsilon_0}\sum_{m=1}^{q}\left[e^{jkr_m}\cdot e^{jl\varphi_m}\cdot\left(\frac{1}{r_m}\widehat{\boldsymbol{\varphi_m}} + \frac{\rho\cdot\sin(\varphi_m-\varphi)}{r_m^2}\widehat{\boldsymbol{r_m}}\right)\right] \quad (2.12)$$

To simplify Eq. 2.12, I assume $\rho \ll z$, as any light too far from the propagation will not be detected by our sensor. Therefore, the second term in Eq. 2.12 can be neglected, and the emitted field becomes [49]:

$$\boldsymbol{E}_l(\rho,\varphi,z) \approx \frac{P(t)\cdot k^2}{4\pi\varepsilon_0}\sum_{m=1}^{q}\frac{e^{jkr_m}}{r_m}\cdot e^{jl\varphi_m}\,\widehat{\boldsymbol{\varphi_m}} \quad (2.13)$$

Then, I use Taylor expansion with respect to r around the point $r = r_m$ (where $R^2 \ll z^2 + \rho^2$) to approximate r_m, the zeroth-order approximation is:

$$r_m \approx \sqrt{\rho^2 + z^2} \quad (2.14)$$

The first-order approximation is:

$$r_m \approx \sqrt{\rho^2 + z^2} - \frac{\rho * R * \cos(\varphi_m - \varphi)}{\sqrt{\rho^2 + z^2}} \quad (2.15)$$

Here, I apply first-order approximation for the phase and the zeroth-order approximation for the amplitude to Eq. 2.13, as phase is more sensitive than amplitude to errors due to its 2π periodicity:

$$\boldsymbol{E}_l(\rho,\varphi,z) \approx \frac{P(t)\cdot k^2}{4\pi\varepsilon_0}\cdot\frac{e^{jkr}}{r}\sum_{m=1}^{q}e^{-jk\rho R\cos(\varphi_m-\varphi)/r}\cdot e^{jl\varphi_m}\,\widehat{\boldsymbol{\varphi_m}} \quad (2.16)$$

where $r = \sqrt{\rho^2 + z^2}$ is the spherical radius from the origin point to the Q point.

Here, I found that Eq. 2.16 has the form of the Bessel function of its first kind:

$$J_n(x) = \frac{1}{2\pi j^n}\int_0^{2\pi} e^{jx\,cos(\tau)+jn\tau}d\tau \tag{2.17}$$

When $q \gg 2\pi$, the discrete sum approaches an integral:

$$\begin{aligned}\sum_{m=1}^{q} e^{-jk\rho \mathrm{R}\cos(\varphi_m-\varphi)/r}\cdot e^{jl(\varphi_m-\varphi)} \\ \approx \frac{q}{2\pi}\int_0^{2\pi} e^{-jk\rho R\cos(\varphi_m-\varphi)/r}\cdot e^{jl(\varphi_m-\varphi)}\,\mathrm{d}\varphi_m = q * j^{-l}\end{aligned} \tag{2.18}$$

With the relation $J_{n-1}(x) + J_{n+1}(x) = (2n/x)\,J_n(x)$, I can obtain the analytical expression of the far-field radial component:

Substitute Eq. 2.18 into Eq. 2.16, and we can obtain:

$$\boldsymbol{E}_l(\rho,\varphi,z) \approx \frac{P(t)\cdot k^2}{4\pi\varepsilon_0}\cdot\frac{e^{jkr}}{r}\cdot q\cdot e^{jl\varphi}\cdot j^{-l}J_l(k\rho R/r)\,\widehat{\boldsymbol{\varphi}_{\boldsymbol{m}}} \tag{2.19}$$

The final expression of the field depends on the choice of the polarisation basis. Then, since the electric field along the propagation axis z cannot be detected for a transverse field, the transversal polarisation of the emitted beam in the normalised cylindrical coordinate can be expressed as

$$\boldsymbol{E}_l(\rho,\varphi,z) = \frac{qP(t)}{4\pi\varepsilon_0}k^2\frac{e^{jkr}}{r}j^{-l}\left[\left(\frac{lr}{k\rho R}\right)J_l\left(\frac{k\rho R}{r}\right)\widehat{\boldsymbol{\rho}} + jJ_l'(k\rho R/r)\widehat{\boldsymbol{\varphi}}\right] \tag{2.20}$$

For better understanding, I transform the electric field under the circular polarisation basis $\hat{L}$ and $\hat{R}$:

$$\boldsymbol{E}_l(\rho,\varphi,z) = \frac{qP(t)}{4\pi\varepsilon_0}k^2\frac{e^{jkr}}{r}\frac{j^{-l}}{\sqrt{2}}\left(e^{j(l-1)\varphi}J_{l-1}\left(\frac{k\rho R}{r}\right)\hat{\boldsymbol{L}} + e^{j(l+1)\varphi}J_{l+1}\left(\frac{k\rho R}{r}\right)\widehat{\boldsymbol{R}}\right) \tag{2.21}$$

Based on Eq. 2.20, I can observe that when monitoring the electric field under cylindrical coordinates, the emitted electric field possesses the OAM state l at both the radial and azimuthal directions. However, when analysing the electric field in terms of the circular polarisation basis, the OAM states are $l_L = l - 1$ and $l_R = l + 1$, respectively. Thus, the final expression of the field varies depending on the choice of polarisations.

Figure 2.14 illustrates the far field intensity and polarisation profiles with different l, from -2 to 2, respectively. In the figure, the far-field profile for $l = 0$ exhibits a doughnut shape, while for $l = \pm 1$, the centre of the beams shows non-zero intensity, which contrasts with the description of the LG mode. The reason for this phenomenon is that the emitted beam is a vector vortex beam. In

Ref. [34, 49], the authors shared a similar assumption regarding the vector vortex beam. In the case of $l = \pm 1$, the vector vortex beam can be regarded as the superposition of two orthogonal scalar waves: a left-hand circularly polarised (LHCP) beam with a topological charge of $l - 1$ and a right-hand circularly polarised (RHCP) beam with a topological charge of $l + 1$. For both OAM states, their transverse fields consist of a wave with zero charge and another wave. The wave with zero charge contributes to the brightness in the centre. As for $l = 0$, its transverse field can be decomposed into two waves with opposite topological charge (-1 and $+1$), which can be expressed by the higher order of Poincaré sphere. These two elements are the polar basis of a Poincaré sphere. The other explanation for the doughnut-shaped profile of the OAM state zero is that the emitted field depends on the polarisation of the beams in the ring waveguide and the elements' position. Therefore, the centre of the polarisation condition has a singularity, resulting in a doughnut shape in the intensity profile, which differs from the general vortex beam (having a non-zero intensity at the beam centre, for $l = 0$). Figure 2.14 shows a set of beam profiles, and I have reproduced these results from the literature in my own simulation.

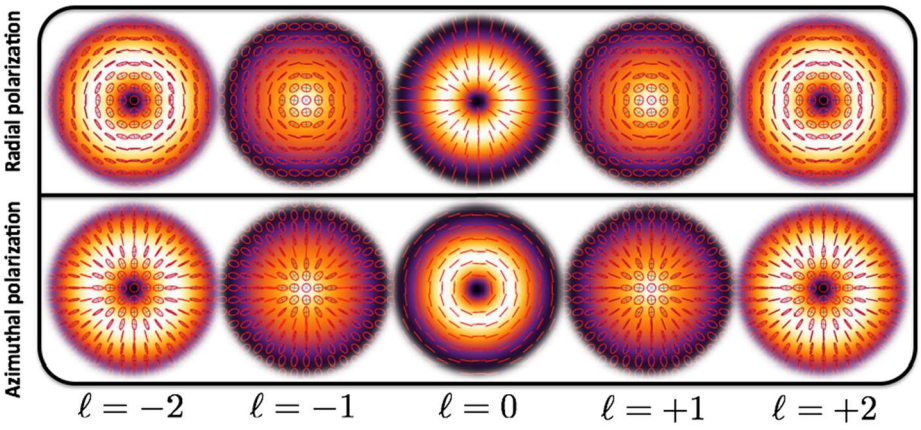

Figure 2.14 The theoretical intensity and polarisation patterns for a beam emitted from a ring resonator [34]. The upper row is for the light polarised perpendicular to the waveguide, yet in the plane of the resonator, while the lower row is for the polarised parallel to the waveguide, leading to a radial and an azimuthal polarisation distribution inside the ring resonator, respectively. Each column corresponds to a specific topological charge l of the OAM eigenstates. Interestingly, in the case where $l = \pm 1$, the intensity pattern of the outgoing beam does not form a doughnut shape. Their polarisations switch from the radial to the azimuthal, and vice versa. This type of beam is known as a Poincaré or polarisation-singular beam. In the figure, the concentric ring profile due to confinements of the scattering sources is neglected, which means the mode index p is zero in the Laguerre-Gaussian mode ($LG_0^{|l|}$).

2.2 Metasurfaces

As the focus of this thesis is on investigating metasurface-integrated vortex beam emitters, a brief overview of metasurfaces is given below.

Metasurfaces are a prevailing research area for numerous scientists due to their impressive flexibility in manipulating light behaviour using subwavelength-sized meta-atoms. This manipulation happens in various aspects, including intensity [50-52], phase [53-55], polarisation [56-58], and more. Moreover, many metasurfaces are relatively easy to fabricate using standard nanofabrication techniques such as plasma-enhanced chemical vapour deposition (PECVD), electron-beam lithography (EBL), and reactive ion etching (RIE).

Metasurfaces can generally be categorized into two main types based on the materials: plasmonic metasurfaces and dielectric metasurfaces [59]. Plasmonic materials (such as metals and some conducting oxides at certain wavelengths) exhibit strong interaction with light through plasmonic resonance. However, these materials suffer from significant resistive losses, leading to reduced efficiency. For example, in Ref. [60], gold metasurfaces were employed to create mode converters, and the output suffered from a 50% loss. Moreover, some plasmonic materials, such as gold or silver, can be expensive. On the contrary, dielectric materials such as silicon or titanium dioxide offer solutions to these limitations. They can provide efficient light manipulation with reduced resistive losses compared to plasmonic materials.

2.2.1 2π phase coverage

In numerous metasurface applications [61-63], the primary objective of the design is to achieve a 2π phase-change coverage when manipulating the phase of scattered light. In Ref. [61], the authors presented a high-efficiency gradient metasurface for anomalous reflection. Figure 2.15 depicts the gradient super-unit cell comprising 10 meta-atoms. It is easy to observe that if the designed super-unit cells can achieve 2π phase-change coverage, the reflected light can form a continuous wavefront when multiple super unit cells are cascaded end to end.

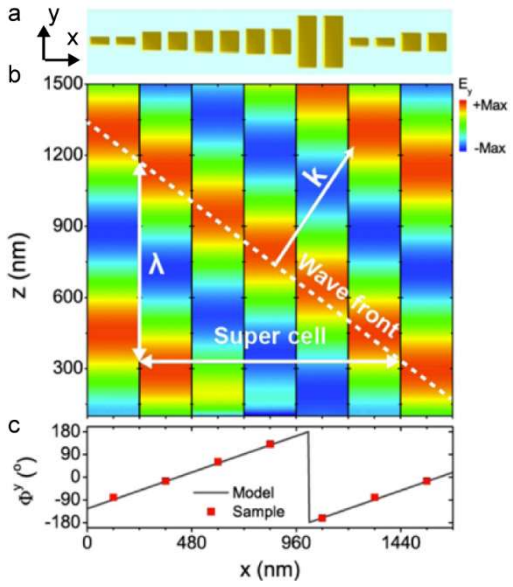

Figure 2.15 An example of a continuous wavefront with 2π phase change coverage. (a) Super unit cells' structure in top-down view. (b) Wave propagation from each meta-atom along the z-axis. The white dotted line represents the matching wavefront of the reflective light. (c) The 2π phase-change coverage with red dots indicating the phase value for each meta-atom. [61]

Metasurfaces, utilised in Chapter 3, are phase-gradient metasurfaces, where achieving 2π phase-change coverage is crucial for the metasurface-integrated vortex beam emitter. Here, an example metasurface, depicted in Figures 2.16 and 2.17, serves to illustrate the significance of achieving 2π phase coverage.

Assuming the phase change can be induced by altering the size of the cylinders, in the discussion below, a wide range of out-coupling angles (θ) can be obtained by designing super unit cells. As illustrated in Figure 2.16, two types of super-unit cells are positioned on top of two waveguides, each containing six meta-atoms. The meta-atoms in both figures are placed at the same pitch. The only difference between these two figures, is the size of the meta-atoms. It is easy to observe that θ is larger when a large gradient is applied. Therefore, when the meta-atoms can achieve 2π-phase-change coverage, I have the freedom to control the out-coupling angle of the emitted waves.

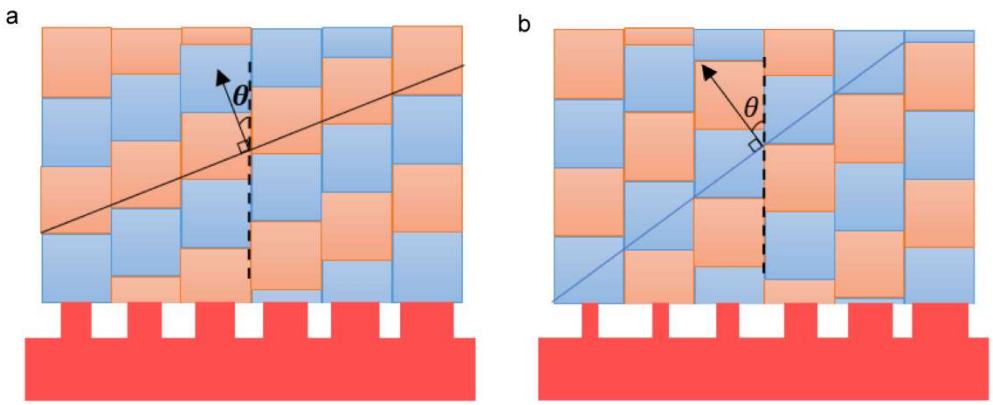

Figure 2.16 The phase profiles of light emitted by two metasurface-integrated waveguides. They show that if the phase change induced by changing the cylinder's size can cover a 2π range, it is possible to design a metasurface with a large area due to the continuous wavefront.

Metasurfaces capable of achieving a 2π phase change can produce a continuous wavefront, when super unit cells are cascaded together. It enables metasurface to scatter light directly at a specific out-coupling angle θ. Figure 2.17 illustrates the consequences when a metasurface fails to achieve 2π phase change coverage. A discontinuity in the wavefront occurs between adjacent super-unit cells, leading to distortion of scattered light and dispersion of out-coupling light in multiple directions.

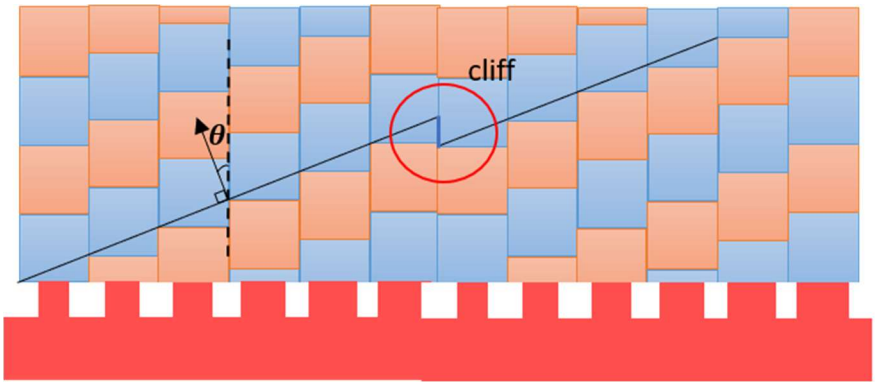

Figure 2.17 A cliff exists in the wavefront of adjacent phase-gradient super-unit cells. When a super-unit cell does not provide a full 2π phase coverage. This cliff will distort the scattered light and change the outcoupling angle.

For dielectric metasurfaces, there are three primary approaches employed to achieve 2π phase-change coverage: the Pancharatnam-Berry (PB) phase [24, 64-66], the Fabry-Pérot (FP) resonance [67, 68], and the Mie resonance [69].

The PB phase, also known as the geometric phase or the Berry phase, is based on the discoveries made by Pancharatnam in the 1960s. The spin-reversed scattered wave gains an additional phase factor when the planar resonator is rotated by an angle with respect to the

propagation direction. It was interpreted as a geometrical phase by Berry in the 1990s. Therefore, this PB phase can achieve 2π phase-change coverage by altering the orientation angle of the scatter. In Figure 2.18, Luo W. et al. used PB metasurfaces to transform the linearly polarised beam into two beams, the left circularly polarised beam and the right circularly polarised beam, respectively [24].

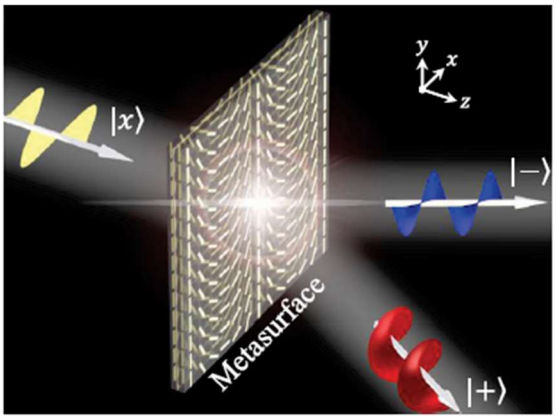

Figure 2.18 Schematic of the 100% efficiency photonic spin hall effect achieved by PB metasurfaces. The $|x\rangle$, $|+\rangle$, $|-\rangle$ represents the beams with linear polarisation, left circular polarisation, and right circular polarisation, respectively. [24]

The Fabry-Pérot (FP) resonance approach uses high aspect ratio nano-pillars to create phase delay between meta-atoms, enabling the realisation of 2π phase-change coverage. These nano-pillars, characterised by their different effective indices, act as truncated waveguides. Zhou Z. et al. proposed a metasurface-decorated beam deflector based on this approach, as illustrated in Figure 2.19.(a). By varying the cross-sectional radii of the meta-atoms, different effective indices are obtained (Figure 2.19.(b)). Since the effective index indicates the speed of the light, a phase change is introduced into the scatted light for each meta-atom. Therefore, the output light of the metasurfaces is deflected into a different angle, as shown in Figure 2.19.(c). In this case, the required aspect ratio is determined by the refractive index contrast of the materials. As an example, the crystalline silicon, used in this study [67], has a refractive index of 4.295 at $700\ nm$, the corresponding aspect ratio required to achieve 2π phase-change coverage is 2.68. While for the TiO_2 material in Ref. [68], which has a refractive index of approximately 2.4 at $660\ nm$, the aspect ratio increases to $10 \sim 15$.

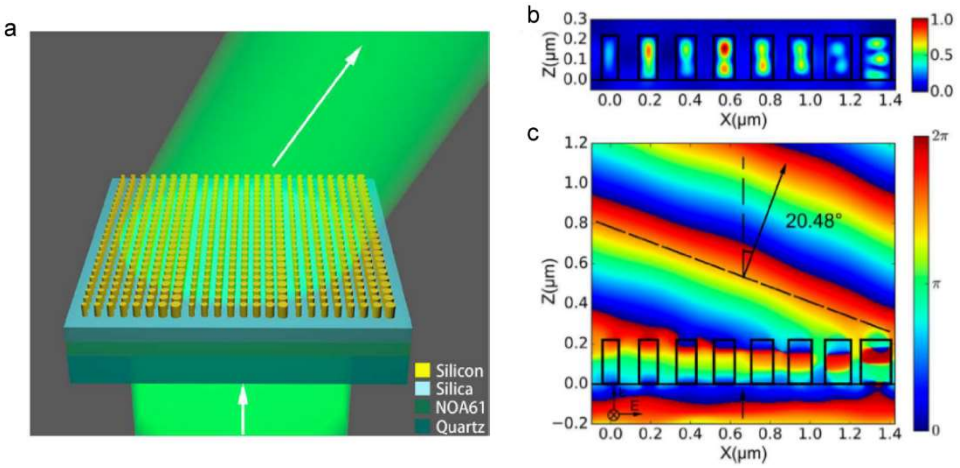

Figure 2.19 Demonstration of a beam deflector using Fabry-Pérot resonance for achieving 2π phase-change coverage. (a) Schematic of a gradient metasurface that acts as a beam deflector. (b) Mode profile for each $220\text{-}nm$-thick crystalline-silicon post of the deflector showing the magnetic field amplitude in the xz plane at $532\ nm$. (c) The phase profile obtained by the metasurfaces results in a diffraction angle of $20.48°$. The incident light is a plane wave below the substrate. [67]

The Mie resonance approach [70-72], in contrast to the FP approach, can achieve full 2π phase-change coverage using meta-atoms with a small aspect ratio. These meta-atoms are described as Huygens source nano-antennas. As light is transmitted into the meta-atoms, it stimulates two types of resonance, which are the electric dipole of Mie resonance and the magnetic dipole of Mie resonance. Each of these resonances can introduce a π phase change. Therefore, by overlapping these two resonances, a 2π phase-change coverage is obtained. He F. et al. [73] utilised the Mie resonance to achieve output beam steering over an angular range of 9 degrees, as illustrated in Figure 2.20.

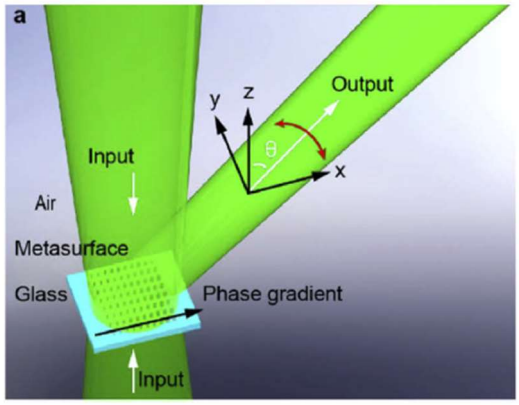

Figure 2.20 Schematic diagram of a beam-steering metasurface using Mie resonance for obtaining 2π phase-change coverage. It features an array of silicon nano-pillars positioned on a semi-infinite glass substrate. A phase gradient is established along the x direction within the metasurfaces. The output beam can sweep by 9 degrees through controlling the two normal inputs. For clarity, the semi-infinite substrate is represented as a slab with no output into it [73].

2.2.2 Applications of Metasurfaces

Metasurfaces have garnered considerable research interest across diverse fields owing to their ability to manipulate light behaviour using ultra-thin layers of sub-wavelength nanostructures. This has led to explorations across various domains, including beam deflectors, beam splitters, metalenses, mode converters, and metasurface holograms.

2.2.2.1 Beam deflectors

A beam deflector plays a crucial role in optical systems by altering the propagation direction of incident light beams, as illustrated in Figure 2.21.(a). Many metasurfaces designed with 2π phase coverage can fulfil this requirement effectively. However, achieving high diffraction efficiency and minimising light dispersion becomes a significant challenge when designing a beam deflector. Recently, a nearly dispersion-less multi-colour metasurface beam deflector was proposed, it had a diffraction efficiency exceeding 89% [74]. Metasurface-based beam deflectors can be utilised for motion detection or facial recognition. In Ref. [75], the authors proposed a 21×21 array of deflectors for bending the input light into 441 random points simultaneously. Capturing the changes of these 441 random points allows the movement of an object to be determined. Moreover, in Ref. [76], the authors integrated metasurfaces onto a waveguide, which is able to deflect the input mode at a consistent out-coupling angle when light is illuminated from two opposite directions.

2.2.2.2 Beam splitters

A beam splitter can divide incident light into two or more beams, which has applications in optical and photonic systems, as illustrated in Figure 2.21.(b). One key functionality of a beam splitter is its ability to control the power distribution of the resulting beam. In Ref. [77], the authors demonstrated a metasurface-based beam splitter capable of not only reflecting the incident beam into two separate beams but also shifting the power ratio between these two beams by changing the incident angle. Another application of a metasurface beam splitter involves wavelength selection. In Ref. [78], a metasurface was demonstrated. The meta-atoms are viewed as truncated waveguides. Thus, when incident beams contain different wavelengths, each wavelength can be split into different angles, resulting in wavelength-dependent beam separation. Additionally, many studies have explored the polarisation-separation capabilities of beam splitters, referred to as polarisation correlation beam splitters. These beam splitters can effectively split beams based on their linear [79-81] or circular polarisation states [82-84]. All these functions make beam splitters useful in various areas, such as optical and photonic systems, optical communication systems, polarisation multiplexing systems, and polarisation imaging systems.

2.2.2.3 Metalenses

Metalenses, focusing light to a point (Figure 2.21.(c)), with their superior performance, advanced functionalities, and potential for integration with various optical elements, have attracted significant research attention. Conventional objective lenses often come with a bulky structure and complexity for integration. A common optical phenomenon when focusing light is called chromatic aberration. This phenomenon means that different colours fail to focus on the same focal point. Historically, other bulky optical components were employed to address this issue, leading to a complex and huge optical system. Nowadays, modern achromatic metalenses have emerged as a solution to this problem with an ultra-thin layer of nanostructures. Refs. [85, 86] proposed achromatic metalenses capable of providing consistent focal length for incident light across different wavelengths in the visible and terahertz regimes, respectively. These achromatic metalenses can find applications in various optical systems, such as microscopes, telescopes, and cameras. Nevertheless, a metalens with chromatic aberration has an application in wavelength dispersion. Chen W. et al. designed an off-axis metalens that exploits wavelength dispersion to accurately resolve incident wavelengths [85]. To further enrich the functionality of metalenses, researchers have explored the incorporation of phase-change materials [87] and coherent control mechanisms [88]. These advancements enable metalenses to switch their focal points, offering greater flexibility and versatility in optical applications.

2.2.2.4 Mode converters

To address the increasing demand for higher data capacity in optical communication and optical information processing, researchers have explored mode-division-multiplexing (MDM) technology. Within the MDM system, the mode converter is one of the vital elements. However, traditional mode converters suffer from drawbacks such as a large footprint, limited operation bandwidth, and relatively large insertion loss. Metasurfaces offer a promising solution to these challenges due to their remarkable ability to manipulate light in thin layers of subwavelength structures. In Ref. [89], Ohana et al. proposed a mode converter by placing metasurfaces on a $1\ \mu m\ \times\ 220\ nm$ Si waveguide at $1550\ nm$. This converter achieved full conversion from TE_0 to TE_1 modes using a length of only around $20\ \mu m$, with transmission rates of approximately 88% compared to that of the unmodified waveguide. Moreover, using plasmonic metasurfaces can further enhance the performance. In Ref. [60], the conversion length could be reduced to only 1.7 times the free-space wavelength when employing plasmonic metasurfaces, as illustrated in Figure 2.21.(d).

2.2.2.5 Metasurface hologram

Metasurface holograms offer several advantages over conventional photographs. Unlike regular photographs that only capture the intensity of light, holograms have the capability to record both the intensity and phase of light. This ability allows hologram images to appear as three-dimensional images. Compared to conventional holograms, metasurface holograms still offer three advantages [90, 91]. Firstly, metasurfaces can provide unprecedented spatial resolution, resulting in holographic images with low noise and high precision in the reconstructed images. Secondly, the use of subwavelength nano-atoms eliminates undesired diffraction orders which improves the quality of hologram images and shrink down the size of devices. Lastly, metasurface holograms can be fabricated over large areas, allowing them to produce holographic images with large space-bandwidth products, which enables a wide range of applications.

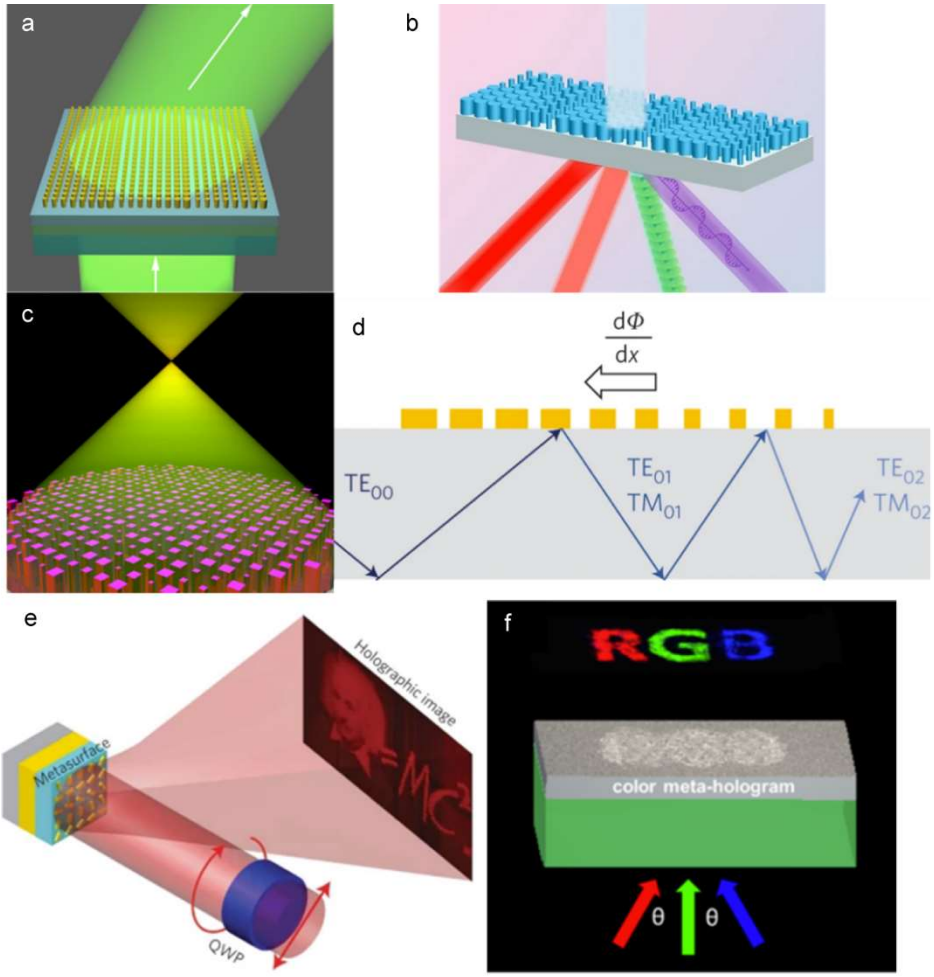

Figure 2.21 Demonstrations of metasurface applications. (a) A beam deflector at visible wavelength [67]. (b) Schematic figure of a beam splitter [92]. (c) A metalens [93]. (d) Applying metasurfaces to waveguides for mode conversion [60]. (e-d) Reflective metasurfaces and transmissive metasurfaces for image projection [94, 95].

2.3 Silicon waveguide

Due to its high refractive index, which is around 3.45 at 1550 nm and 3.416 at 375 μm, silicon finds widespread applications in semiconductor devices, biosensing, and photonics. This property can reduce the aspect ratio of the scattering elements, as discussed in Section 2.2.1. Moreover, silicon, being the second most abundant element in the Earth's crust and extensively researched for many years, has become the most widely used and cost-effective material for electronic devices. Silicon-on-insulator (SOI) wafers, featuring mature fabrication processes, are commonly available from various companies and laboratories. Because of these advantages, silicon is used as the key material in this thesis, facilitating a simple fabrication process for the proposed design.

Before designing devices, material loss is a crucial factor to consider, as it can significantly impact the device's efficiency, particularly for large devices. In Chapter 3, the infrared wavelength

of $1550\ nm$ is utilised. In Ref. [96], the authors proposed that a side wall smooth Si waveguide on an insulator exhibits propagation losses of $3.6 \pm 0.2\ dB/cm$ for the fundamental TE mode. Given that our device occupies only a small area of a few hundred micrometres, the corresponding material loss is small enough to be neglected. Thus, the propagation loss was not considered in Chapter 3. However, in Chapter 4, where THz waves are employed, the devices occupy a larger area, up to a few hundred centimetres. Therefore, the propagation loss of those devices should be considered. This aspect will be discussed in detail in that chapter.

2.3.1 Waveguide and its modes

As an industrial standard, SOI wafers have a 220-nm-thick Si layer on top of a 2-μm-thick SiO_2 layer. The Si layer is used for patterning waveguides that support light propagating along the desired direction. Therefore, Si waveguides with a thickness of $220\ nm$ are discussed below for introducing waveguide properties and modes (how the light propagates in the waveguide).

2.3.1.1 Waveguide

Waveguides are structures designed to guide waves along a specific route with minimal loss. Typically, a waveguide consists of a core material, characterised by a high refractive index (n_{core}) , and the core is surrounded by a cladding material with a low refractive index $(n_{cladding})$, as plotted in Figure 2.22.

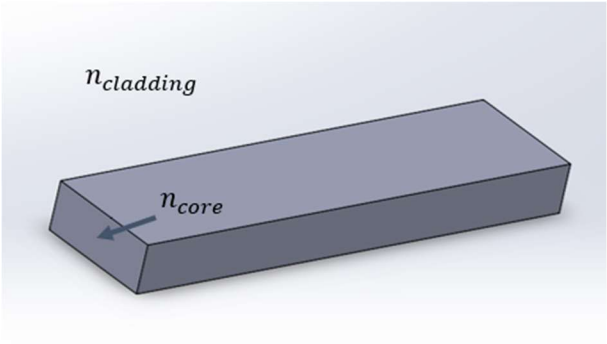

Figure 2.22 Illustration of a common structure of a strip waveguide. The core material is surrounded by cladding material $(n_{clad} < n_{core})$.

As Figure 2.23 illustrates, when incident light E_i travels inside the waveguide and encounters the interface between two materials with different refractive indexes $(n_1 < n_2)$, two phenomena occur: refraction (E_t) and reflection (E_r). Refraction can be explained by Snell's law, which describes the relationship between the angle of incident light and the angle of refraction when waves pass through an interface between two materials with different refractive indices:

$$\frac{sin\theta_2}{sin\theta_1} = \frac{n_1}{n_2} \tag{2.22}$$

When $n_1 < n_2$, the angle of refraction (θ_1) is always larger than the angle of incident light (θ_2). From Snell's law, it is easy to observe that if I continue raising θ_2, θ_1 can reach 90°. This implies that there will be no refraction of light into the low-refractive-index material. Under this situation, all the light is reflected back into the high-refractive-index material, leading to total internal reflection. This is the reason why n_{core} should be larger than n_{clad} in the waveguide.

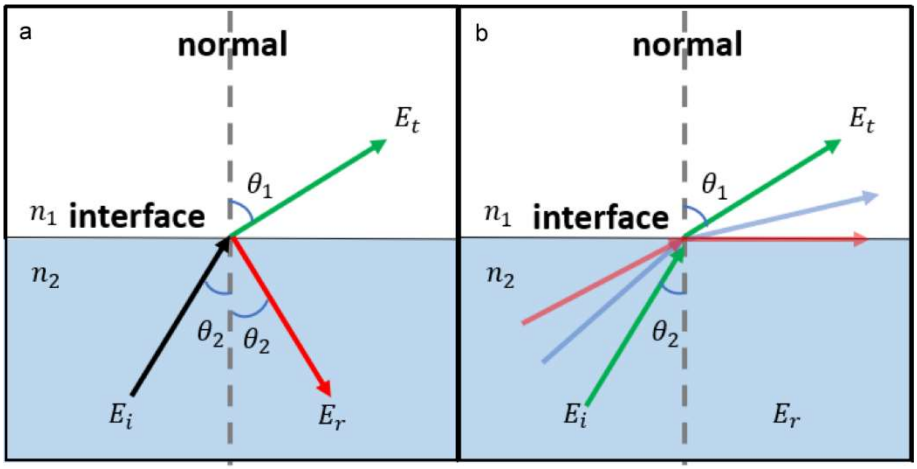

Figure 2.23 Demonstrations of Snell's law. (a) When the input light E_i (black) hits the interface from the high-refractive-index material (n_2) to the low-refractive-index material (n_1), a part of the light will be refracted into the upper layer as light E_t (green) at θ_1, following Snell's law. The rest of the light will reflect as light E_r (red), at θ_2. (b) Depicts how the incidence angle θ_2 affects the refraction angle θ_1. If I keep increasing θ_2 (larger than the critical angle, the red lines), the light will stop being refracted into the upper layer.

Waveguides come in various structures, including the strip waveguide and the rib waveguide, both of which are used in this thesis. A strip waveguide has a structure that is a high-refractive-index strip located on top of a planar structure, as illustrated in Figure 2.22. This kind of waveguide has strong light confinement, typically being surrounded by a low-refractive-index medium on three sides. On the other hand, a rib waveguide is similar to a strip waveguide but contains a slab at the bottom. According to Ref. [97], the thickness of the slab in a rib waveguide is often less than half the thickness of the top silicon layer to ensure single-mode propagation and eliminate the influence of high-order modes. In Chapter 3, the slab thickness is chosen to be 100 nm, as it helps to enhance the coupling efficiency of the ring resonator. This is essential for designing the integrated vortex beam emitter in Chapter 3.

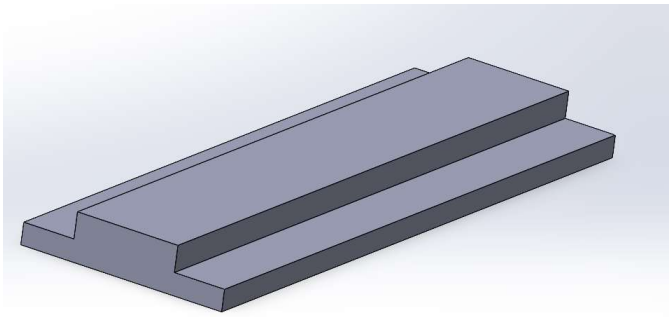

Figure 2.24 Schematic of a rib waveguide. It contains a slab at the bottom of the waveguide.

2.3.1.2 Waveguide Modes

Waveguide modes are time-harmonic solutions to Maxwell's equations that describe the transverse field pattern within a waveguide. These modes represent how the electromagnetic fields are distributed across the cross-section of the waveguide as EM waves propagate through it. To analyse waveguide modes and their properties, I have used simulation software called Lumerical. Lumerical is a leading commercial simulation software used for designing and optimizing photonic devices and integrated circuits. It contains various solvers to simulate various optical devices under different conditions. In this section, the finite-difference Eigenmode (FDE) solver is employed to analyse mode profiles, effective indices, and other relevant parameters.

The refractive index of materials and the structure of a waveguide determine which types of modes are capable of propagating inside the waveguide. As Figure 2.25 illustrates, the black lines represent the structure profile, which contains a silicon waveguide placed on top of a SiO_2 substrate and surrounded by air on the other three surfaces.

Each mode has a unique effective index, which is determined by the waveguide structure and mode order. The effective index n_{eff} can be calculated by:

$$k_x = n_{eff}\frac{2\pi}{\lambda} \tag{2.23}$$

where x is the propagation direction, k_x is the propagation constant, and λ is the light wavelength.

The effective index indicates the phase delay per unit length in a waveguide, relative to the phase delay in vacuum. When the effective index falls within the range of refractive indices of the core material n_{core} and the cladding material n_{clad} (i.e., $n_{core} > n_{eff} > n_{clad}$,), the corresponding mode can be guided inside the waveguide. In this case, total internal reflection occurs, keeping the light confined inside the waveguide. A higher effective index corresponds to

a slower speed of light propagating in the waveguide. On the contrary, when $n_{eff} < n_{clad}$, this mode is unguided, it results in light being refracted into the surrounding medium.

Based on the polarisation of the propagating light, waveguide modes can be categorised into four main types of modes: transverse electromagnetic modes (TEM), transverse electric modes (TE), transverse magnetic modes (TM), and hybrid modes. TEM mode implies both the electric and magnetic vectors are orthogonal to the propagation direction. However, this mode cannot propagate in a rectangle waveguide because the magnetic field lines cannot form closed loops. TE mode requires the electric vector to be perpendicular to the propagation direction, while TM mode requires the magnetic vector to be vertical to the propagation direction. Hybrid mode has the property that both the electric and magnetic vectors are nonzero in the propagation direction. In the 2D waveguide simulations, perfect TE and TM modes do not exist [98]. Therefore, in the following analysis, TE and TM modes are actually quasi-TE mode and quasi-TM mode. The six figures in Figure 2.25 show the amplitude profiles of the fundamental TE and TM modes in the cross-section of a waveguide, which has a height of $220\,nm$ and a width of $500\,nm$. The TE polarisation fractions of these two modes are 98% and 4%, respectively. The TE polarisation fraction is defined as the integration of the E_y intensity divided by the integrated total field intensity in the y-z plane. This is the reason why, in Figure 2.25.(b), the E_y component is relatively large and the E_z component is relatively small in Figure 2.25.(c). For the TM mode, given that the TE polarisation fraction is only 4%, the E_y component is significantly smaller than the E_z component. However, it is worth knowing that these calculated TE and TM modes have the H/E field in the direction of propagation. For the TE mode, the waveguide TE/TM fraction (the integrated transverse field intensity divided by the integrated total field intensity) is equal to 72.8%, while the TM fraction of the TM mode is 86.46%.

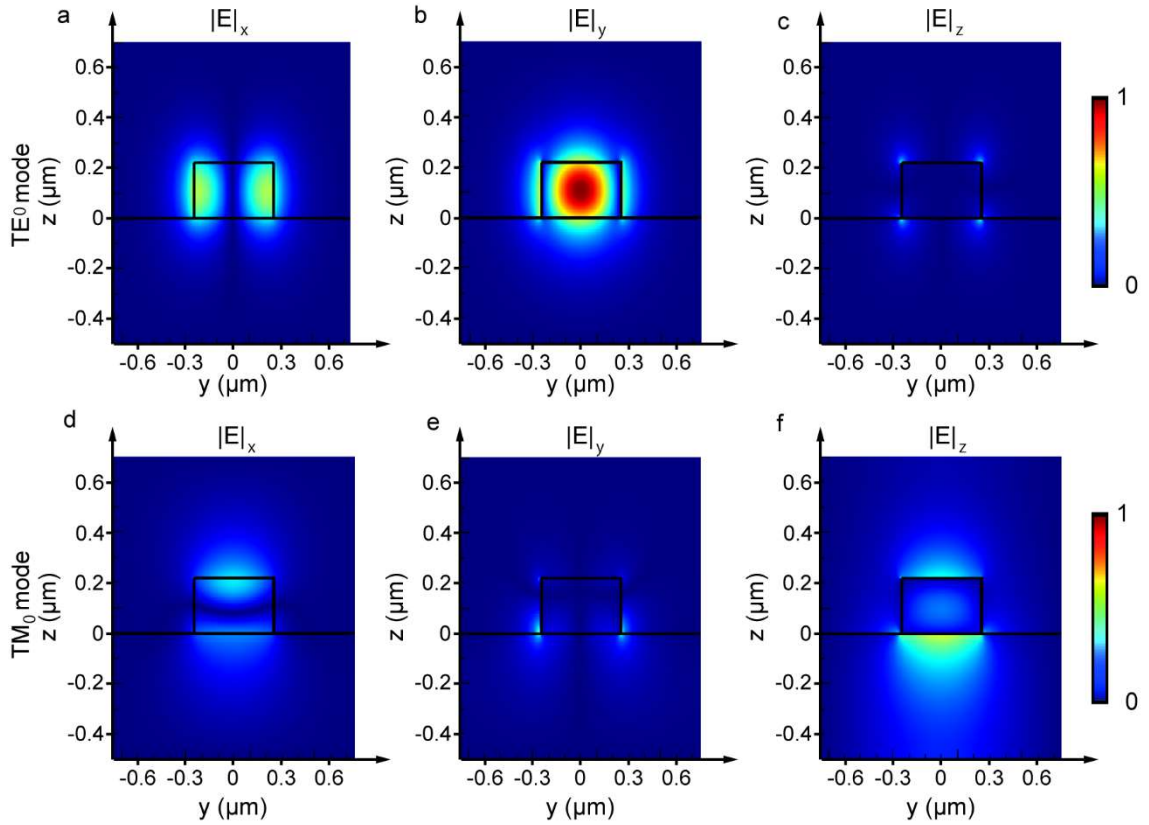

Figure 2.25 Electric field amplitude profiles of the fundamental TE mode ($n_{eff} = 2.3803$) and the fundamental TM mode ($n_{eff} = 1.607$). The black rectangle represents a $500\ nm \times 220\ nm$ silicon waveguide on a 2-μm-thick SiO_2substrate. The transverse field magnitude is normalised to 1. E_x, E_y, E_z are the three components of the electric field. For the simulated TE mode, the TE polarisation fraction is 98% and the waveguide TE fraction is 72.8%. As for the simulated TM mode, the TE polarisation fraction is 9%, and the waveguide TM fraction is 86.46%. The TE polarisation fraction is defined as an integration of the E_y intensity divided by the integrated total field intensity in the y-z plane. The TE/TM fraction of the waveguide is equal to the integrated transverse field intensity divided by the integrated total field intensity. For the TE mode, E_y intensity is larger than E_z intensity, as illustrated in (b) and (c). For the TM mode, E_y intensity is smaller than E_z intensity, as illustrated in (e) and (f).

2.3.1.3 Waveguide structure design

As previously discussed, when neglecting loss, only the guided wave can propagate inside the waveguide over long distances. Therefore, selecting the appropriate waveguide structure is essential because it determines the effective index of the guided mode. When designing a waveguide, it is recommended to choose a structure that exclusively supports one fundamental mode. This is because, apart from that fundamental mode, all the other modes will be refracted

into the cladding material, leaving only one guided mode in the waveguide. This feature is helpful for maintaining the waveguide to its original mode, especially for applications of information transmission. A parameter sweep was conducted on the waveguide width while maintaining a fixed height of $220\ nm$. The simulation focuses on the four largest effective indices as the width of the waveguide grows. The input wavelength was set at $1550\ nm$. Figure 2.26(a) illustrates the changes in the four largest effective indexes with an increasing width. It is observed that when the width of the waveguide reaches $500\ nm$, the waveguide only supports one quasi-TE mode and one quasi-TM mode. For a waveguide with a height of $220nm$ and a width of $500\ nm$, the effective index (n_{eff}) of the corresponding fundamental TE mode equals 2.38.

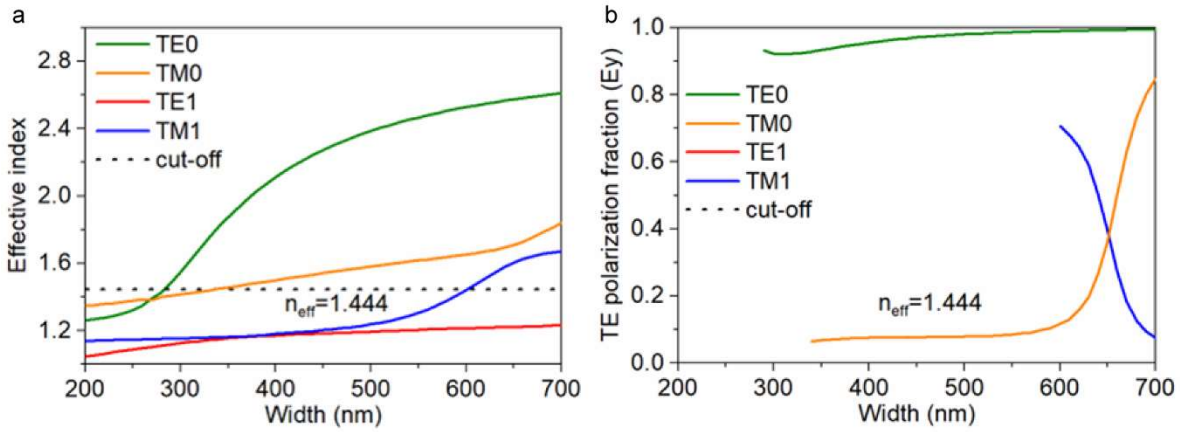

Figure 2.26 Numerically simulated mode properties. (a) The largest four n_{eff} values for width-varying waveguides. (b) Corresponding TE polarisation fraction, obtained from the E_y profile. There is a cut-off line, which equals the n_{eff} of the SiO_2 substrate. Only when $n_{eff} > 1.444$, the mode can be guided inside the Si waveguide. Otherwise, it is an unguided mode. The TE_0, TM_0, and TM_1 modes cross the cut-off line at $W \approx 290\ nm$, $W \approx 340\ nm$ and $W \approx 600\ nm$, respectively.

2.4 Silicon microring resonator

The all-pass ring resonator is a key component discussed in this report. It comprises a strip waveguide and a ring waveguide. The fundamental characteristics of the ring resonator can be derived by applying a continuous wave (CW) to the input port. Assuming the reflections of the light from the ring waveguide are negligible, the field ratio of the transmitted light to the input light is given by [99]

$$\frac{E_{pass}}{E_{input}} = e^{i(\pi+\gamma)} \frac{a - re^{-i\gamma}}{1 - rae^{i\gamma}} \tag{2.24}$$

where $\gamma = \beta L$ is the single-pass phase shift, L is the circumference of the ring, and β is the propagation constant of the propagating mode. Here, a is the amplitude of the light in the ring, and it accounts for the bending loss of the ring waveguide, the propagation loss of the material, and the loss in the coupling area. r is the self-coupling coefficient. From Eq. (2.24), the intensity of transmission is obtained as [99]:

$$T = \frac{I_{pass}}{I_{input}} = \frac{a^2 - 2ra\cos\gamma + r^2}{1 - 2ra\cos\gamma + (ra)^2} \tag{2.25}$$

A ring is considered to be in resonance when the phase ϕ is an integer multiple of 2π or when the wavelength of the light fits a whole number of times inside the optical length of the ring [99]:

$$\lambda_{res} = \frac{n_{eff} L}{m} \tag{2.26}$$

where n_{eff} is the effective index of the propagating mode, λ_{res} is the free-space resonance wavelength, and m is an integer that describes the order of the whispering gallery mode (WGM).

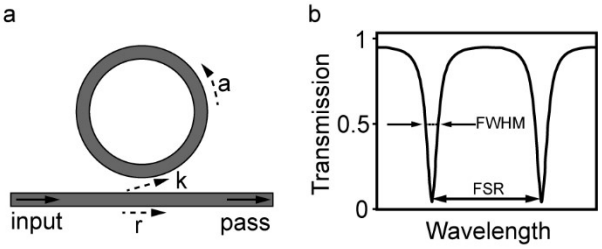

Figure 2.27 Demonstration of an all-pass ring resonator. (a) The top-down view of the all-pass ring resonator, consisting of an access waveguide and a ring waveguide [99]. (b) A model of transmission spectrum of an all-pass ring. (Modified figure from [99])

The transmission spectrum is crucial for characterising the performance of the ring resonator. Figure 2.27 illustrates the general shape of the ring resonator. The transmission is extracted at the pass port. There is a transmission drop at resonance wavelengths. There are two parameters to characterise the performance of a ring resonator: the full width at the half wavelength (FWHM) and the free-spectral range (FSR), respectively. The FWHM of the resonance can be analytically expressed as follows [99]:

$$FWHM = \frac{(1 - ra)\lambda_{res}^2}{\pi n_g L\sqrt{ra}} \tag{2.27}$$

Additionally, with a first-order approximation of the dispersion, the FSR, which represents the wavelength span of two adjacent resonances, is given by [99]:

$$FSR = \frac{\lambda^2}{n_g L} \tag{2.28}$$

In both equations, n_g is the group index related to the dispersion of the waveguide [99]:

$$n_g = n_{eff} - \lambda_0 \frac{dn_{eff}}{d\lambda} \tag{2.29}$$

Similar to the effective index n_{eff}, the group index also has the corresponding group velocity ($v_g = c/n_g$). It characterises the dispersive medium (waveguide) and represents the travelling envelope velocity for a transmitted pulse.

To design a ring resonator with desired properties, the key parameters are the radius of the ring resonator and the gap between the access waveguide and the ring waveguide. The ring radius affects the round-trip loss and bending loss, while the gap determines the access-ring power coupling ratio. These factors collectively determine the coupling regime. There are three coupling regimes used to describe the coupling efficiency: overcoupling, critical coupling, and undercoupling, as illustrated in Figure 2.28. For a given structure of a ring waveguide, there exists a critical distance (g_{crit}) between the access and ring waveguide, where the transmission at the resonance is close to zero. This implies that most of the light from the input is coupled into the microring. It also has the property that at non-resonance wavelengths, most of the light doesn't couple to the microring (i.e., the transmission is close to one). When the gap is lower than this critical gap, the ring resonator is over-coupled. The transmission at resonance is not close to zero, and the transmission is still quite high at the non-resonance wavelength. On the contrary, when the gap is higher than this critical gap, the ring resonator is under-coupled. In this case, a considerable amount of light is still remained in the pass port at resonance wavelengths. In both situations, the transmission at resonance wavelengths is higher than the critical point, which decreases the power intensity of the light circulating inside the ring resonator.

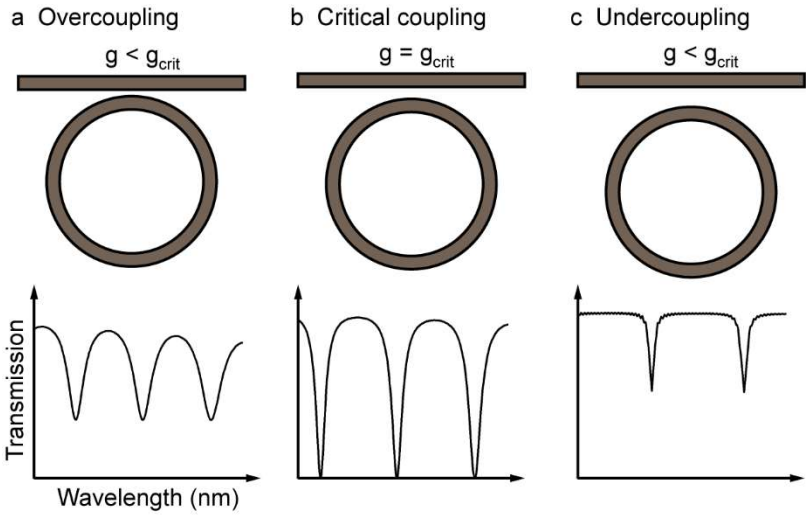

Figure 2.28 Illustration of three coupling regimes. When $g < g_{crit}$, the ring resonator is overcoupling. When $g = g_{crit}$, the ring resonator is in critical coupling. When $g > g_{crit}$, the ring resonator is undercoupling. (modified figures from [100])

Chapter 3 Asymmetric vortex beam emitter

In the previous chapter, integrated microring emitters for vortex beam generation and metasurfaces were discussed. However, the hybridisation of these two concepts has not been discussed in the literature to the best of my knowledge. Therefore, in this chapter, a hybridisation of metasurface and integrated vortex beam emitter is presented, and it can be regarded as a new approach for integrated OAM generation. In this approach, vortex beam emission is achieved by using a microring resonator that possesses a metasurface phase gradient. As compared to the two original design approaches, this hybrid approach allows for wavelength-based OAM tuning (i.e., the output vortex beam changes its OAM value with wavelength), position-based OAM tuning (referring to the grating period of light scatterers), and nanostructure-based OAM tuning (with structure referring to that of light scatters, a gradient of which creates a gradient in the output phase). Only the first two functionalities are available in conventional meta-waveguides, while the last tuning functionality represents a new concept in the regime of passive microring emitters.

A critical feature of this new design approach is symmetry breaking, which is introduced by the phase gradient. Symmetry breaking has profound importance in metasurface light manipulation. For example, a metasurface beam deflector can create a linear phase ramp that breaks the continuous rotational symmetry possessed by a planar surface. This symmetry breaking allows normal incident light to be deflected away from the surface normal [101, 102]. Another example is the photonic bound states in the continuum (BIC). A BIC state has to be converted into a quasi-BIC state to facilitate its detection, and this often relies on breaking the geometric symmetry of the BIC metasurface [103, 104]. A third example is to use metasurfaces to break the continuous rotational symmetry of a planar surface into discrete rotational symmetry that has a specific order. This has enabled a range of linear and nonlinear processes, including vortex transmutation [105], nonlinear optical circular dichroism [106], and nonlinear wavefront control [107].

The meta-device proposed here breaks a form of conjugate symmetry. In free-space vortex beam generation, the conjugate symmetry is associated with the geometric phase, and it forces right- and left-handed circular polarisation to generate symmetric OAM values (i.e., values that are identical in absolute value but opposite in sign). Ref. [108] reported for the first time a method based on metasurface J-plate to break the conjugate symmetry, which was subsequently used to develop OAM lasers [109]. For microring-based OAM emitters, the influence of the conjugate symmetry depends on whether the microring is an optically active device (i.e., a microring laser) or an optically passive device (i.e., a leaky waveguide antenna, the category that this work belongs to). In the former case, the conjugate symmetry again forces the OAM values to be symmetric. In order to generate nonzero net OAM, this symmetry must be broken, which has been realized

through methods such as introducing to the microring cavity a metasurface [110], an externally applied non-Hermitian coupling [111], or a slight shape deformation [112]. By comparison, in the latter case, where the microring contains no gain medium, the conjugate symmetry forces the OAM values to follow the direction of the WGM, which further follows the direction of the input light [4]. In these waveguide couplers, launching light into a microring in the opposite direction only changes the helicity of the output light; it has no influence on the absolute value of the OAM.

As will be discussed in detail below, our device breaks the conjugate symmetry that constrains the OAM generation in conventional microring light couplers. It allows a single device to generate identical or very different outputs by simply changing the input mode direction, which has never been reported before in Si chip-based emitters, to the best of our knowledge. I refer to this type of OAM emission as asymmetric vortex beam emission. This phenomenon could be utilised in OAM multiplexing for high-capacity free-space optical communications [113, 114]. Moreover, it allows for both wavelength-based and direction-based OAM tuning to function simultaneously. This feature could be explored to generate highly sculpted electromagnetic fields for manipulating particles and cells in miniaturised optofluidic systems [115-118].

In the analysis below, the generic device layout and the governing formula are first discussed in Section 3.1. It is followed by a discussion on the properties of individual meta-atoms in Section 3.2. An example device is then designed and analysed in detail, and the analysis includes the properties of in-plane transmission (Section 3.3) and off-chip emission at two representative wavelengths (Section 3.4and 3.5). Section 3.6 also contains a new method for extracting an OAM spectrum from a vector vortex beam.

This work has been conducted with strong support from Wangke Yu, who is also a PhD student at the University of Southampton. She is an expert in OAM spectrum analysis. She has analysed the OAM components for each emitted electric field, and I have led all the other parts of the work. Most results in this chapter are presented in the journal paper: Jianzhi Huang*, Wangke Yu*, Hailong Pi, Yijie Shen, Jize Yan, and Xu Fang "Asymmetric vortex beam emission from a metasurface-integrated microring with broken conjugate symmetry." *Optics Express* 31.25 (2023): 42549-42561.

3.1 Design schematic of the emitter

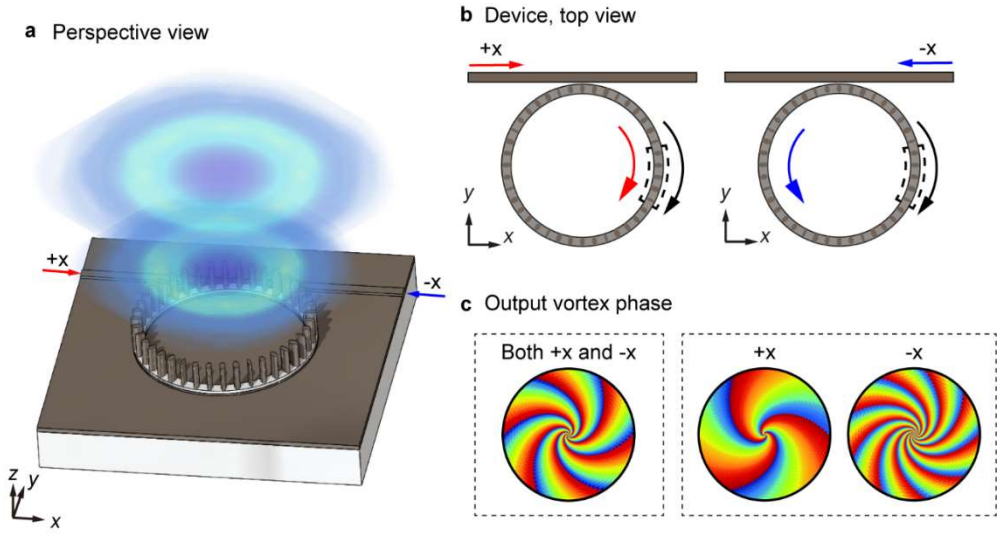

Figure 3.1 Schematic diagram of the metasurface-integrated microring vortex beam emitter. (a) The emitter consists of a Si microring resonator evanescently coupled to a straight Si bus waveguide. A Si nanopillar-based phase gradient metasurface resides on top of the Si microring, and the metasurface and the microring are separated by a thin layer of SiO_2. The input light, which propagates in either the $+x$ or the $-x$ direction along the bus waveguide, can excite a WGM resonance inside the microring. The metasurface converts the WGM into a vertically propagating vortex beam that carries OAM. (b) The WGM can propagate in either the clockwise direction (the red curved arrow) or the counter-clockwise direction (the blue curved arrow), depending on the direction of the incident light. By comparison, the intrinsic phase gradient of a metasurface super unit cell (the black curved arrow and the dashed box) stays invariant. (c) The metasurface phase gradient breaks conjugate symmetry and generates a phenomenon that I refer to as asymmetric vortex beam emission. Comparing to the conventional emitter, it allows the $+x$ and the $-x$ incident lights to generate two different sets of OAM values. Two possible output scenarios are illustrated here, where the two inputs, which have an identical wavelength, can generate identical or very different outputs.

Figure 3.1 schematically illustrates the proposed metasurface-integrated microring vortex beam emitter. The meta-device utilises the silicon-on-insulator (SOI) platform, which is adopted in a plethora of areas, including photonic crystals [119, 120], metasurfaces [121, 122], optomechanics [123, 124], and photonic integrated circuits [125, 126]. The meta-device consists of a Si microring resonator and a straight Si bus waveguide [Figure 3.1.(a)]. The microring is decorated on top with many uniformly distributed Si nanopillars, with a SiO_2 buffer layer inserted between the microring and the nanopillars. The nanopillars have a fixed height but vary in cross

section, and together they function as a phase gradient metasurface. When the microring is driven at a resonance wavelength, a WGM forms inside the microring, which propagates either in the clockwise direction [Figure 3.1.(b), for input that propagates in the $+x$ direction in the bus waveguide] or the counter-clockwise direction (for input in the $-x$ direction). Through light scattering induced by the nanopillars, the metasurface extracts energy from the WGM and generates an OAM beam that propagates in the vertical direction (i.e., the $+z$ direction) [Figure 3.1.(a)].

The meta-device possesses a metasurface-induced phase gradient [Figure 3.1.(b)]. In conventional passive microring vortex beam emitters [4, 29, 46, 127-129] that do not possess such a gradient, the topological charge l of the output vortex beam follows the angular phase-matching condition [4] and can be expressed as

$$l = \pm(m - q) \tag{3.1}$$

Here, m is the azimuthal order (i.e., the cycle number) of the WGM, and q is the element number of the angular grating (e.g., the number of holes in our recent work in Ref. [46]). The propagation direction (clockwise or counter-clockwise) of the WGM determines the sign of the topological charge but has no effect on its absolute value. A schematic transmission spectrum of a conventional passive microring vortex beam emitter is plotted in Figure 3.2. There are three sharp resonances. Assuming the centre resonance is when $l = 0$. Because the grating elements remain the same and the WGMs have different azimuthal orders, the OAM states of these three resonances can be derived from Eq. (3.1), labelled in Figure 3.2.

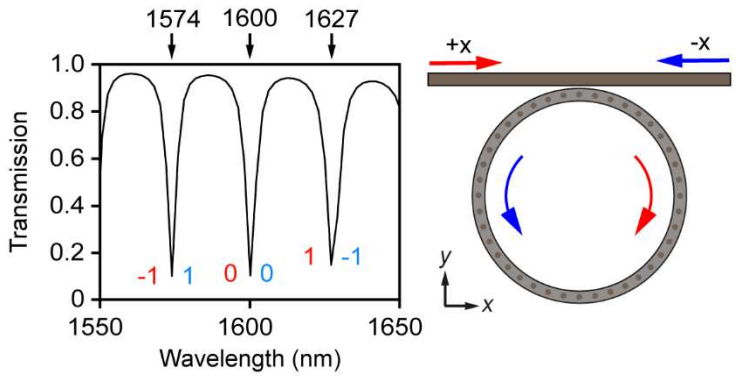

Figure 3.2 Schematic transmission spectrum of a conventional passive microring vortex beam emitter. 40 identical pillars located on top of microring. Three resonances are shown from $1550\ nm$ to $1650\ nm$. When the input mode is luminated along the +x or -x direction, the estimated topological charge at each resonance wavelength is labelled near the sharp dips (following Eq. (3.1)). Blue numbers indicate the input light is along the +x direction, while red numbers indicate the -x direction. The topological charge $l = 0$ corresponds to the centre resonance.

To modify Eq. (3.1) for the phase gradient microring shown in Figure 3.1, I first interpret Eq. (3.1) by considering the phase difference α between adjacent light scatterers on a microring. For all passive microring OAM emitters, including both the conventional ones and the new type proposed here, the topological charge l of their OAM beam is always the number of optical cycles around the beam axis. By projecting these optical cycles onto the light source (i.e., the light scatterers along a microring), we can see that $l = q \cdot \alpha/(2\pi)$, where 2π represents the whole microring. By replacing a conventional angular grating (e.g., a set of identical holes in Ref. [46]) with a phase gradient metasurface [e.g., a set of different Si nanopillars as shown in Figure 3.1.(a)], I introduce a new contribution to the phase difference α. This new contribution is the intrinsic phase difference θ between adjacent nanopillars. Here, the term intrinsic implies that a phase difference can exist in light scattering, even if two nanopillars are excited at the same conditions, which is studied below in Figure 3.3. I can consequently arrive at a generic expression for the topological charge l, which encompasses both the conventional passive microring emitters and the meta-devices studied here:

$$l = \pm(m - q) + n \tag{3.2}$$

Here, $n = q \cdot \theta/(2\pi)$, and it is the contribution of the phase gradient metasurface. For a conventional microring emitter, $\theta = 0$ and Eq. (3.2) reduces to Eq. (3.1). The sign of n is independent of the rotation direction of the WGM and the direction of the input light because it originates from the intrinsic phase gradient of the metasurface [Figure 3.1.(b)].

The extra term n in Eq. (3.2) provides an extra degree of freedom for controlling the topological charge l in microring-based vortex beam emission. More importantly, it breaks the conjugate symmetry that exists in Eq. (3.1). Eq. (3.1) forces l_{+x} and l_{-x}, the respective topological charge under the $+x$ and $-x$ inputs, to always follow $l_{+x} + l_{-x} = 0$, as illustrated in Figure 3.2. It implies that flipping the input direction always results in flipping the helical wavefront of the vortex beam. By comparison, the new term of n in Eq. (3.2) does not change its sign with the input direction. This leads to $l_{+x} + l_{-x} \neq 0$, meaning that the conjugate symmetry between the $+x$ and $-x$ configurations is broken, for nonzero values of n. The values of l_{+x} and l_{-x} become independent of each other, because n is a parameter that can be adjusted independently from the value of $m - q$. I consequently refer to vortex beam emission that obeys $l_{+x} + l_{-x} = 0$ as symmetric vortex beam emission, and cases that follow $l_{+x} + l_{-x} \neq 0$ as asymmetric vortex beam emission. However, it is important to clarify that this independence exists only at the design stage. Once the device is fabricated, the relative differences between the two sets of OAM values become fixed. In the following sections, I numerically demonstrate the phenomenon of asymmetric vortex beam emission, by showing first a unique case where $l_{+x} = l_{-x} = -8$ (Section 3.4) and then a more general case where $l_{+x} = -9$ and $l_{-x} = -7$ (Section 3.5).

3.2 Properties of individual meta-atoms

The metasurface is designed following a standard intuition-guided procedure [130], where a large number of different meta-atoms are characterized individually as the first step [Figure 3.3].Figure 3.3.(a) is the schematic of a single meta-atom, which consists of a Si nanopillar and a Si rib waveguide that are separated by a thin layer of SiO_2. The SiO_2 buffer layer is included here to suppress the strength of the evanescent coupling between the nanopillar and the waveguide [76, 131]. Beneath the Si waveguide, a SiO_2 BOX (buried oxide) layer optically isolates the waveguide from the Si substrate [not depicted in Figure 3.3.(a)].

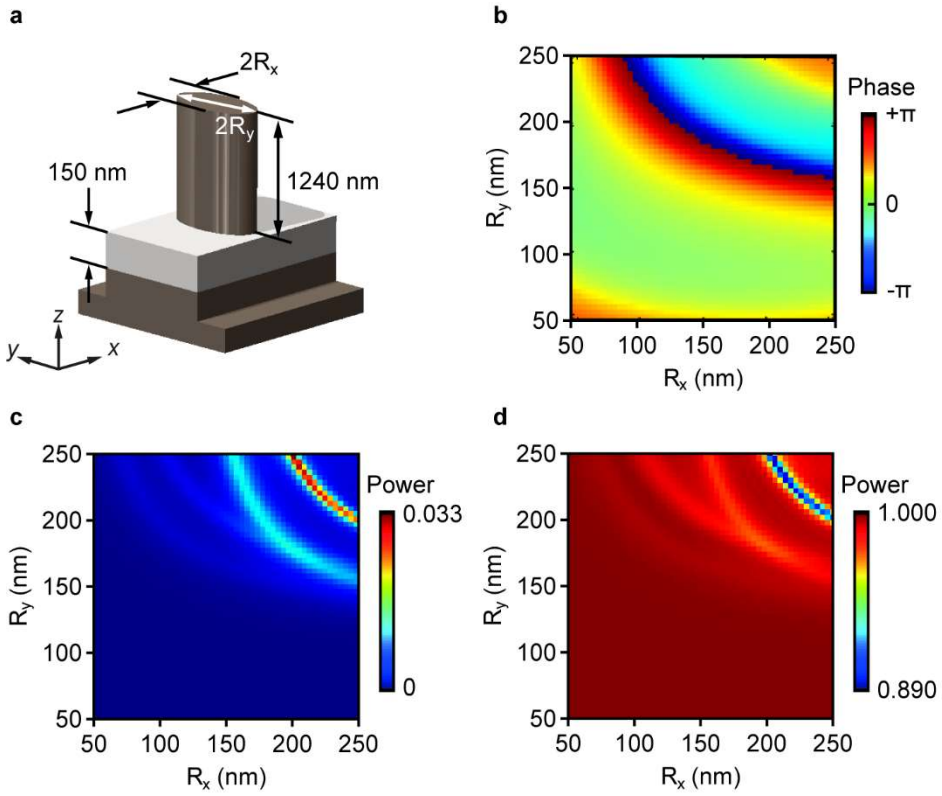

Figure 3.3 Optical properties of individual meta-atoms. (a) Schematic of a meta-atom, which from the top consists of a Si nanopillar ($1240\ nm$ in height), a SiO_2 spacer layer ($150\ nm$ in thickness), and a Si rib waveguide ($220\ nm$ in core thickness and $100\ nm$ for the rib). The whole meta-atom is on top of a SiO_2 buried oxide layer (not depicted). The schematic is not drawn to scale. (b-d) Optical properties simulated for a library of meta-atoms, with the free-space wavelength λ_0 taking a representative value of $1600\ nm$. All the meta-atoms have an elliptical cross section in the xy plane, and the principal semi-axis dimensions R_x and R_y are tuned from 50 to $250\ nm$ at a step of $4\ nm$. (b) Phase of off-chip light scattering, normalised with respect to the phase of the input light. The values are taken at a height of approximately $2.5\ \mu m$ above the centre of the bottom surface of each nanopillar. (c) Corresponding emission power of meta-atoms normalised against that of the input light. The values are taken at the

same height and from an integration window of $12\ \mu m$ by $4\ \mu m$. (c) Residual power that remains confined in the waveguide, taken at the exit yz plane of the waveguide and normalised against that of the input.

Figure 3.3.(b-d) show the numerically simulated electromagnetic properties of a large group of meta-atoms, covering the phase of the light scattered into free space [Figure 3.3.(b)], its emission power [Figure 3.3.(c)], and the power of the transmitted light that remains confined in the waveguide [Figure 3.3.(d)]. The simulation was conducted using a commercial finite-difference time-domain solver (FDTD Solutions, Lumerical). Here, the free-space wavelength λ_0 of the input light was $1600\ nm$. As seen in Figure 3.4 below, it was the peak wavelength of a WGM resonance, as well as the central wavelength of the whole spectrum investigated here (from $1550\ nm$ to $1650\ nm$). The refractive indices of Si and SiO_2 were set as 3.476 and 1.444, respectively [132]. In each meta-atom, the rib Si waveguide had a core thickness of $220\ nm$, a core width of $500\ nm$, and a slab thickness of $100\ nm$ [Figure 3.3.(a)]. The SiO_2 buffer layer above the core had a thickness of $150\ nm$, and the nanopillar further above had a height of $1240\ nm$. The waveguide was in single mode, and the fundamental TE mode was used as the input for all the analysis in this work. All the nanopillars had an elliptical cross section in the xy plane, and they differed in their principal semi-axis dimensions R_x and R_y. One of the principal axes was always along the waveguide [i.e., the x-axis in Figure 3.3.(a)], creating a mirror symmetry with respect to the vertical xz plane in all the meta-atoms. This mirror symmetry eliminated polarisation rotation in the light scattering and simplified the analysis. It is worth noting that, although the waveguide shown in Figure 3.3.(a) later constitutes a curved segment of a microring, it is treated as straight at this step of analysis. This is a good approximation, considering the large contrast in length between an individual meta-atom ($0.63\ \mu m$) and the circumference of the microring ($25.13\ \mu m$ along its centre).

The phase of the output light [Figure 3.3.(b)] is the most important parameter to consider in the metasurface design. Here, R_x and R_y are tuned independently from 50 to $250\ nm$ at a step of $4\ nm$, creating a total of $51 \times 51 = 2601$ meta-atoms for selection. The phase values are taken at approximately $2.5\ \mu m$ above the bottom plane of the nanopillars. They are with respect to the input, which is launched into the waveguide $5\ \mu m$ before the centre of the meta-atom. The phase map possesses these three main features: (1) it provides the full 2π phase coverage; (2) it consists of multiple curved bands; (3) it is roughly symmetric with respect to the diagonal line that connects the smallest nanopillar ($R_x = R_y = 50\ \mathrm{nm}$) and the largest nanopillar ($R_x = R_y = 250\ \mathrm{nm}$). These features have been observed recently in Si nanopillars that are in direct contact with a strip waveguide [76]. I can consequently draw the same conclusion here, that the output phase seen in Figure 3.3.(b) is dominated by phase accumulated in propagation.

In addition to the output phase, the emission power [Figure 3.3.(c)] and the residual power [Figure 3.3.(d)] are another two important parameters for meta-atom selection. Different from metasurfaces that function under the illumination of freely propagating light, the metasurface here is driven by a WGM, which can easily be disturbed by the light scattering of meta-atoms. For the results of Figure 3.3.(b) to serve as a good lookup table [130] to predict the device output wavefront, this disturbance has to be at a small level. To monitor this disturbance, I have simulated not only the emission power of individual meta-atoms [Figure 3.3.(c)] but also the power that remains in the waveguide [Figure 3.3.(d)]. The values of the former are extracted at the same xy plane used for Figure 3.3.(b), by integrating the power outflow within a rectangular area of $12\ \mu m$ by $4\mu m$. For the residual power shown in Figure 3.3.(d), the integration is conducted at the exit yz plane, which is $5\ \mu m$ behind the central axis of the nanopillar.

Both Figure 3.3.(c) and 3.3.(d) show that the nanopillar-induced mode perturbation is overall very weak. After normalisation against the input power, slightly more than 95% of nanopillars have a scattering efficiency below 1% [Figure 3.3.(c)] and a residual efficiency above 95% [Figure 3.3.(d)]. These nanopillars are considered to have a weak perturbation to the waveguide mode (consequently, a weak perturbation to the WGM in a microring). This weak perturbation benefits from the use of the SiO_2 buffer layer, which can regulate the strength of the evanescent coupling between the Si waveguide and the Si nanopillars. Its thickness is chosen as $150\ nm$ here, as a result of balancing the WGM mode integrity against the output efficiency in the meta-device.

3.3 In-plane transmission of the meta-device

Here, an example device is designed based on the results of the previous section. Because the radius of the microring is $4\ \mu m$, and the effective index is 2.56, the WGM at $1600\ nm$ has $m = 40$ based on Eq. (2.26). Therefore, when 40 nanopillars are placed uniformly along the waveguide, the topological charge at $1600\ nm$ equals the number of super unit cells. These 40 nanopillars are divided into eight repeating super unit cells, with each super unit cell containing five different nanopillars. The properties of all the meta-atoms in a super unit cell are listed in Table 3-1. The residual efficiency of these 5 nanopillars are over 98%, and the emission efficiency for each pillar is around 0.2%. The gap between the access waveguide and microring is set to be $50\ nm$. This value facilitates critical coupling and can be fabricated following standard nanofabrication procedures.

Table 3-1 Properties of all five meta-atoms in a super unit cell for $1600\ nm$ wavelength

Number of pillars	#1	#2	#3	#4	#5
$R_x\ (nm)$	114	114	134	70	126
$R_y\ (nm)$	222	246	246	226	182
Emission phase (rad)	4.7881	6.2650	0.7080	2.5843	3.5752
Emission efficiency	0.24%.	0.29%.	0.26%.	0.17%.	0.24%.
Residual efficiency	99.35%.	98.77%	99.25%	99.60%	99.43%

Figure 3.4 shows the in-plane transmission of the example meta-device. The intrinsic phase difference θ between adjacent nanopillars is approximately $2\pi/5$, resulting in a linear phase ramp along the microring that takes the value of $n = -8$.

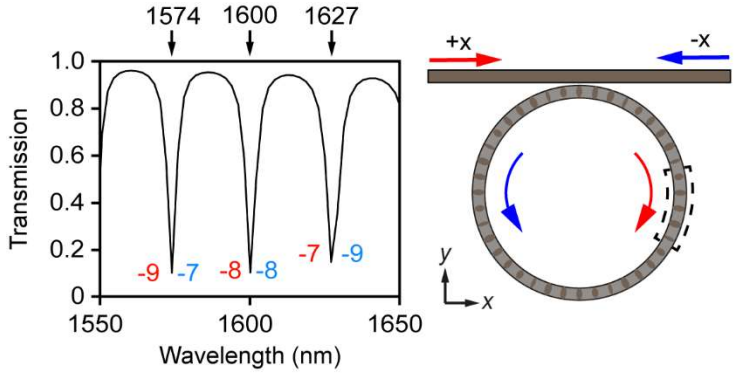

Figure 3.4 Transmission of the example meta-device. The spectrum is independent of the input direction, which is along either $+x$ or $-x$. Nevertheless, the OAM value of the vortex beam is direction dependent. At the three resonance wavelengths of 1574, 1600, and 1627 nm, its value is -9, -8, and -7 (labelled in red), respectively, under the $+x$ input. Under the opposite input, the values are instead -7, -8, and -9 (labelled in blue).

The transmission spectrum shown in Figure 3.4 is invariant with incident direction, with the meta-device being a time-independent linear system that obeys the Lorentz reciprocity theorem. It features three sharp dips at $1574\ nm$, $1600\ nm$, and $1627\ nm$. Each dip is associated with a WGM inside the microring. The values of the azimuthal order m are 41, 40, and 39, which are obtained by counting the optical cycles inside the microring. Note that the value of q in Eq. (3.1) is wavelength independent and stays 40.

Interestingly, although they produce identical transmission spectra, the $+x$ incident light and the $-x$ incident light differ in their vertical emission. By using Eq. (3.2), the values of l_{+x} (i.e., the

topological charge under the $+x$ incidence) and l_{-x} (i.e., that under the $-x$ incidence) are calculated for each WGM and specified in Figure 3.4. For the resonances at $1574\ nm$, $1600\ nm$, and $1627\ nm$, l_{+x} is -9, -8, and -7, respectively, while l_{-x} is -7, -8, and -9, respectively. Asymmetric emission, defined above as $l_{+x} + l_{-x} \neq 0$, is observed at all these three resonance wavelengths. It is worth highlighting that this result does not violate the Lorentz reciprocity theorem, because reversing the input direction here does not constitute a swap between input and output.

3.4 Whispering gallery mode and vortex beams at 1600 nm

In this section, I select one of the three WGM resonances, which has a free-space wavelength λ_0 of 1600 nm, and study it in detail (Figure 3.5). Figure 3.5.(a) and 3.5.(b) show the field confinement of the bus waveguide and the microring. For both the $+x$ and the $-x$ inputs, most of the input light is coupled into the microring, building up a strong WGM resonance. Due to this strong coupling, the residual field that remains inside the bus waveguide behind the microring is very weak, which is congruent with the transmission dip seen in Figure 3.4. We can see that Figure 3.5.(a) and 3.5.(b) are almost mirror images of each other with respect to the vertical yz plane.

Interestingly, the mirror symmetry of the near field [Figure 3.5.(a) and 3.5.(b)] is not transferred to the emission into the far field [Figure 3.5.(c) and 3.5.(d)]. Instead of being a pair of mirror images, the two output waves are closer to being identical copies. They both possess eight-fold rotational symmetry to a good degree, and for both of them the vortex spirals in a clockwise direction towards its centre. This leads to $l_{+x} = l_{-x} = -8$. The sign here can also be verified by tracing the evolution of the electric field along the beam axis [127]. Relatively small differences exist between Figure 3.5.(c) and 3.5.(d), and they are attributed to factors such as small fluctuations in the output phase gradient and the output power among the meta-atoms. The device output efficiency, defined as the power ratio of the output vortex beam and the input guided mode, is 11.0% and 10.9% for the $+x$ and the $-x$ incidence, respectively.

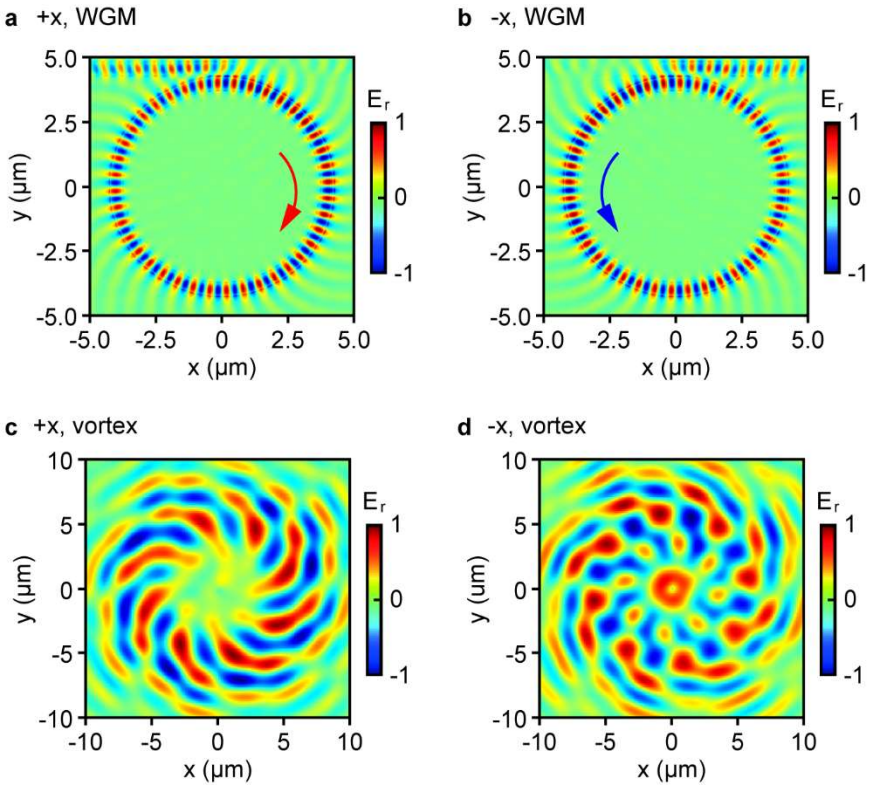

Figure 3.5 Properties of the meta-device at a representative WGM resonance wavelength of 1600 nm. (a, b) The radially polarised electric field E_r inside the microring at (a) the $+x$ incidence and (b) the $-x$ incidence. The field is taken at the middle height of the Si waveguide. (c, d) The corresponding E_r field above the microring at (c) the $+x$ incidence and (d) the $-x$ incidence. The field is taken at 8 μm above the top of the Si waveguide. All four panels are the top view. Each panel is normalised against its respective peak value.

This observation of $l_{+x} = l_{-x} = -8$ at 1600 nm can be interpreted by using Eq. (3.2). The order of the WGM inside the microring, which can be identified in Figure 3.5.(a) and 3.5.(b), is identical to the number of nanopillars on top of the microring, i.e., $m = q = 40$, at this wavelength. Eq. (3.2) consequently gives $l_{+x} = l_{-x} = n = -8$, which fits well with the numerical results shown in Figure 3.5.(c) and 3.5.(d). Similar verification of Eq. (3.2) is also conducted for the two other WGM wavelengths (i.e., $1574\ nm$ and $1627\ nm$), and the analytical results all fit with the numerical ones, illustrated in Figure 3.6.

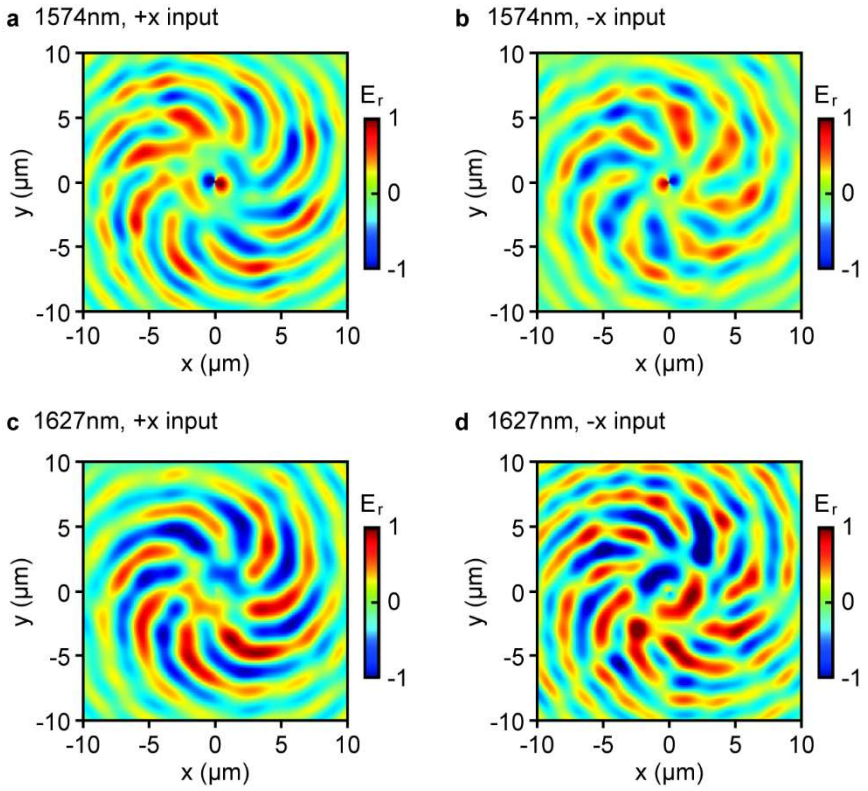

Figure 3.6 The E_r fields of the vortex beam emitted by the meta-device, at (a) 1574 nm under the $+x$ incidence, (b) $1574\,nm$ under the $-x$ incidence, (c) $1627\,nm$ under the $+x$ incidence, and (d) $1627\,nm$ under the $-x$ incidence. The field is taken at $8\,\mu m$ above the top of the Si waveguide. All four panels are the top view. Each panel is normalised against its respective peak value.

3.5 Vortex beam mode analysis

I notice that mode purity, a property critical for many potential applications such as free-space optical communications, is seldom analysed in the literature on integrated OAM generation. The OAM beam emitted by the meta-device discussed here is a vector vortex beam. A vector vortex beam is a kind of structured light that possesses not only OAM but also spatially inhomogeneous states of polarisation [133, 134], and this full-vector feature makes mode purity analysis even more challenging. To provide insight on this challenge, I present in this section a method of mode purity analysis and conduct calculations for the WGM wavelength of $1574\,nm$ as an example (Figure 3.7).

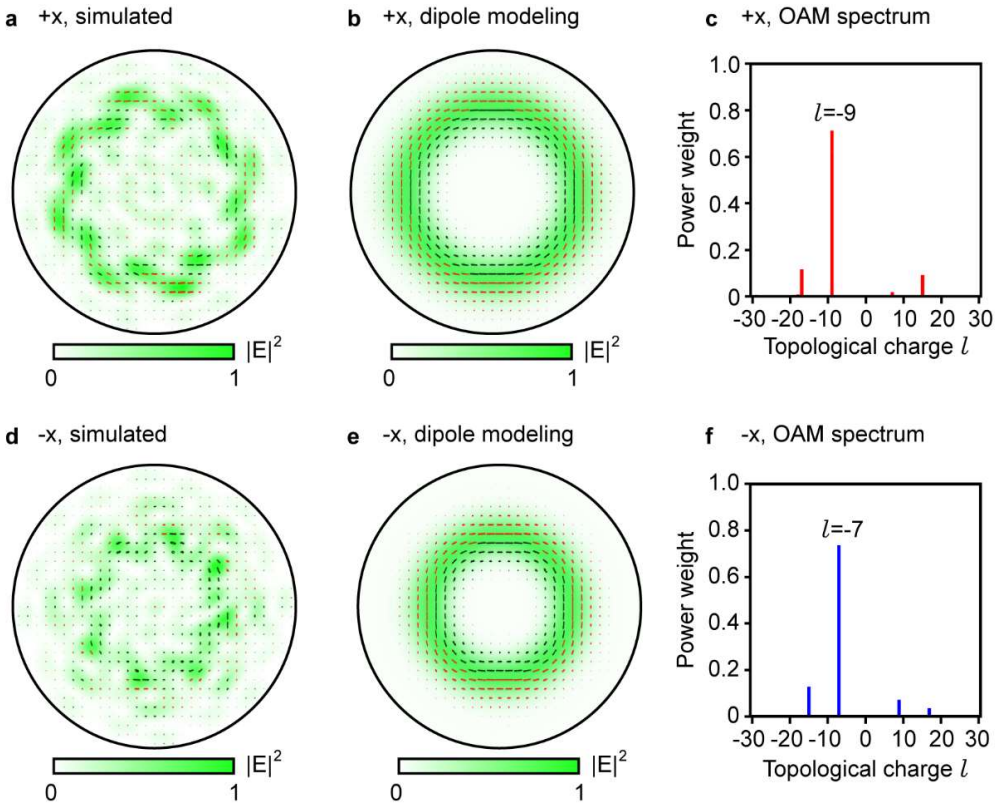

Figure 3.7 Mode analysis for the output vortex beam. The wavelength is $1574\ nm$, another WGM resonance wavelength that is different from Figure 3.5. (a) Intensity distribution of the output under the $+x$ incidence, overlaid with the polarisation distribution. The map shows the hemisphere, where every point is one metre away radially from the device. At locations that have a strong local intensity, the polarisation is dominantly in the azimuthal direction. It can possess a small degree of ellipticity, which is expressed by using the red colour (for the right-handed rotation, defined from the point of view of the receiver) and the black colour (for the opposite handedness). (b) Corresponding intensity and field distribution for an ideal device, obtained by modelling all the meta-atoms as infinitesimal electric dipoles. (c) The OAM spectrum extracted from panel (a), utilizing only the azimuthal component of its electric field. (d-f) Corresponding results for the $-x$ input, showing (d) the intensity and the polarisation distribution of the meta-device, (e) the distributions of an ideal device, and (f) the OAM spectrum extracted from the azimuthal field of the panel (d).

The first step of the method is to identify the dominant polarisation component in the output. Figure 3.7.(a) shows the output at one metre away from the meta-device. Its intensity distribution has roughly a ring shape but lacks continuous rotational symmetry, which indicates that the OAM carried by the beam has a spectrum rather than a single value (an example of similar features can be found in the interference patterns shown in Ref. [135]). The polarisation of the output changes in both ellipticity and direction with location. It is dominantly along the azimuthal direction at locations that bear significant intensity. As a reference, I have used the dipole modelling, where

each meta-atom is approximated with an infinitesimal electric dipole [46], to predict the ideal output beam, which is plotted in Figure 3.7.(b). The differences between Figure 3.7.(a) and 3.7.(b) are attributed to the deviation of the meta-atoms from the ideal electric dipoles, which appear as a small but finite fluctuation in their output phase and output strength. The cause of the fluctuation is that the phase and emission efficiency of nanopillars in a super unit cell have some error compared to the ideal case, as listed in Table 3-1. The emission efficiencies of nanopillars are not the same, and the phase difference between two adjacent nanopillars is not exactly $(2\pi)/5$, as illustrated in Figure 3.9. Another reason for this fluctuation is that the nanopillar is selected for the input wavelength of $1600\,nm$. Figure 3.8 illustrates the properties of the nanopillars at three different wavelengths. There are some recognisable differences about the phase and emission intensity among these three wavelengths.

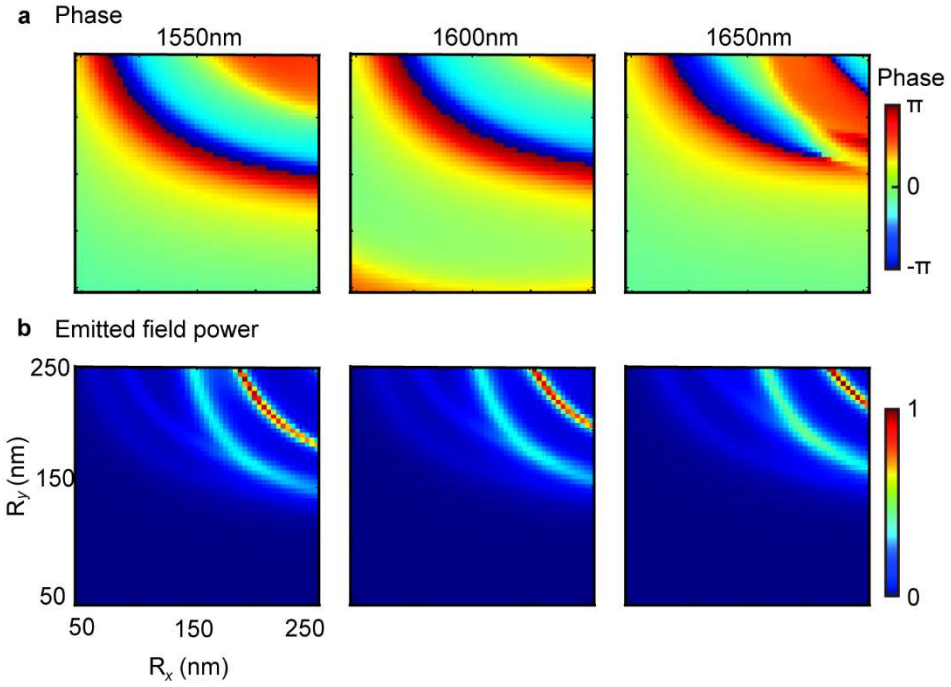

Figure 3.8 Optical properties of individual meta-atoms at different wavelengths ($1550\,nm$, $1600\,nm$, and $1650\,nm$). Optical properties were simulated for a library of meta-atoms. All the meta-atoms have an elliptical cross section in the xy plane, and the principal semi-axis dimensions R_x and R_y are tuned from 50 to $250\,nm$ at a step of $4\,nm$. (a) Phase of off-chip light scattering at different wavelengths, normalised with respect to the phase of the input light. The values are taken at a height of approximately $2.5\,\mu m$ above the centre of the bottom surface of each nanopillar. (b) Corresponding emitted power at different wavelengths, normalised against the maximum value in each map. The values are taken at the same height and from an integration window of $12\,\mu m$ by $4\,\mu m$.

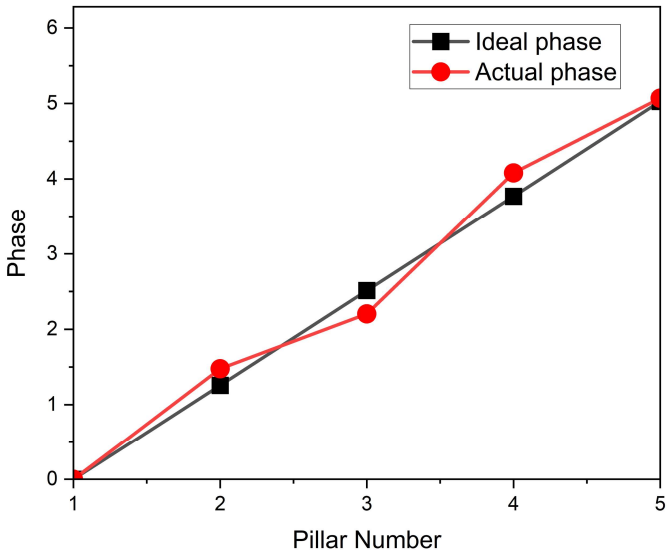

Figure 3.9 Comparison between the phase gradient obtained from simulations and the ideal phase gradient at $1600\ nm$ wavelength. The phases of those 5 nanopillars increases from 0 to 2π.

As Figure 3.7 reveals the existence of a single dominant field component, we can approximate the vector vortex beam with a scalar vortex beam. This scalar vortex beam retains the intensity distribution of the original vector vortex beam. The spatial dependence of its phase is also the same as that of the azimuthal component in Figure 3.7.(b). It nevertheless has an identical state of polarisation across the plane (hence a scalar vortex beam). This scalar vortex beam E can then be considered as a weighted superposition of the standard Laguerre-Gaussian modes $LG_l(r,\varphi)$

$$E = \sum_l C_l \ LG_l(r,\varphi) \tag{3.3}$$

where r and φ are the axial distance and the azimuthal angle of the cylindrical coordinate system, respectively. In this mode decomposition, only the Laguerre-Gaussian modes that have a zero radial index are considered [127], based on the intensity distribution of Figure 3.7.(a). Figure 3.7.(c) shows the spectrum of the weight $|C_l|^2$ for a broad range of l (equivalently l_{+x}, as the incident direction is $+x$ here) from -30 to 30. The dominant component is $l_{+x} = -9$, which has a weight of 71%. This mode analysis method is then applied to the output under the $-x$ incidence [Figure 3.7.(d), with the ideal output also provided as Figure 3.7.(e) for comparison], and the extracted OAM spectrum is shown in Figure 3.7.(f). The dominant component is $l_{-x} = -7$, which has a weight of 74%. Both the dominant l_{+x} and l_{-x} are the same as the analytical values predicted in Figure 3.4.

To further verify this method of OAM spectrum analysis, we deliberately pick a different component of the output electric field and repeat the analysis. The component used for the verification is the radial electric field, which is orthogonal to the azimuthal component used for

Figure 3.7. The OAM spectra obtained from the analysis are plotted in Figure 3.10. Under the $+x$ incidence, $l_{+x} = -9$ is the dominant component and has a weight of 70%. Under the $-x$ incidence, $l_{-x} = -7$ is the dominant component and has a weight of 74%. As compared to Figure 3.7, this analysis produces identical values of the dominant l_{+x} and l_{-x}, as well as almost identical values of their weights. These results further verify the validity of our method.

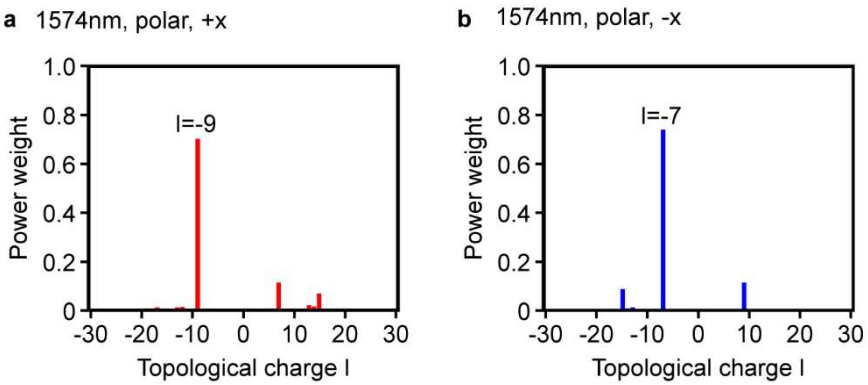

Figure 3.10 The OAM spectra of the emitted field at $1574\ nm$, obtained by analysing the radial component of the output electric field, as opposed to the azimuthal component used in Figure 3.7. The incident light is along (a) the $+x$ direction and (b) the $-x$ direction. The dominant term of both spectra is (i.e., -9 and -7) is identical to that of Figure 3.7, confirming the validity of our mode decomposition method.

Before concluding this work, it is worth discussing the use of the OAM spectrum analysis that we have developed here. In principle, the analysis can be applied to each constituent polarization component of a vector vortex beam, as shown above. Nevertheless, these factors need to be considered when applying this analysis. (1) The dominant component will provide the highest numerical accuracy. (2) Information of both the intensity distribution and the polarisation distribution is needed to identify the dominant component, as shown in Figure 3.7. (3) Thanks to the linearity of Maxwell's equations, a vector vortex beam is allowed to carry different OAM values in its different constituent components. For such kind of complicated electromagnetic fields, our analysis will generate a set of distinct OAM spectra, each revealing a specific aspect of the original field.

3.6 Conclusion

To conclude, I have proposed and numerically demonstrated a new approach for integrated vortex beam emission. This new approach hybridises two prominent existing approaches, which are based respectively on metasurfaces and angular grating-decorated microrings. In the example device discussed in detail here, this approach is realized by positioning a Si pillar-based metasurface on top of a Si microring resonator. Because the metasurface phase gradient is

intrinsic and does not switch with the direction of the input light, the conjugate symmetry that is intrinsic to conventional microring emitters is broken here. The rotation direction of the source (i.e., the circulation of the WGM inside the microring) and that of the output (i.e., the helicity of the vortex beam) are no longer coupled. This is a new phenomenon that I refer to as asymmetric vortex beam emission. It allows for a single device to produce two independent sets of OAM values, with each value accessible via a unique combination of wavelength and input direction. This feature represents a new capability for integrated OAM emissions. It is however worth clarifying that, this independence exists only at the design stage. Once a device is fabricated, the relative differences between the two sets of the OAM values will be fixed.

In addition to demonstrating this new design approach, my teammate Wangke has also developed here a new analytical method that allows for the extraction of an OAM spectrum from a vector vortex beam. The method is based on approximating the vector vortex beam as a scalar vortex beam and subsequently using this scalar vortex beam to conduct mode decomposition. The results match well with both the analytical prediction and the simulated field maps. I believe both the hybridised design approach and the OAM spectrum analysis method presented here could significantly benefit future studies on integrated vortex beam emission.

Chapter 4 THz vortex beam emitter

Metasurfaces enable a high level of control over electromagnetic waves across a broad frequency range that extends from GHz to the ultraviolet [136-140]. By imparting a judiciously designed change to the wavefront of these waves, metasurfaces can deflect a light beam towards a designated direction [67, 73], and focus it into a diffraction-limited spot [141, 142] or along a narrow line [116, 143]. It can also convert a simple optical mode (e.g., a linearly polarised plane wave or a fundamental TE mode inside a waveguide) to a far more complicated mode, such as an optical vortex with orbital angular momentum [110, 144] and a hologram that transforms with wavelength [145, 146]. In each of these cases, the key to wavefront shaping has always been considered as identifying a set of meta-atoms (i.e., unit cells of light scatterers) that differ in output phase [147]. For example, in all-dielectric metasurfaces, mechanisms such as the Mie resonance [148-150] and the effective refractive index approximation [150, 151] are commonly used in device design, for creating a gradual phase gradient that covers the full 2π cycle. This tuning in the output phase of meta-atoms is often accompanied by a variation in their output amplitude. Although simultaneous control over both the output phase and the output amplitude is feasible for some designs [152-157], most previous works have taken the approach of intentionally suppressing the amplitude variation in meta-atom selection [158]. Because of this dominance of the phase gradient-oriented design approach in metasurface research, “phase gradient metasurface” is viewed widely as a synonym of “gradient metasurface”, sometimes even as a synonym of the term “metasurface” itself.

As opposed to this phase gradient approach, I introduce in this work a different type of metasurfaces that can be referred to as an “amplitude gradient metasurface”. As the name implies, in this type of metasurfaces, the device design emphasises the amplitude gradient: the meta-atom selection can be purely based on the difference in their light scattering amplitude. As far as I know, this amplitude gradient meta-waveguide has never been proposed previously.

This amplitude gradient concept is developed for a type of metasurface converter that transforms the guided mode of a waveguide into a free-space mode that propagates off chip [159]. These metasurfaces, which are also referred to as meta-structured waveguides or meta-waveguides [159], possess features of both traditional free-space metasurfaces and leaky-wave antennas, and they represent an emerging subfield of metasurface research. They target applications such as augmented reality displays [160], LiDAR sensing [161], and free-space optical communication [162]. Various wavefront shaping functionalities have been realised on meta-waveguides, including beam deflection [110, 163], focusing [163-166], as well as the generation of vortex beams [110, 166], airy beams [167], and holograms [146, 160, 168].

According to the statement above, all of these existing metasurfaces [146, 159-161, 163-168] belong to the category of phase gradient metasurfaces. This design approach can only offer a limited effective aperture, making power projection over a long distance very difficult. Here, I propose a new, amplitude gradient-oriented design approach that allows for both a large device aperture and advanced off-chip wavefront shaping.

In the analysis below, the properties of individual meta-atoms and the general principles for their selection are first discussed in Section 4.1. A number of example devices are then designed and numerically studied, and they show these three distinct wavefronts shaping functionalities in the THz regime: beam expansion (in Section 4.2), focusing (in Section 4.3), and vortex beam generation (in Section 4.4). Their main performance characteristics are summarized in Section 4.5, which also includes a brief discussion on potential experimental challenges and future applications.

This work has been conducted in collaboration with a research group at the Department of Automation at Tsinghua University. Most results in this chapter are presented in the journal: Wen Lyu*, Jianzhi Huang*, Shengqi Yin, Xukang Wang, Jiaming Liu, Xu Fang and Hua Geng "Amplitude gradient-based metasurfaces for off-chip terahertz wavefront shaping." *Photonics Research* 11.9 (2023): 1542-1552. I designed the light focusing model (in Section 4.3) and vortex-beam-generation models (in Section 4.4) and ran all Lumerical simulations on Iridis, the high-performance computing system belonging to the University of Southampton.

4.1 Amplitude gradient-based metasurface design

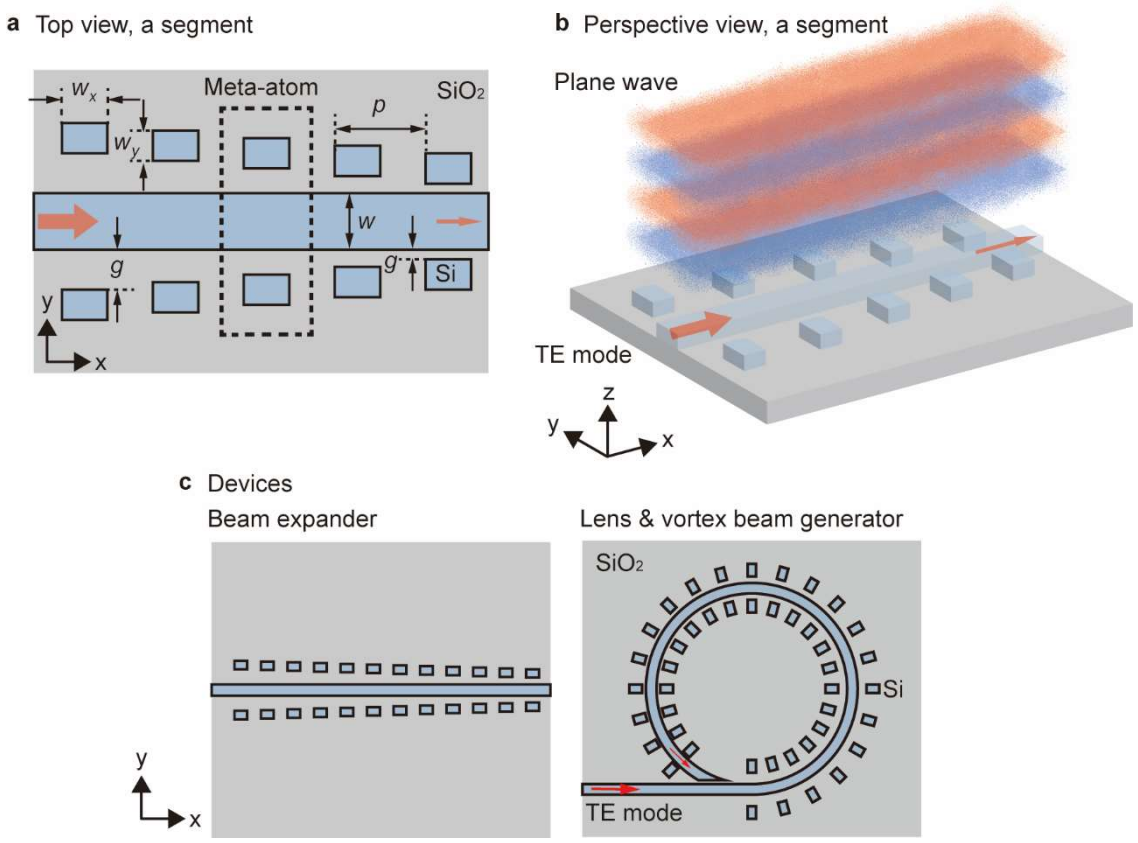

Figure 4.1 Schematic diagrams of the amplitude gradient meta-waveguides. (a) A segment of the meta-waveguide consists of a long Si waveguide and cuboid shaped Si pillars positioned symmetrically by its two sides. All the Si pillars have identical planar dimensions of w_x by w_y, and they have a constant interval of p along the waveguide. The waveguide-pillar gap g is a critical parameter to control the light scattering amplitude of each meta-atom (highlighted using the dotted line box.). (b) By judiciously selecting the values of g, the influence of the power decay in the guided mode (the two red arrows) on light scattering can be compensated and a plane wave with a large cross section can be created. (c) Two device configurations are considered in this work, where the waveguide is either straight (for plane wave generation) or bent into a circle (for focusing and vortex beam generation).

Figure 4.1 illustrates meta-waveguides designed using the amplitude gradient approach. It shows a top view [Figure 4.1.(a)] and a perspective view [Figure 4.1.(b)] of a segment of a meta-waveguide, as well as two kinds of the overall shape of the example devices analysed in this work [Figure 4.1.(c)]. The meta-waveguide consists of a long Si waveguide and many pairs of cuboid shaped Si pillars positioned by its two sides, and the whole structure is on top of a thick SiO_2 layer. The Si waveguide has a rectangular cross section that is h in height and w in width. All the Si pillars have identical planar dimensions of w_x (along the waveguide direction) and w_y (along the

orthogonal direction), and their height is the same as that of the waveguide (i.e., h). These two Si pillars in a pair are placed symmetrically by the two sides of the waveguide, at a constant periodicity of p along the waveguide. A meta-atom of this metasurface is consequently a pair of pillars and a segment of waveguide in between [Figure 4.1.(a)]. The only geometric difference between the meta-atoms is the distance between the waveguide and a side pillar, which is referred to as the gap g. As will be discussed in detail below, the gap g is a critical parameter for the amplitude gradient metasurfaces.

A starting point of this amplitude gradient design approach is to position meta-atoms with stronger scattering amplitude (i.e., efficiency) further down the waveguide [Figure 4.1.(b)]. All meta-waveguides, including both the phase gradient meta-waveguides discussed in previous works [159] and the amplitude gradient meta-waveguides proposed here, are based on scattering a guided mode off chip using a series of meta-atoms. This scattering determines the off-chip wavefront shaping, but also leads to a detrimental shadowing effect [76]. As the residual intensity decreases further down the waveguide, the phase gradient approach always results in a limited effective aperture [159]. By comparison, the amplitude gradient approach proposed here can compensate for this shadowing effect and remove this limitation on effective aperture [Figure 4.1.(b)]. This feature is demonstrated in the first set of example devices in Section 4.2, where the central waveguide is straight [Figure 4.1.(c)]. Bending the waveguide into a loop [Figure 4.1.(c)] can further sculpt the output wavefront into different shapes, which are demonstrated in the second and third sets of example devices in Section 4.3 and 4.5, respectively.

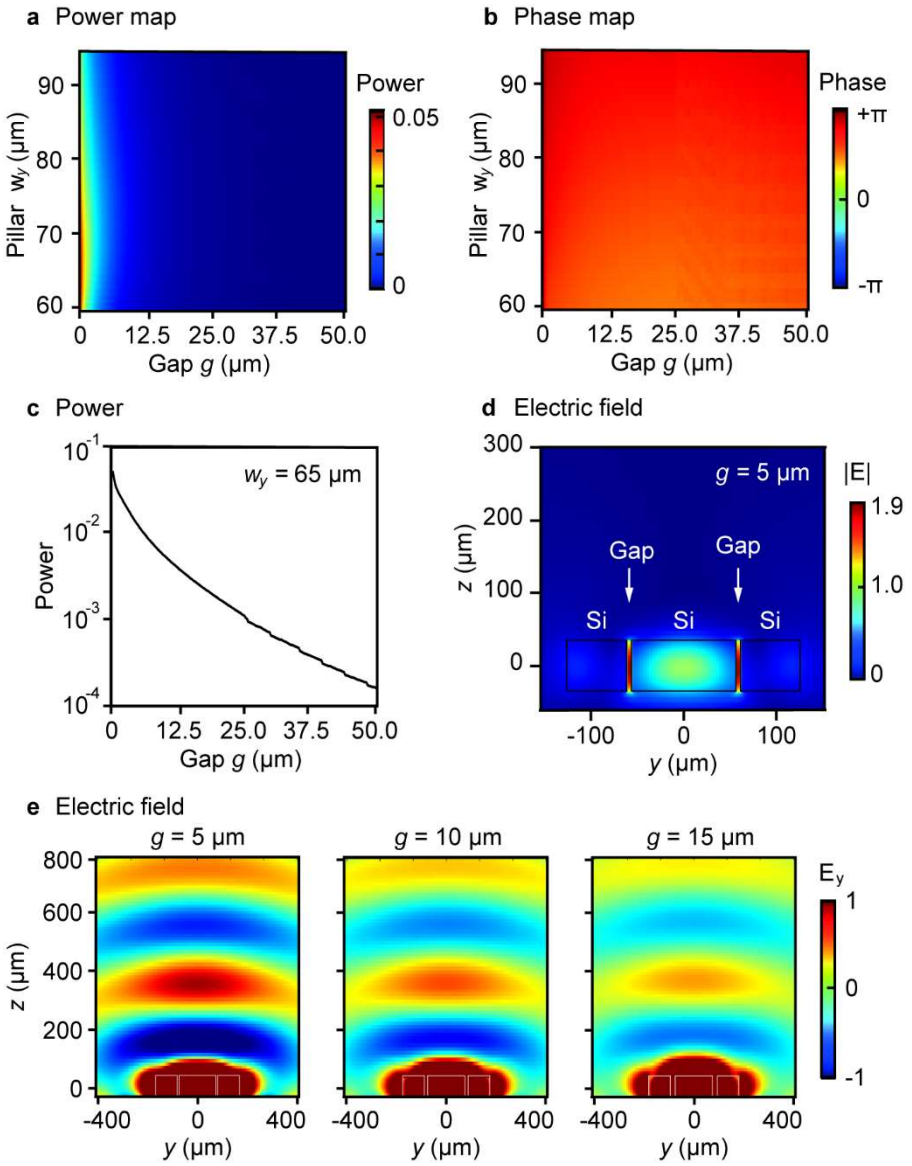

Figure 4.2 Light scattering of individual meta-atoms. The input mode is TE mode with the wavelength of 375 μm. The value of w_x is fixed at 100 μm. (a) The scattered power after normalisation against the input guided mode power, with w_y scanned from 60 to 94 μm and g from 0.25 to 50 μm. (b) The scattered phase in the same parameter ranges. (c) The dependence of the output power on g with w_y fixed at 65 μm. The data is taken from the horizontal line of $w_y = 65$ μm in panel (a). (d) The electric field distribution at the yz middle plane of a representative meta-atom, which has $w_y = 65$ μm and $g = 5$ μm. The field is normalised against that at the centre of the waveguide. (e) The same meta-atom is plotted again at a different scale, and it is compared against two other meta-atoms. The only geometric difference of these meta-atoms is the value g, which takes three representative values of 5, 10, and 15 μm. All three panels are plotted at the same scale to best visualise the free-space light. At this scale, the features of the near field confined to the surface of the meta-atoms are not resolved.

Figure 4.2 shows the numerically simulated electromagnetic properties of a set of meta-atoms. The simulation, for this figure and all that follow, was conducted using a commercial finite-difference time-domain solver (FDTD Solutions, Lumerical). Following our recent works on metasurface mode converters [169, 170], all the devices were designed to work at $0.8\ THz$, which corresponded to a free-space wavelength λ_0 of $375\ \mu m$. Both Si and the underlying SiO_2 were treated as lossless, and their permittivity [171, 172] were 11.67 and 3.84, respectively. The central Si waveguide was single mode and had a height h of $70\ \mu m$ and a width w of $112\ \mu m$. The fundamental transverse electric (TE) mode had an effective index of 2.50, which corresponded to an effective wavelength λ_{eff} of $150\ \mu m$. For the Si side pillars, their height was set as $70\ \mu m$, the same as that of the waveguide. The planar dimensions of w_x, w_y and g were treated as free parameters in device design and analysed as below.

Figures 4.2.(a) and 4.2.(b) show the power and the phase of light scattered by individual meta-atoms, respectively. In parametric sweeping, the value of w_x is fixed at 100 μm. The value of w_y is tuned from $60\ \mu m$ to $94\ \mu m$ at a step of $1\ \mu m$, and g is tuned from $0.25\ \mu m$ to $50\ \mu m$ at a step of $0.25\ \mu m$. The power shown in Figure 4.2.(a) is obtained by integrating the output over a window of $1600\ \mu m$ (along the waveguide) by $800\ \mu m$ (in the orthogonal direction), which is located at $480\ \mu m$ (i.e., slightly over one wavelength) above the centre of the meta-atom. The value is very small throughout the whole simulated parameter range [Figure 4.2.(a)]. Its highest value is only 0.052 after normalisation against the input power, which occurs at $w_y = 65\ \mu m$ and $g = 0.25\ \mu m$ (i.e., the smallest value of g considered in the simulation). In the whole simulated range of w_y, the power rapidly decreases as g increases, and appears to be almost zero in Figure 4.2.(a) once g is beyond approximately $10\ \mu m$. To show this dependence on g more clearly, the values along the horizontal line of $w_y = 65\ \mu m$ are extracted from Figure 4.2.(a) and plotted in Figure 4.2.(c). The power decreases almost exponentially as g increases and varies by over two orders of magnitude in the simulated range of g.

In sharp contrast to this exponential dependence of the power on gap g, the phase shows little sensitivity to both w_y and g [Figure 4.2.(b)]. The values shown in Figure 4.2.(b) are taken at $480\ \mu m$ above the centre of the meta-atom (i.e., the centre of the power integration window mentioned above). These phase values are with respect to the input, which is launched at $725\ \mu m$ before the centre of the meta-atom. In the investigation of phase gradient metasurfaces, such phase maps are always plotted over a full 2π range to show the extent of phase coverage [158]. I follow the same style in plotting Figure 4.2.(b) and obtain here a phase map that appears to be uniform.

To interpret the far-field results of Figure 4.2.(a-c), Figures 4.2.(d) and 4.2.(e) show the electric near-field distributions of a few representative meta-atoms. Figure 4.2.(d) shows the electric field

at the yz middle plane of a meta-atom that has $w_y = 65$ μm and $g = 5$ μm. Field enhancement is observed in the gaps between the central waveguide and the side pillars, a phenomenon similar to the field confinement observed in Si slot waveguides designed for telecom wavelengths [173]. At the amplitude scale of Figure 4.2.(d), no scattered field can be discerned due to its small amplitude. To highlight the scattered field, the same field map is plotted at a different scale in Figure 4.2.(e), where two other meta-atoms are also shown for comparison. The only geometric difference of the three meta-atoms in Figure 4.2.(e) is in g, which is 5, 10, and 15 μm. In all three maps, the scattered wave looks like a spherical wave in the far field and does not reveal the intricate geometry of the meta-atoms. Most importantly, these maps show a clear contrast in the output amplitude and a constant output phase.

The amplitude gradient seen in Figure 4.2 is exploited in the following sections, in order to generate a plane wave in Section 4.2, a focus in Section 4.3, and a vortex beam that carries a finite value of orbital angular momentum in Section 4.4. Section 4.2, all the meta-atoms are identical, with $w_x = 100$ μm and $w_y = 65$ μm. In Sections 4.3 and 4.4, the waveguide is bent from a straight line into a circle. To accommodate more pillars along the circle, the values of w_x (now the pillar dimension along the waveguide) and w_y (still the orthogonal planar dimension of the pillars) are swapped in value. In essence, the cuboid Si pillars used in this work are all of the same size, and the different wavefront shaping functionalities are obtained by changing the shape of the waveguide (either a straight line or a circle) and the value of the gap g.

Before discussing the details of each of the three example functionalities below, it is worth mentioning the influence of the gap dependence shown in Figure 4.2.(c) on device design. I conducted design optimisation in our simulation and found that for each functionality, good results can be obtained by simply adjusting the value of g at a constant step, with the smallest g positioned at the end of the waveguide. This observation can be understood by considering the absolute scattering power of each meta-atom. For all the devices discussed below, the waveguide can be approximated as a leaky waveguide in which the residual power decreases exponentially with propagation distance. With a constant decrease in g along the waveguide, the meta-atoms instead have an almost exponential increase in their scattering efficiency with their distance to the waveguide entrance. These two factors can result in increased uniformity of the output intensity along the waveguide, which underpins the functionalities discussed in the following sections. Regarding the detailed device design, more information is provided in the respective section below.

4.2 Beam expander as the first functional device

In this section, we numerically demonstrate the first functionality obtained by using the amplitude gradient design approach, which is off-chip plane wave generation. The aim here is to expand a guided wave, which is highly constrained in its cross section, into a plane wave with a large beam width, which can then be further modulated to enable functionalities such as beam steering and focusing. For a waveguide decorated with periodic structures that extends along the x-axis in the xy plane (as shown in Figure 4.1), we can define a deflection angle ϑ for the output light with respect to the vertical $+z$ direction. This angle ϑ can be expressed as [76]

$$\vartheta = \arcsin\left[\lambda_0 \left(\frac{1}{\lambda_{eff}} + n\frac{1}{p} + \frac{k_p}{2\pi}\right)\right] \tag{4.1}$$

where λ_0 is the free-space wavelength, λ_{eff} is the effective wavelength inside the waveguide, n is an integer that describes the diffraction order, p is the periodicity of the scatterers, and k_p is the phase gradient. Note that this equation is obtained by matching the guided mode and the output light in their in-plane momentum, which brings to it a broad scope of application. It can be applied to different waveguide-driven devices, including phase gradient metasurfaces (where $k_p \neq 0$), conventional gratings (where $k_p = 0$ and all the light scatterers are identical), and the amplitude gradient metasurfaces proposed here (where $k_p = 0$ and all the light scatterers are unique). As $k_p = 0$ here, we can see that if $p = \lambda_{eff}$, only one diffraction order of $n = -1$ exists, which has a deflection angle $\vartheta = 0°$. The output light should leave the meta-waveguide vertically into free space. This behavior is confirmed by using the two devices in Figure 4.3. One with 100 meta-atoms and the other with 1000, are numerically studied. The central waveguide is $70\ \mu m$ in height and $112\ \mu m$ in width. The side pillars are $70\ \mu m$ in height. And for obtaining a maximum intensity manipulation range, based on the property in Figure 4.2., the values of w_x (the planar dimension along the waveguide) and w_y (the planar dimension in the orthogonal direction) are $100\ \mu m$ and $65\ \mu m$, respectively. In the 100-unit device, the meta-atoms have a periodicity of $144.5\ \mu m$, and the gap g decreases from $19.8\ \mu m$ to 0 at a step of $0.2\ \mu m$ in the forward direction. In the 1000-unit device, the meta-atom periodicity is $149.5\ \mu m$, and the gap g decreases from $49.95\ \mu m$ to 0 at a step of $0.05\ \mu m$ in the forward direction.

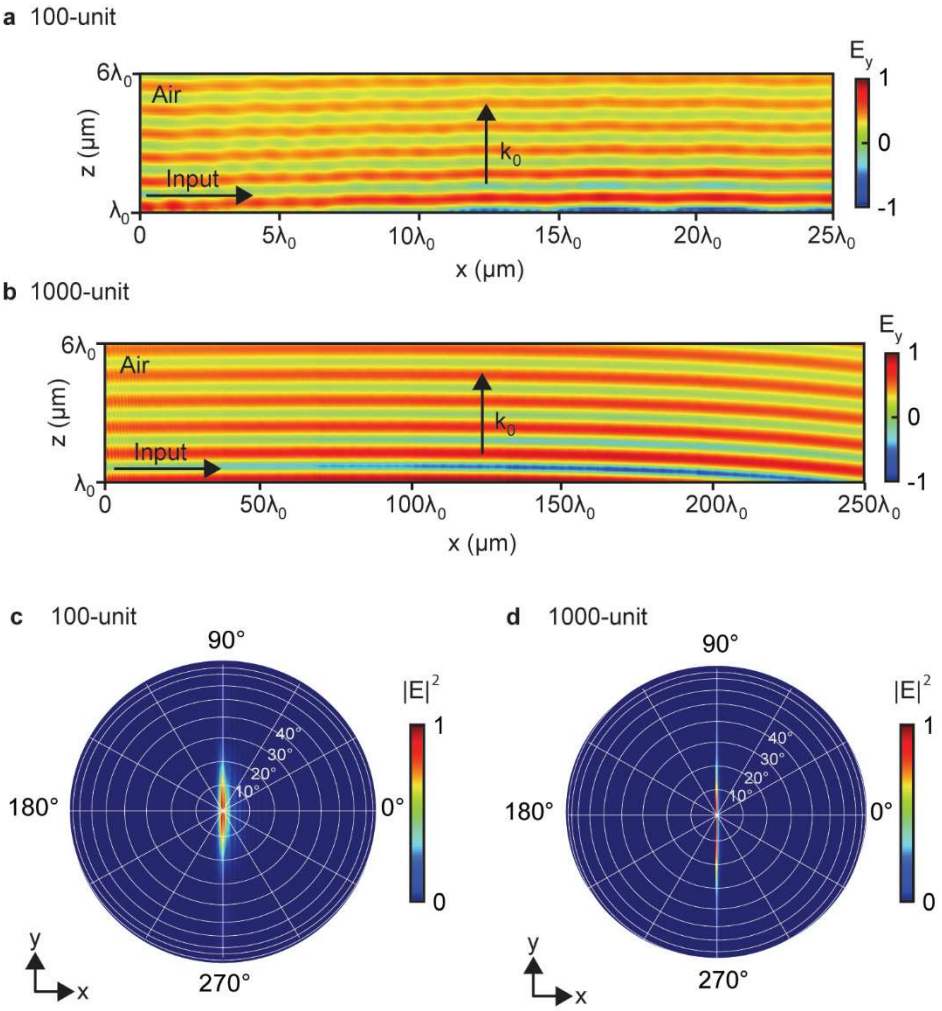

Figure 4.3 Off-chip plane wave generation in two amplitude-gradient meta-waveguides. In both devices, the input guided mode propagates towards the $+x$ direction, generating a free space beam that propagates vertically towards the $+z$ direction. The number of meta-atoms is (a) 100 and (b) 1000. Both field maps show an area in the central xz plane, with the bottom edge of the maps one wavelength above the middle plane of the metasurface. The whole length of the two devices is approximately 40 and 400 times of the free-space wavelength λ_0, and only a section of $25\lambda_0$ and $250\lambda_0$ is shown here. Due to space constraints, only the first map is plotted to scale. The second map is significantly compressed along the *x*-axis. This compression amplifies any small tilting in the wavefronts in the visualization. (c, d) Corresponding far-field distributions, for the (c) 100-unit and (d) 1000-unit devices.

Figure 4.3 shows the off-chip beam deflection of two meta-waveguides, where the number of meta-atoms is 100 and 1000. Design optimisation has been conducted for both devices, with the aim of obtaining a flat and horizontal wavefront. In the optimization, we have noticed that the meta-atom periodicity needs to be slightly adjusted from the analytical value of $150\ \mu m$ for a nearly vertical emission. The periodicity p is consequently set as $144.5\ \mu m$ and $149.5\ \mu m$ for the 100-unit and the 1000-unit devices, respectively. This adjustment in p is attributed to the small

influence of the side pillars on the effective index of the waveguide, as well as the existence of a small but finite phase gradient [i.e., the k_p in Eq. (4.1) is not strictly zero].

Figure 4.3.(a) and 4.3.(b) are field maps of the output field along the waveguide direction. Both maps show a plane wave with a nearly flat wavefront and a nearly uniform amplitude. It is worth noting that, due to space constraints, Figure 4.3.(b) is significantly compressed along the x-axis. Once the x and z axes are plotted at the same scale, as in Figure 4.3.(a), the tilting of the wavefront currently seen in Figure 4.3.(b) diminishes and becomes barely noticeable.

To quantify the beam deflection performances, the far-field radiation is calculated for both devices and shown in Figure 4.3.(c) and 4.3.(d). Both radiation maps show a bright spot at the centre, congruent to the field maps of Figure 4.3.(a) and 4.3.(b). Both spots are relatively broad along the *y*-axis. This is because only a single waveguide is simulated here for both devices, which already approaches the limit of the computing power available to us. The spots will become narrower along this axis by repeating the same meta-waveguide at a subwavelength interval. Along the x-axis, detailed analysis reveals that the deflection angle is $-0.18°$ and $0.08°$ in Figures 4.3.(c) and 4.3.(d), respectively, both very close to the target value of $0°$. The full width at half maximum (FWHM) of the emission lobe along the x-axis is $2.41°$ in Figure 4.3.(c), and it decreases to $0.26°$ in Figure 4.3.(d). This change in the FWHM value originates from an increase in the emission aperture, which accompanies the increase in the number of meta-atoms.

As mentioned in the previous section, as compared to the existing phase gradient design approach, a clear advantage of the amplitude gradient design approach is its capability to compensate for energy decay in the energy feeding waveguide. To highlight this point, we compare our results with the state-of-the-art literature in device apertures in Table 4-1. Here, we only consider devices that transform a guided wave into a plane wave, and exclude other forms of off-chip plane wave generation (e.g., generating a plane wave from a surface wave [174]). In the table, we distinguish the nominal width, which is the geometric dimension of a metasurface, from the effective width, which is the size of the beam width of the emitted light. For our 1000-unit meta-waveguide, the geometric length is $400\lambda_0$, while the beam width, calculated from the beam FWHM at a height of $6\lambda_0$ [i.e., along the top edge of Figure 4.3.(b)], is $275\lambda_0$. Although the shadowing effect still exists here, our device brings an order of magnitude increase in device aperture as compared to state-of-the-art literature (Table 4-1). The comparison clearly shows that amplitude gradient metasurfaces are ideal for plane wave generation. As a beam expander, the 1000-unit device increases the beam by a factor above 900 when we take the waveguide width (i.e., $112\ \mu m$) as the width of the input wave. It is worth pointing out that the simulation of the 1000-unit device is close to the limit of our computing power, and we believe that the beam expansion factor can be further increased in the future (e.g., by using larger values of g that

change at a smaller step). It is worth noting that, as we were already approaching the limit of the computing power of the University's supercomputer, we could only simulate a single, long waveguide. We foresee that, if an array of these waveguides is placed at a subwavelength interval and the waveguide-waveguide near-field coupling is minimal, a true plane wave can be generated from it.

Table 4-1 Comparison with state-of-the-art literature on meta-waveguide-based plane wave generation. For the beam width, a nominal value refers to the dimension of the metasurface, while an effective value refers to that of the output light.

Ref.	Design approach	Wavelength (λ_0)	Beam width (Nominal or Effective)
[110]	Phase gradient	$1550\ nm$	$8\ \lambda_0$ (Nominal)
[146]	Phase gradient	$720\ nm$	$10\ \lambda_0$ (Effective)
[163]	Phase gradient	$300\ \mu m$	$5\ \lambda_0$ (Nominal)
This work	Amplitude gradient	$375\ \mu m$	$400\ \lambda_0$ (Nominal) $275\ \lambda_0$ (Effective)

4.3 Light focusing lens as the second functional device

Different wavefront shaping functionalities can be obtained simply by bending the straight waveguide shown above into a circle. I explore in this section the focusing function, where the meta-atoms extract the guided light off the chip into a focus and discuss in detail the orbital angular momentum of the extracted light in the next section. In both sections, as the circle is much larger than individual meta-atoms, the curvature of the central waveguide is ignored in the element selection illustrated in Figure. 4.5.

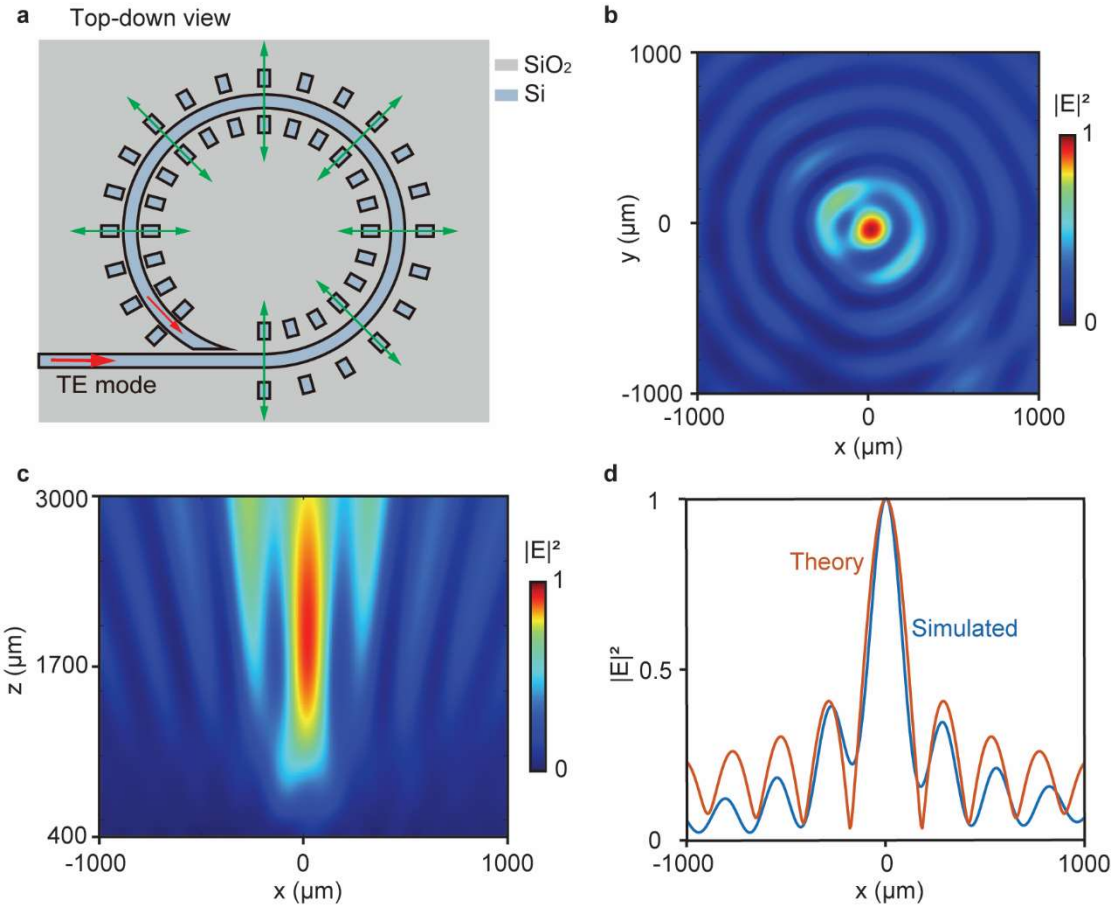

Figure 4.4 Off-chip light focusing by an amplitude-gradient metasurface. (a) Schematic of the device. The waveguide is bent into a circle, and it is decorated uniformly with 100 meta-atoms except for the final $1/12$ of the circle. The fundamental TE mode is launched into the waveguide in the $+x$ direction, and each meta-atom functions like an electric dipole radiating in the radial direction. (b) The electric field distribution at a xy plane above the centre of the device. The plane passes through the centre of the central focal spot, which is approximately $2\ mm$ above the device. (c) The electric field distribution at the xz plane that passes through the centre of the device. The bottom edge of the map is $400\ \mu m$ above the middle plane of the device. (d) The simulated field amplitude along the line of $y = 0$ in panel (b), overlaid with the analytical results derived from a zeroth-order Bessel function of the first kind.

Figure 4.4 shows a light-focusing circular meta-waveguide, which can also be referred to as a waveguide-driven metalens. The waveguide is bent in the anti-clockwise direction [Figure 4.4.(a)] at an outer radius of $2650\ \mu m$. Before tapering off at its tail, the waveguide maintains the same cross-sectional dimensions as those in the previous section (i.e., $70\ \mu m$ in height and $112\ \mu m$ in width). However, the values of w_x and w_y are swapped to be $65\ \mu m$ and $100\ \mu m$, respectively. The reason for this is that bending the straight waveguide will reduce the distance between the adjacent nanopillars located by the inner side of the waveguide. This will increase the crosstalk between two adjacent nanopillars. Figure 4.5 illustrates the output of these meta-atoms. It also

has an exponentially decreasing power when increasing the gap g and a nearly flat phase response. One hundred meta-atoms distribute uniformly along the first $11/12$ segment of the circle, and the angle θ between adjacent meta-atoms is 0.05782 rad. The residual power reaching the end of the waveguide is 10.7% of the total input, while the reflection from the tail that remains inside the waveguide is at the order of 10^{-4}.

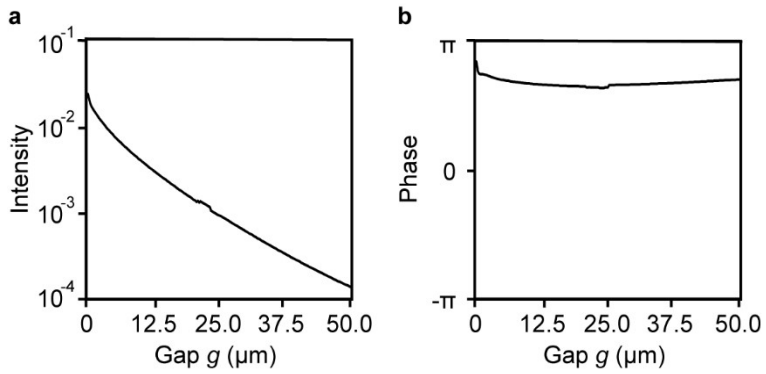

Figure 4.5 The output of individual meta-atoms, with w_x fixed at $65\ \mu m$ and w_y fixed at $100\ \mu m$. (a) The power decreases nearly exponentially with increasing the gap g, meanwhile (b) the phase is nearly flat in the same range of g.

Similar to the devices discussed in the previous section, here the gap g is adjusted along the waveguide. Its value decreases at a step of $0.1\ \mu m$ towards the waveguide tail, and its smallest value is $5\ \mu m$. This distribution creates a gradient in the scattering efficiency in the meta-atoms that compensates for the decay in the residual power along the waveguide. The collective response of the meta-atoms creates a circular light source that has an almost uniform intensity distribution along its circumference. This light source approximates an annular aperture, where a ring-shaped opening is cut in an opaque mask. Nevertheless, different from the most standard textbook configuration [175], where an annular aperture is illuminated by a linearly polarised plane wave, here each meta-atom approximates an electric dipole that oscillates in the radial direction [Figure 4.4.(a)]. The output field of this radiation configuration can also be explained as the vector vortex beam described in Section 2.1.4. It leads to the generation of a Bessel beam, which has been investigated previously in the research field of microring-based vortex beam generators [4].

Figure 4.4.(b) and 4.4.(c) show the output field in a segment of the xy and xz planes above this waveguide-driven metalens. An elongated central focus and a series of concentric rings surrounding it are observed, which are key features of a Bessel-beam focus. The field distribution is not perfectly circular in the xy plane [Figure 4.4.(b)], which is attributed to factors such as a fluctuation of output intensity along the waveguide, the lack of light scatterers at the end $1/12$ segment of the circle, and light scattering at the waveguide tail. The last factor originates from the tapering of the waveguide. A gradual shrink in the waveguide width at its tail reduces light

reflection inside the circular waveguide, but it radiates light into free space and can disturb the field distribution at the focus.

To further confirm that the focus is a Bessel beam [176, 177], Figure 4.4.(d) compares the simulated result with a zeroth-order Bessel function of the first kind. A good fitting is observed, especially for the central focal spot. This fitting gives a FWHM of the central focus of $221.2\ \mu m$, which is approximately $0.59\lambda_0$. The output efficiency, taking into account both the central focus and the concentric rings, is 27%.

It is worth mentioning that this focus is a beam with $l = 1$, as explained in Section 2.1.4. From Figure 4.6, we can see that the radial electric field of the metalens has one optical cycle around the device axis.

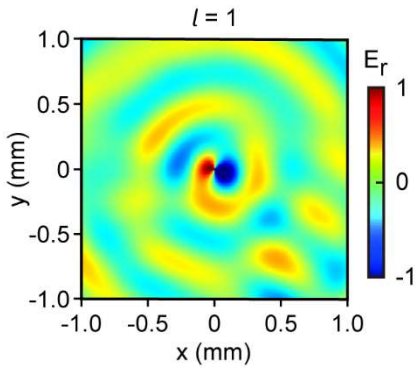

Figure 4.6 The radial electric field of the metalens discussed in Figure 4.4. The map shows a $2\ mm \times 2\ mm$ square approximately $2\ mm$ above the emitter.

4.4 Vortex beam generator as the third functional device

The meta-waveguide layout shown in Figure 4.4.(a), where many light scatterers distribute uniformly along the circumference of a circle, is in fact an ideal configuration for generating optical vortex beams. A vortex beam can carry orbital angular momentum (OAM), which can be utilised for high-resolution imaging [178], laser micromachining [179], particle manipulation [180], as well as optical communication in both the classical and quantum regimes [8, 181]. An analysis of the phase distribution of the output shown in Figure 4.6 indeed reveals a finite value of orbital angular momentum. It is worth noting that, for such radially polarised cylindrical vector vortex beams [47], a focus without an intensity minimum at its centre can carry a finite value of orbital angular momentum [34]. There have been many reports on off-chip vortex beam generation using a waveguide, and they utilise either a phase gradient metasurface or a decorated microring resonator [182-184]. Figure 4.7 shows that a third approach to off-chip emission exists, which is to use an amplitude gradient metasurface.

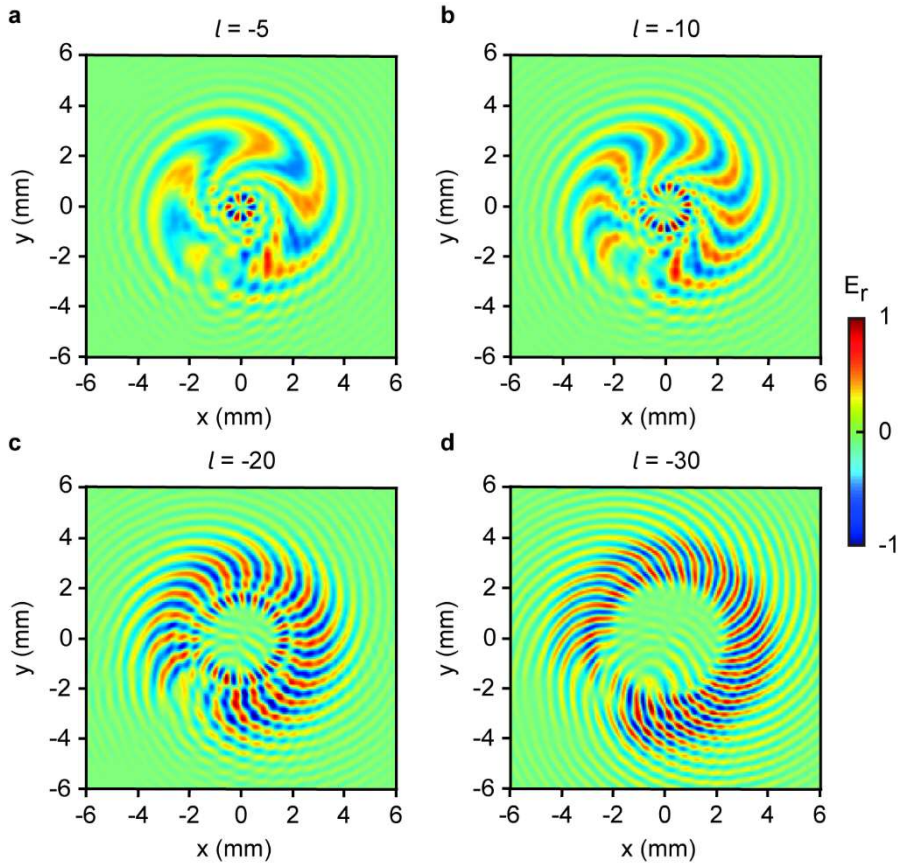

Figure 4.7 Off-chip vortex beam emission from four meta-devices. All the devices have the same circular waveguide but a different number of meta-atoms, which is (a) 105, (b) 110, (c) 119, and (d) 128. For each device, the radial electric field E_r of the same area is shown here, which is a square of $12\ mm\ \times\ 12\ mm$ at approximately $2\ mm$ above the emitter. The field is normalised against the maximal value of respective figures. The topological charge, which corresponds to the number of optical cycles around the beam axis, is (a) -5, (b) -10, (c) -20, and (d) -30.

To understand vortex beam generation using the device layout of Figure 4.4.(a), we can refer to the vortex beam generation in a decorated microring resonator. In a decorated microring resonator, an OAM carrying vortex beam originates from the phase mismatch between adjacent nanostructures (e.g., shallow holes in Ref. [4]) in their light scattering. The value of the topological charge l is consequently derived to be the difference between the number of nanostructures and the resonance order of the whispering gallery mode [4]. Here, I also concentrate on the phase mismatch between adjacent meta-atoms, even though the meta-waveguide does not form a full circle and there is no whispering gallery mode. I consequently can arrive at this expression for the topological charge of l,

$$l = 2\pi\left(\frac{r}{\lambda_{neff}} - \frac{1}{\theta}\right) \tag{4.2}$$

where r is the radius of the circle and θ is the angle between two adjacent meta-atoms. Note that this equation is valid for a meta-waveguide that occupies only a part of a full circle, a configuration that is shared by all four devices in Figure 4.7.

Figure 4.7 shows the vortex beams generated by four different devices. Most of the geometric structure of this generator is similar to the metalens in the last section. The differences between these two devices are the smallest gap g and the number of meta-atoms along the first $11/12$ segment of the circle waveguide. The gap g still decreases at a step of $0.1\ \mu m$ in the forward direction, but its smallest value is now $3\ \mu m$. The number of meta-atoms differs among the four devices, which is 105, 110, 119, and 128 in Figure 4.7.(a-d), respectively. This leads to a variation in the angle θ, which is 0.05480 rad, 0.05251 rad, 0.04846 rad, and 0.04499 rad in the four panels.

The topological charge l takes the values of -5 [Figure 4.7.(a)], -10 [Figure 4.7.(b)], -20 [Figure 4.7.(c)], and -30 [Figure 4.7.(d)], which correspond to the number of optical cycles around the device axis in each map. This adjustment in the number of meta-atoms changes the value of θ. By taking the same λ_{neff} value of 2.523 for all the devices, the value l derived from Eq. (4.2) is -5.0, -10.0, -20.0, and -30.0 for Figure 4.7.(a-d), respectively, identical to the simulated results. All four panels of Figure 4.7 show the same area at the same height above the devices. It is clear that, as the absolute value of l increases from Figure 4.7.(a) to Figure 4.7.(d), the radiation becomes more divergent. The output efficiency extracted from Figure 4.7 is 29%, 31%, 31%, and 32% for Figure 4.7.(a-d), respectively.

As two different types of planar vortex beam emitters, the meta-waveguide discussed in this section and the decorated micro-ring resonators [4] have a certain degree of similarity in their device layout. It is thus worth highlighting some of their key differences here. Firstly, the meta-waveguide does not require any whispering gallery mode resonance, which removes a lot of design constraints (e.g., the bus waveguide-ring coupling and the resonance wavelength) and simplifies the design process. Secondly, the meta-waveguide is more suitable for applications that require a large emission aperture, thanks to its amplitude gradient design approach (the simulation of the 100-unit devices in Figure 4.7 is approaching the limit of our simulation capability, but we foresee that larger devices can also be functional). Thirdly, unlike the decorated micro-ring resonators, Eq. (4.2) does not force l to be an integer here. Consequently, the meta-waveguide could be utilised as a platform to study the generation of vortex beams that carry a non-integer topological charge [185].

4.5 Conclusion

To conclude, I have proposed and numerically tested a new metasurface design approach for extracting a guided THz wave into free space and shaping its wavefront. The design utilises meta-atoms with a gradient in their light scattering amplitude, which is achieved by adjusting the size of the gap between the central waveguide and its side pillars. This new amplitude gradient design approach is very different from the widely adopted phase gradient design approach. As this approach can compensate for the energy decay in the energy-feeding-guided mode, a large number of meta-atoms can be accommodated along a single waveguide, as demonstrated in our 100- and 1000-unit devices. Three different off-chip wavefront shaping functionalities are consequently demonstrated: (1) the generation of a plane wave, where the beam width can reach $275\lambda_0$, equivalently a factor above 900 in width expansion; (2) the generation of a Bessel-beam focus with a FWHM of $0.59\lambda_0$; (3) the generation of OAM-carrying vortex beams, where the topological charge is tuned from -5 to -30.

The amplitude gradient design concept shown here is generic and can be applied in other regimes, such as microwave and infrared bands, as long as the required tuning in the gap size is within the reach of standard nanofabrication technologies. In future experiments, accurately controlling the gap sizes will be critical, and a potential challenge here is the nanofabrication of devices with a high aspect ratio [186, 187]. The device performances can also be affected by factors such as material absorption and surface roughness, which can accelerate the decay of the guided wave and limit the device aperture. Analysis of these factors is beyond the scope of this proof-of-principle demonstration.

The three light shaping functionalities demonstrated here could be used in a range of different applications, such as THz imaging [188], molecular sensing [189], and 6G communications [190]. All the meta-devices demonstrated here have a relatively straightforward configuration of the meta-atoms (all identical and evenly distributed) and the waveguide-pillar gap (changing at a constant step along the waveguide). More complicated configurations (e.g., obtained by incorporating methods such as the inverse design method [130]) could lead to other types of wavefront shaping and functionalities.

Chapter 5 Experimental works

After completing the simulations discussed in the last two chapters, I have focused on related experimental works. This involves fabricating devices and conducting measurements in the laboratory. Three different types of devices are demonstrated in this chapter, which include integrated vortex beam emitters, monolithic fabrication of grating couplers and ring resonators, and metasurfaces for vortex beam generation.

5.1 Integrated vortex beam emitter

The first part of my experimental work was to fabricate a conventional integrated vortex beam generator. This device was designed for testing experimental setups that will be built to measure the metasurface-decorated microring emitter discussed in Chapter 3.

5.1.1 Design of the emitter

The device consists of an access waveguide and a ring-shaped silicon waveguide positioned on top of a silica substrate, as illustrated in Figure 5.1. To simplify the fabrication process and enhance the coupling efficiency, the Si slab has a thickness of $100\text{-}nm$ across the entire substrate. Both the access and the ring waveguide have dimensions of $500\,nm$ in width and $220\,nm$ in height. A 60-nm gap separates the access waveguide from the ring waveguide. After etching uniformly distributed cavities along the centre circle within the ring waveguide, a vortex beam is expected to be generated at specific resonance wavelengths. These apertures have a diameter of $70\,nm$ and a depth of $70\,nm$. The key structure parameters of the device are summarized in Table 5-1.

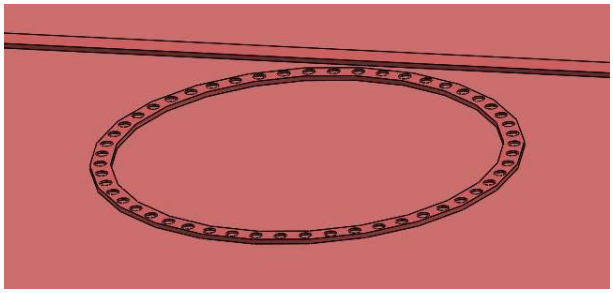

Figure 5.1 Schematic view of an integrated vortex beam emitter. It contains a strip waveguide, a ring-shaped waveguide, and cavities.

Table 5-1 Parameters of the conventional vortex beam emitter

Parameters	Value	Parameters	Value
Rib waveguide width	$500\ nm$	Quantity of cavities	52
Rib waveguide height	$220\ nm$	Cavities depth	$70\ nm$
Rib waveguide slab thickness	$100\ nm$	Cavity diameter	$70\ nm$
Radius of the ring resonator	$10\ \mu m$	Gap	$60\ nm$

The method employed to couple light into the waveguide is grating couplers. A grating coupler is a device used for coupling light between a waveguide on a chip and free-space. It consists of periodic structures that create a diffraction grating, efficiently redirecting light between the waveguide and external optical components. Positioned between the grating coupler and microring resonator is a taper, which gradually adjusts the dimensions of the waveguide from the grating coupler to match those of the microring resonator. The length of the taper is carefully chosen to ensure efficient transfer of light from the wide mode of the grating coupler to the narrower mode of the microring resonator while also avoiding unnecessary loss of the mode. Figure 5.2.(a) provides a schematic view of the structure containing a grating coupler, a taper, and a ring resonator.

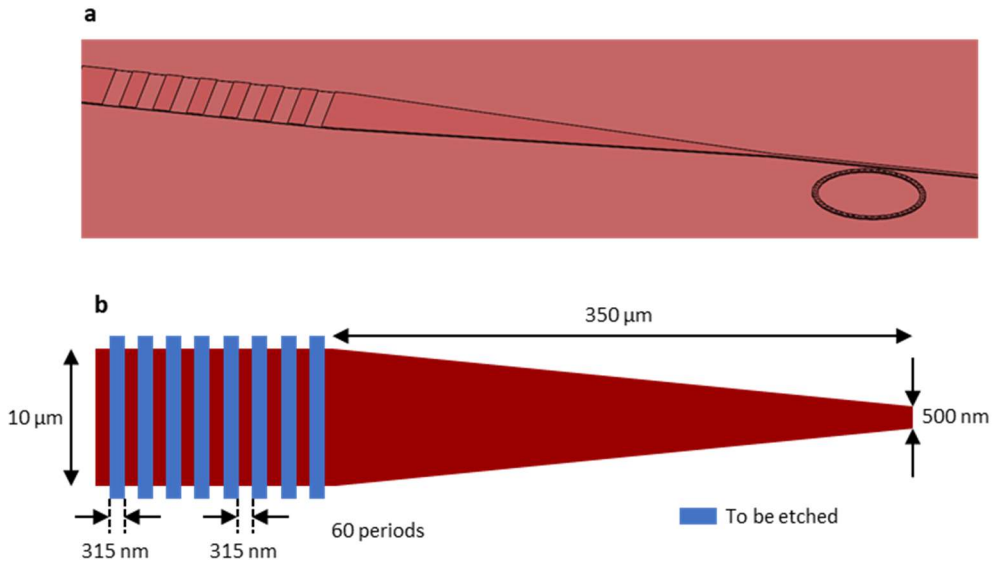

Figure 5.2 Grating coupler and taper. (a) The 3D illustration of a grating coupler and a ring resonator. Grating couplers are symmetrically located at both ports of the access waveguide, one for input light and the other for monitoring light transmission. (b) A

zoomed-in view of the grating coupler and the taper (dimensions not to scale). The structural parameters are taken from Ref. [191].

5.1.2 Fabrication of the device

The fabrication process took place at the Southampton Nanofabrication Centre, and the device was fabricated on a $3\,cm \times 4\,cm$ chip. Figure 5.3 illustrates the fabrication process of the device.

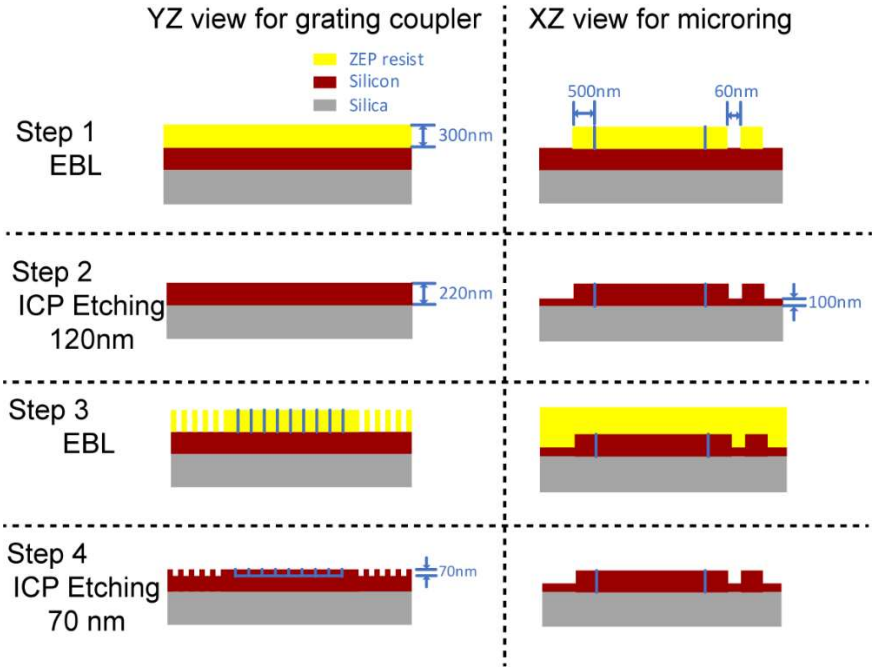

Figure 5.3 Fabrication process of vortex beam generators.

Before starting the fabrication process, the SOI chip was prepared, which included dicing a wafer, cleaning the chip, and coating the chip with a layer of ZEP resist (approximately 300 nm in thickness). Step 1 was using electron-beam lithography (EBL) to pattern the waveguide structure. In Step 2, inductively coupled plasma (ICP) etching was utilised to etch $120\,nm$ of the silicon layer by using SF_6 and C_4H_8 as precursors. After cleaning the resist, step 3 was using EBL to define the grating pattern and cavities. After this step, ICP etching was used again to etch the grating and cavities to a depth of $70\,nm$.

Figure 5.4 depicts the scanning electron microscopy (SEM) images of the first fabricated device. The fabrication results reveal several defects: Firstly, as the cavities and the ring resonator were not written in a single EBL process, misalignments are obvious. Secondly, the gap between the access waveguide and the microring waveguide was not etched down as designed. Thirdly, the duty cycle of the grating coupler does not meet the desired 50%, measuring only 40.6%.

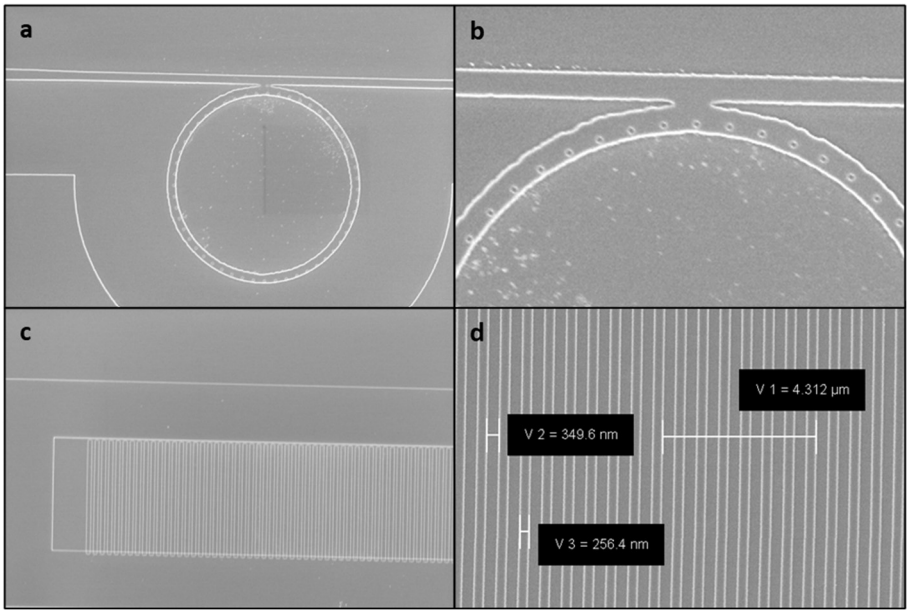

Figure 5.4 SEM figures of the fabricated device. (a) Top-down view of the whole microring resonator. (b) The zoom-in figure indicates the misalignment and unetched gap. (c) Top-down view of the grating coupler. (d) Measurement of the widths of both etched and unetched features.

To address these issues, three correction methods were applied. Firstly, considering the importance of cavity-microring alignment, both cavities and waveguide structures were designed on the same mask layer of EBL. However, a difference shows up between the ideal depths of the cavities ($70\ nm$) and the slab ($120nm$). I think this issue can be solved by using the microloading effect. It is a phenomenon in which less etchant is transported to the bottom of narrow gaps, causing the etching rate to decrease depending on pattern width. Given that the ZEP film has a depth of $300\ nm$ while the cavities have a diameter of only $100\ nm$, the etch rate of the cavities could be slower than that of the slab.

The second correction method is reducing the thickness of the ZEP film. Thicker resist films can lead to various issues, such as development difficulties, challenges in EBL writing, and etching defects. Hence, it is practical to minimise the thickness of the resist film while still ensuring adequate protection for features. Given that the etch method was plasma etching, it involved physical etching during the process. Thus, I have experimentally tested the selectivity of our silicon etching recepies. The results indicate an etching selectivity of around 3:1 between silicon and ZEP film. This means that under the same conditions, the etching rate of Si is three times faster than that of the ZEP film. Consequently, it was determined that a 180 nm ZEP film would provide sufficient protection for the structures during the $120\ nm$ silicon etching process.

The third measure is adjusting the duty cycle of the grating coupler in the EBL mask to achieve the desired 50%. Plasma etching is known for its isotropic etching characteristics, meaning that

the etchant attacks the material in all directions rather than solely perpendicular to the surface. Thus, during the etching process, undercut sidewalls are formed. It means that the edge areas protected by resist is etched. To solve this issue, the duty cycle in the mask was reduced to 40%.

Figure 5.5 illustrates the improvements achieved after three optimisations in the fabrication process. The misalignment issue between the cavities and microring is resolved. A $60\ nm$ gap appeared as intended and the duty cycle of the grating coupler is around 50%.

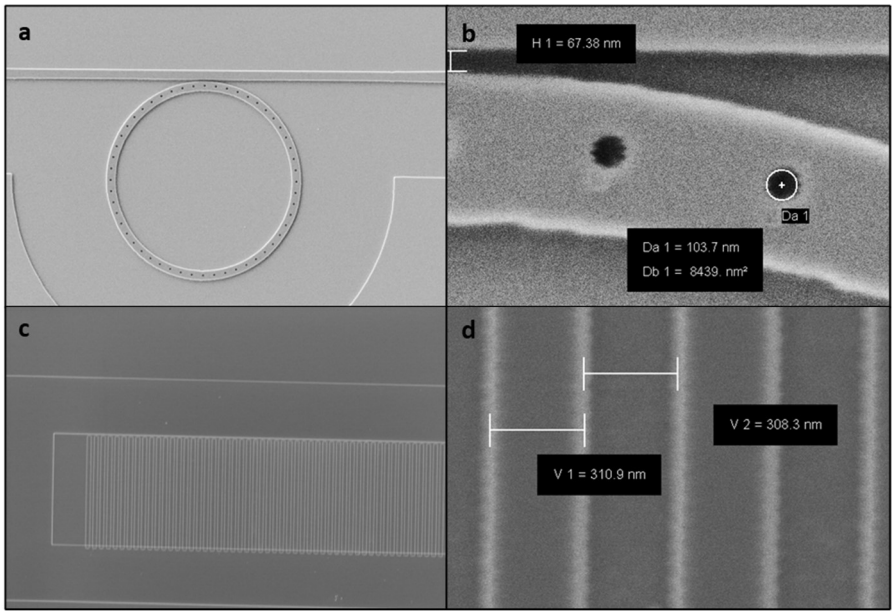

Figure 5.5 SEM figures of the fabricated device after optimisation. (a) Top-down view of the microring resonator. (b) A zoom-in figure to the area of the gap and cavities. (c) Top-down view of the grating coupler. (d) Measurement of the widths of both etched and unetched features.

5.2 Monolithic fabrication of microring resonator

In the previous section, I used two separate EBL steps for writing the waveguide structure and grating coupler due to the requirement for different etching depths. However, to simplify the fabrication process and save time and fabrication costs, I decided to use monolithic fabrication to produce a microring resonator. This work is a cooperation with Siyu Chen, who primarily focused on device measurement while I focused on device fabrication.

I simplified the lithography process to a single step, which implied a single etch depth. Because of the presence of the slab, a rib waveguide can never be a single-mode waveguide. However, by reducing the thickness of the slab, higher-order modes can leak out over a short distance, leaving only the fundamental mode in the waveguide. Consequently, for monolithic fabrication, we increased the depth of the grating from $70\ nm$ to $150\ nm$.

To facilitate easier light coupling, we enlarged the grating area of the grating coupler by 2.5 times compared to the design in Section 5.1, as illustrated in Figure 5.2.(b). A similar modification was applied to the taper section to enable high-efficiency single-mode transformation. This modification aims to simplify the measurement process. Given that the input fibre in our lab, a single-mode fibre with a core diameter of 9 μm, requires precise alignment with the center of the original grating coupler design, the enlargement of the grating coupler helps ease this requirement. By increasing the size of the grating coupler, not only does it help to find the maximum transmission when adjusting the fibre position, but it also allows for raising the fibre, offering additional protection to the fibre. The fabrication process follows a similar procedure to the previous integrated vortex beam emitter, while only utilising one EBL step and ICP etching to a depth of 150 nm. The fabricated microring resonator and grating coupler are shown in Figure 5.6. As observed, the device has smooth edges, and the duty cycle of the grating coupler is approximately 48.4%.

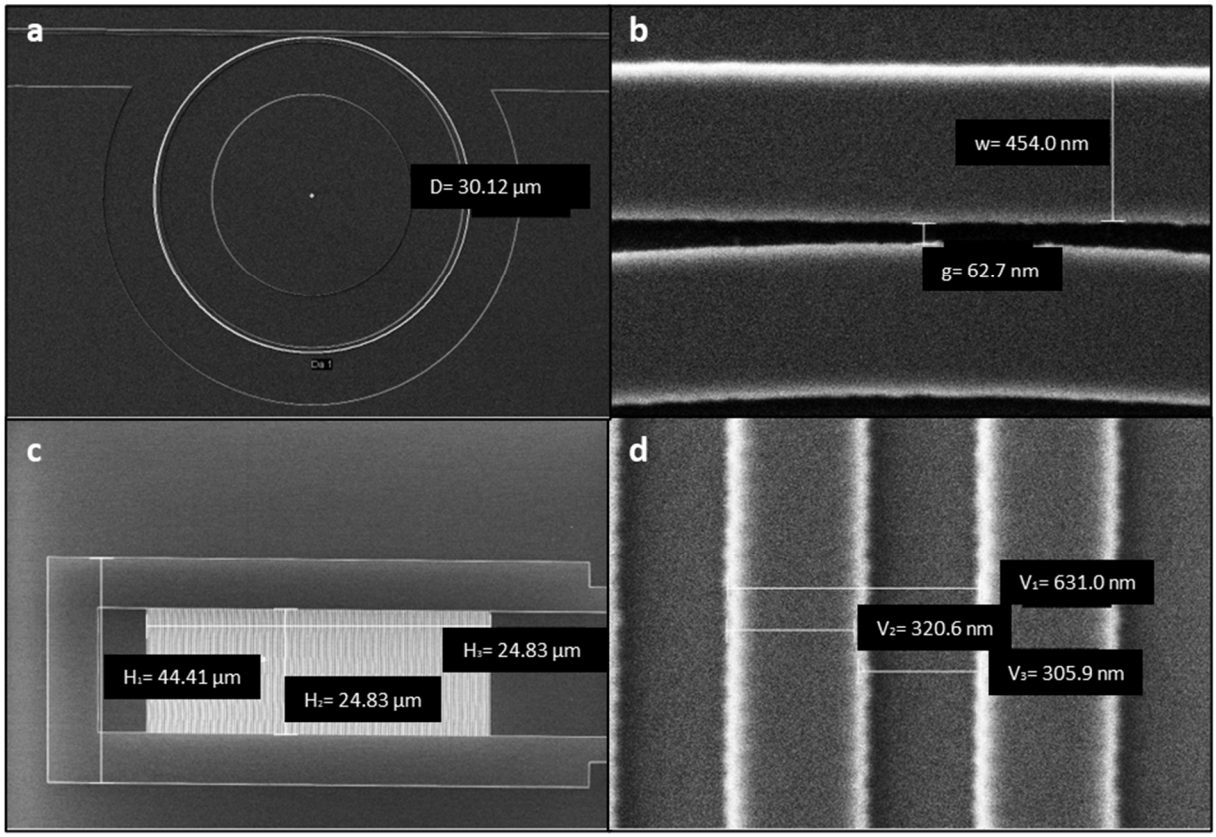

Figure 5.6 SEM figures of the fabricated device. (a) Top-down view of the microring resonator. (b) A zoom-in figure of the area of the gap. (c) Top-down view of the grating coupler (d) Measurement of the widths of the etched and unetched features.

5.3 Metasurfaces for vortex beam emission

In this section, I discuss a metasurface for vortex beam generation. The design has been optimised using the software Lumerical. Several devices have been fabricated, and they will be used to test our measurement system in the future.

5.3.1 Design schematic of the emitter

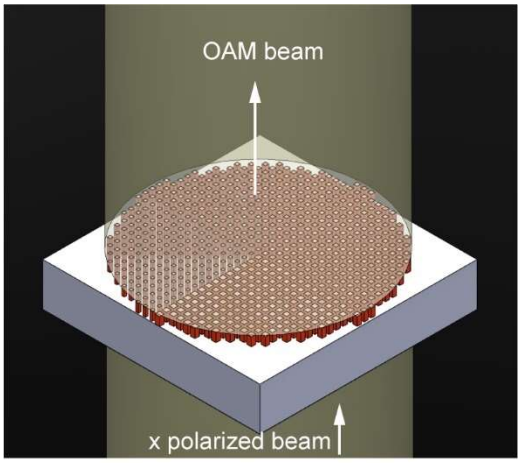

Figure 5.7 Schematic view of the metasurface device. The device contains two layers of material, Si and SiO_2. The Si metasurface has a height of $800\ nm$, and it is on top of a SiO_2 substrate. When a linearly polarised light beam luminates the metasurface, the transmitted light carries a finite value of OAM.

Figure 5.7 schematically illustrates the metasurface design. This device contains amorphous silicon (a-Si) meta-atoms positioned on top of a 2-inch quartz wafer. Each meta-atom has a square cross section with a width of w perpendicular to the propagation direction. In the simulation, the reflective indexes of a-Si and SiO_2 are set as 3.476 and 1.444, respectively [132]. Both materials are treated as lossless in the simulation. The input light wavelength is $1550\ nm$. This design uses the FP resonance approach to achieve a 2π phase coverage.

5.3.2 Properties of the meta-atoms

Figure 5.8.(a) presents the schematic view of a single meta-atom, which consists of a segment of quartz substrate and a nanopillar. All the nanopillars have a square cross section and a height of $800\ nm$. To manipulate the emitted phase of meta-atoms, the width of the square w is tuned from $100\ nm$ to $600\ nm$ in steps of $5\ nm$, resulting in 101 meta-atoms for selection. For each meta-atom, periodic boundary conditions are applied in the x and y directions with a period of $650\ nm$. The input light is a plane wave that is x-polarised. Figure 5.8.(b) shows the simulated electromagnetic properties of the meta-atoms. The phase and efficiency curves exhibit two main

features: (1) A 2π phase coverage can be achieved when w ranges from $100\ nm$ to $400\ nm$, with transmission exceeding 95% for all selections. (2) There is a large drop in transmission at around $w = 440\ nm$, accompanied by a steep phase change.

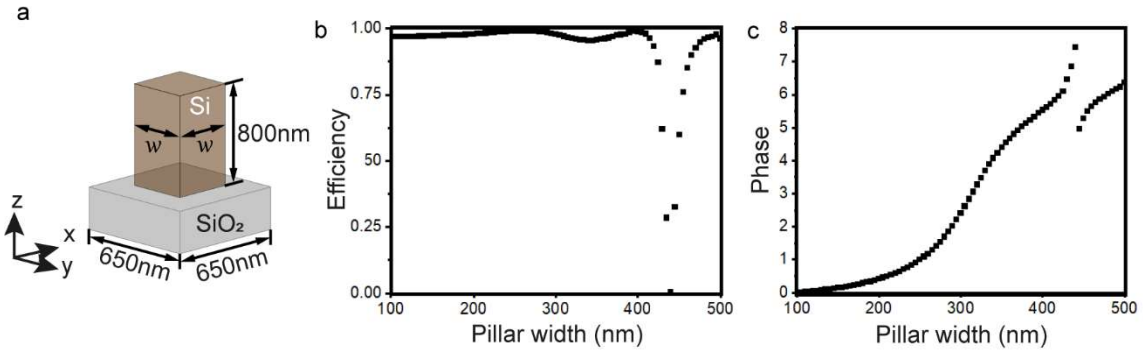

Figure 5.8 Optical properties of individual meta-atoms. (a) Schematic view of a meta-atom. (b) Emission efficiency of meta-atoms. (c) Emitted phase of meta-atoms.

Based on the optical properties described above, 8 meta-atoms are selected for the device. They are listed in Table 5-2.

Table 5-2 Properties of all eight meta-atoms in a super unit cell at the wavelength of $1550\ nm$. The widths of pillars vary between $100\ nm$ to $400\ nm$.

Number of pillars	#1	#2	#3	#4	#5	#6	#7	#8
$w\ (nm)$	100	235	275	300	320	335	360	400
Emission phase (rad)	0	0.764	1.535	2.404	3.269	3.884	4.675	5.527
Emission Efficiency	98.0%	987	99.0%	97.8%	96.3%	95.6%	96.1%	98.8%

5.3.3 Output properties of the device

To simplify the simulation, the effective area has a fixed radius of $10\ \mu m$. Eleven devices are designed to cover various OAM states ranging from -5 to 5. Figure 5.9 compares four different devices that generate different OAM states.

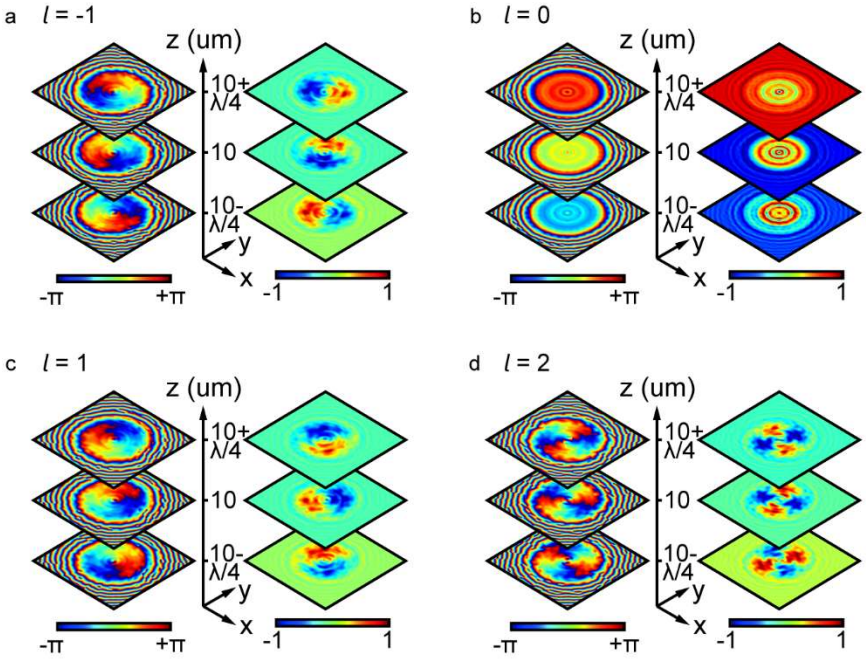

Figure 5.9 The x component of the transmitted electric field. The devices generate a topological charge of (a) $l = -1$, (b) $l = 0$, (c) $l = 1$, and (d) $l = 2$. For each OAM state, the left and right columns illustrate the phase and amplitude of the electric field, respectively. Each map has dimensions of $20\ \mu m \times 20\ \mu m$ and is obtained around $10\ \mu m$ above the surface of the quartz substrate. The propagation distance between two adjacent maps in one column is $\lambda/4$. The amplitude of each map is normalised against the maximum value of the corresponding maps.

Compared to the non-vortex beam $(l = 0)$, the vortex beam has a twisted phase and amplitude. The value of topological charge is related to the number of twists in the field. It can be obtained by two methods. The first method is to count the optical cycles in the transverse field. Along the circle centred on the beam axis, the sign of l indicates the increasing direction of the phase (either clockwise or counterclockwise), while the absolute value tells the number of cycles of the phase and amplitude. The second method is to trace the emitted field along the propagation direction. For a distance λ, the field rotates by $2\pi/|l|$, and the sign of l determines the direction of rotation of the phase.

5.3.4 Fabrication process of the device

The device fabrication was conducted at the Southampton Nanofabrication Centre. It was fabricated on a 2-inch quartz wafer. The fabrication process of the metasurfaces is plotted in Figure 5.10 and outlined as follows:

Step 1 is the preparation of the quartz wafer. Step 2 is the deposition of 800-nm amorphous Si using plasma-enhanced chemical vapour deposition (PECVD). Plasma gases of SiH_4 and Ar are

used, and the temperature of the reaction chamber is 350℃. Step 3 involves resist coating, EBL, and resist development. This step is for patterning metasurface features on top of the a-Si layer. A 300-nm-thick layer of ZEP520A (positive resist) is used. After EBL, the exposed area becomes soluble in the resist developer (step 4). In step 5, a thin layer of Cr is deposited on the ZEP resist by sputtering. A 35-nm-thick Cr layer is used for pattern transfer. This helps to define the pattern and reduce the writing time of the EBL process. In step 6, the wafer is soaked in 1-methyl-2-pyrrolidone (NMP) solvent to clean the ZEP and the unwanted Cr. In step 7, the a-Si film is etched down with plasma gases (CHF_3 and O_2) by reactive ion etching (RIE). Step 8 is wet etching for cleaning the Cr hard mask.

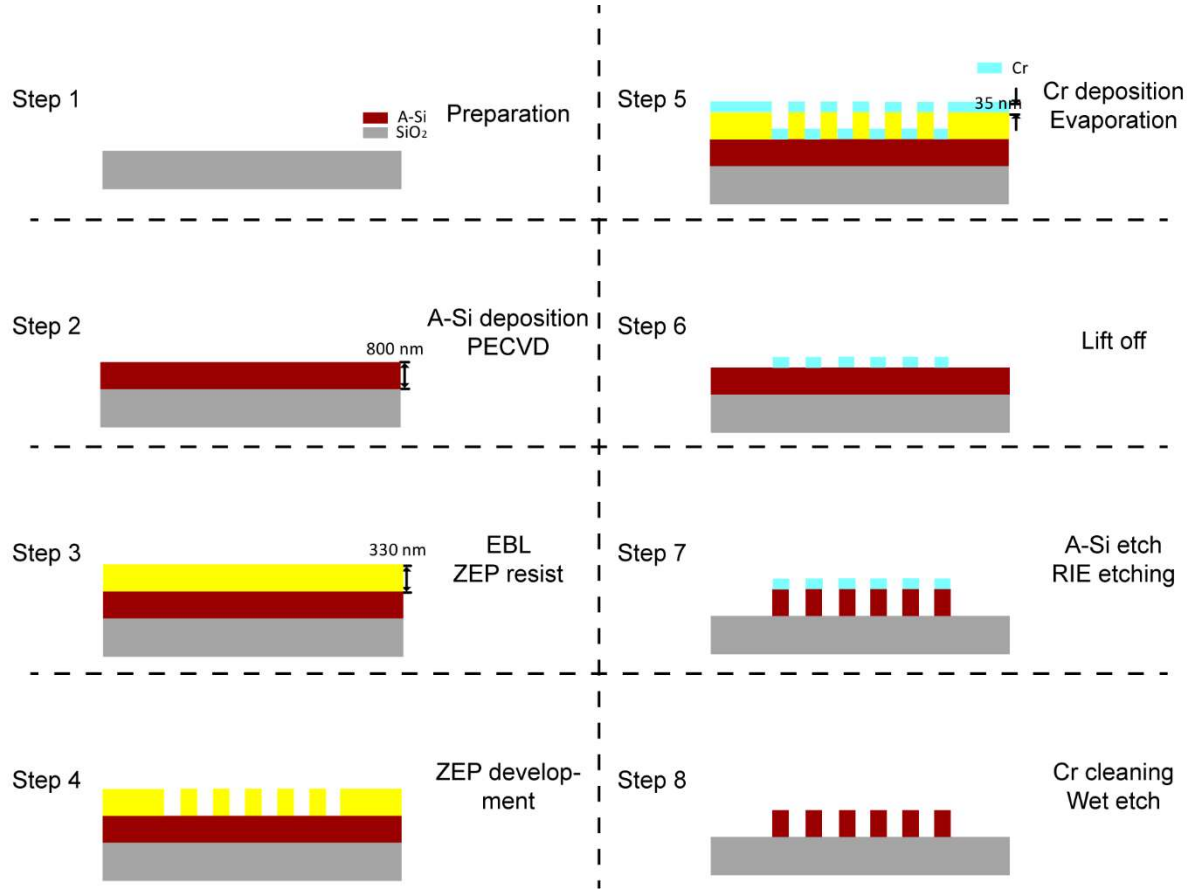

Figure 5.10 Fabrication process of transmissive metasurface.

Figure 5.11 shows SEM images of the fabricated devices. Figures 5.11.(a-e) shows different devices capable of generating the vortex beams with topological charges from 1 to 5. By tracing the number of cycles in the width-increasing pillar, we can derive the generated topological charges of the devices. However, it is observed that the smallest pillars ($w = 100$) are destroyed in the nanofabrication. The origin of this issue can be found in Figure 5.11.(f), where the sidewall of the pillars is not perfectly vertical. This is a feature of isotopic etching.

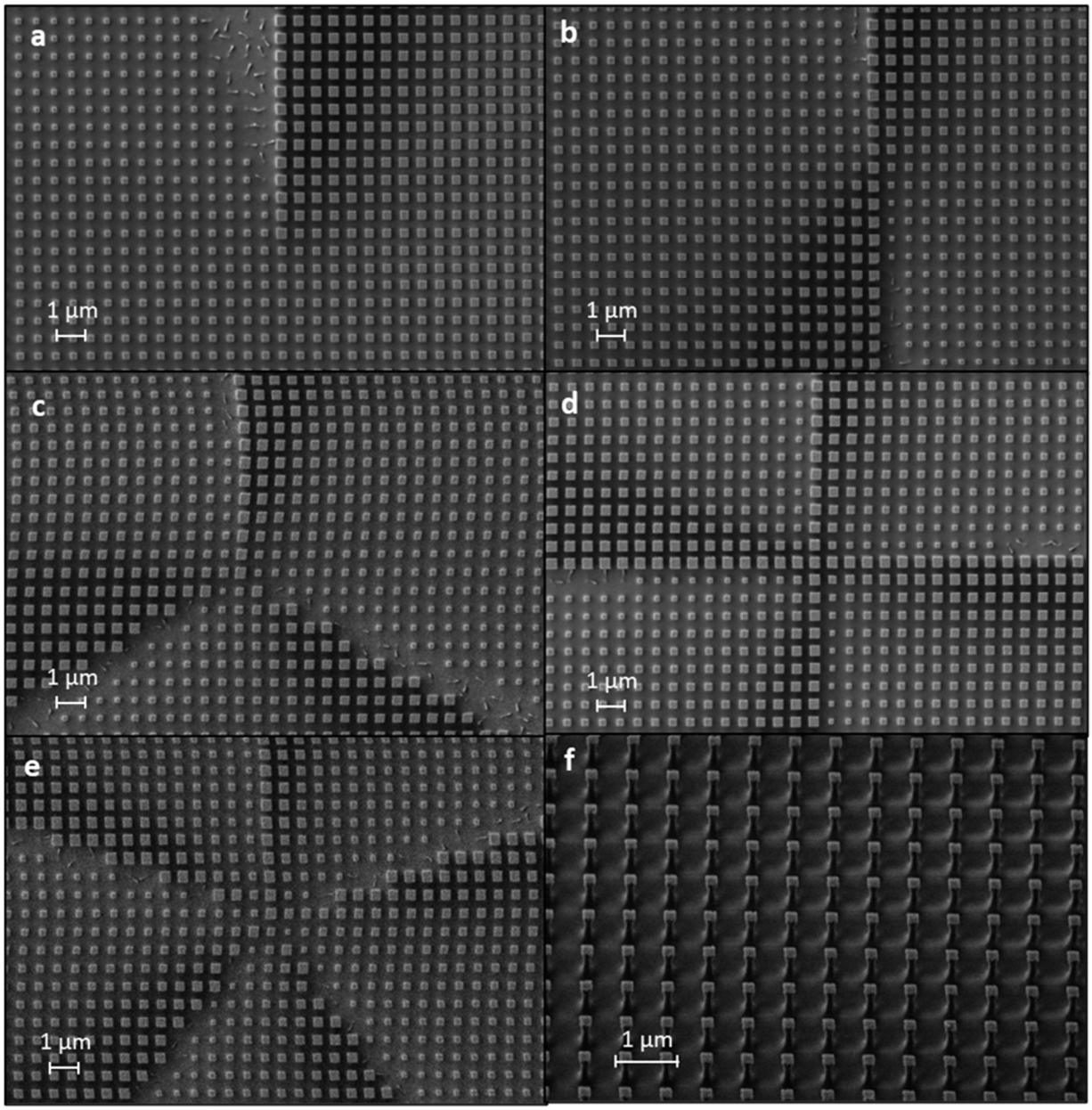

Figure 5.11 SEM images of a batch of fabricated devices. The widths of pillars vary between $100\,nm$ and $400\,nm$. The topological charge of devices in (a-e) is from 1 to 5, respectively. (f) Provides a closed-up view of the sidewall of the second-smallest pillar in an array. The image is tilted with 30-degree for better observation.

To improve device quality, a new super unit cell was designed to ensure the smallest pillar remained in a vertical standing position after the fabrication. The smallest pillar ($w = 100$) of the previous design was replaced by a pillar with a width value of $420\,nm$. This new selection still achieved a 2π phase coverage with transmission exceeding 93% for all pillars.

Table 5-3 Properties of all eight meta-atoms in a modified super unit cell at $1550\,nm$ wavelength. The widths of pillars vary between $235\,nm$ and $420\,nm$.

Number of pillars	#1	#2	#3	#4	#5	#6	#7	#8
$w\ (nm)$	235	275	300	320	335	360	400	420
Emission phase (rad)	0.764	1.535	2.404	3.269	3.884	4.675	5.527	5.952
Efficiency	98.7%	99.0%	97.8%	96.3%	95.6%	96.1%	98.8%	93.3%

Figure 5.12 shows SEM images of the fabricated devices with the new super unit cell. The devices are designed to have five distinct topological charges of -3, -2, -1, 1, and 2. As observed in Figure 5.12, all the pillars remain vertical after all the nanofabrication steps.

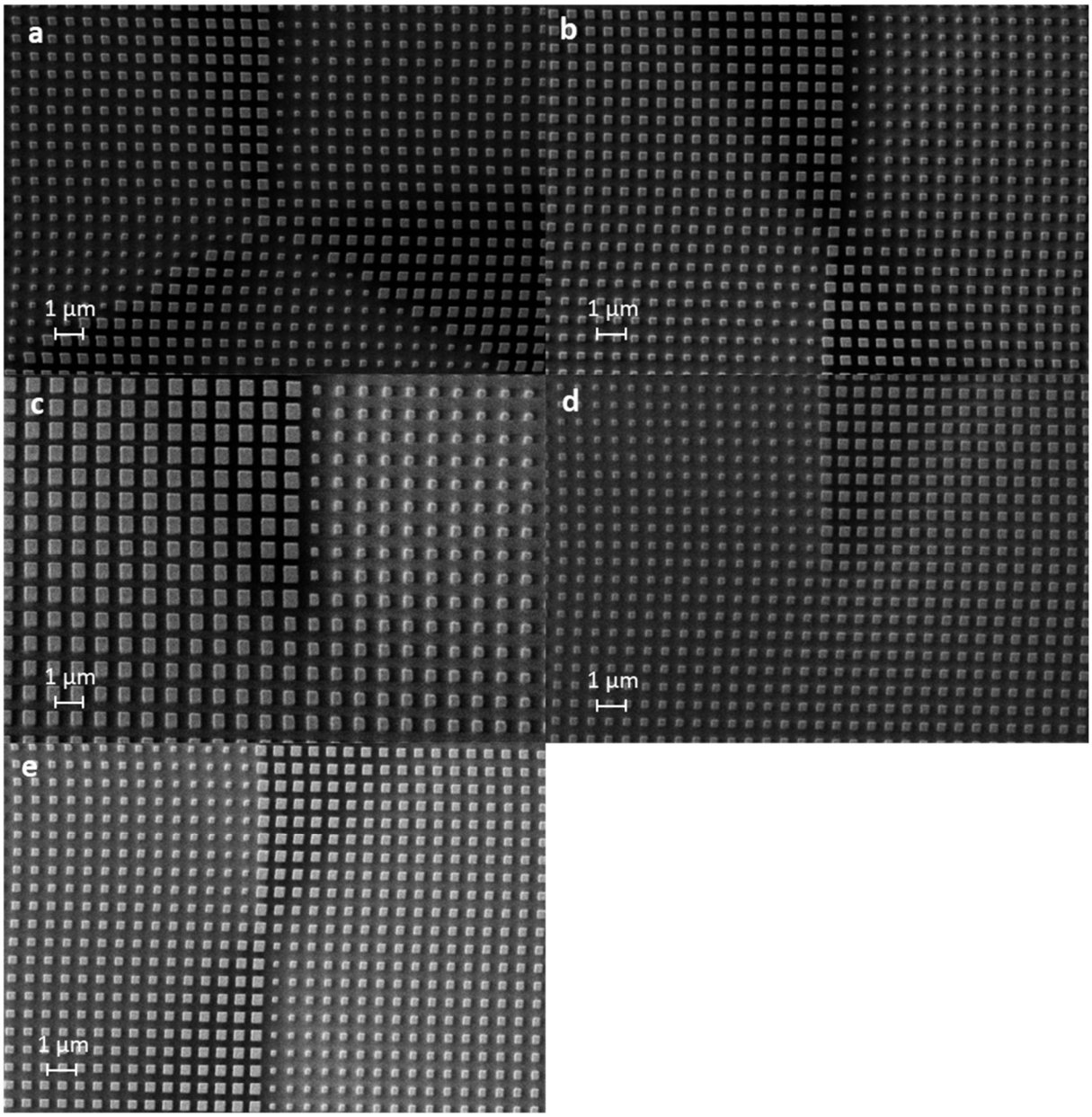

Figure 5.12 SEM images of an improved batch of the fabricated devices. The width of pillars ranges from $235\ nm$ to $420\ nm$. The topological charge of the devices in (a-e) ranges from -3 to 2, omitting 0.

5.4 Conclusion

To conclude, I have designed and fabricated three kinds of optical devices for generating vortex beams at $1550\ nm$ wavelength. The first device is a conventional integrated vortex beam generator. I have solved the problems of mask misalignment and undefined small gaps. In the second device, an enlarged grating coupler has been designed and fabricated to reduce the difficulty of fibre alignment and simplify the fabrication process. The last device is transmissive metasurfaces for OAM generation. Devices of high quality have been obtained. All these three types of devices can contribute to the goal of vortex beam generation.

Chapter 6 Conclusion and outlook

6.1 Conclusion

This thesis details my study of vortex beams that carry OAM. It contains two major pieces of simulation work as well as some preliminary experimental investigations.

In the first piece of simulation work, I have proposed and numerically demonstrated a novel approach for integrated vortex beam generation. This approach combines two well-established approaches, which are based respectively on metasurface-structured waveguides and angular grating-decorated microrings. This hybrid approach brings the conventional microring resonator a new topological charge tuning method, nanostructure-based OAM tuning. The use of Si pillar-based metasurfaces introduces an intrinsic phase gradient that is independent of the WGM inside the microring. As a result, the rotation direction of the source (i.e., the circulation of the WGM inside the microring) and that of the output (i.e., the helicity of the vortex beam) are decoupled, which is referred to as asymmetry vortex beam emission. It allows a single device to generate identical or two completely different sets of OAM values by only switching the input mode direction. This feature represents a new capability for integrated OAM emissions. The example device is capable of generating the same or two different OAM states at one resonance wavelength. For example, $l_+ = l_- = -8$ at $1600\,nm$ and $l_+ = -7,\ l_- = -9$ at $1627\,nm$. Furthermore, my collaborators and I have proposed a novel analytical method for extracting an OAM spectrum from a vector vortex beam. This method is based on approximating the vector vortex beam as a scalar vortex beam, followed by mode decomposition for this scalar vortex beam. The results fit with both the analytical prediction and the simulated field maps. We believe that both the hybridised design methodology and the OAM spectrum analysis method discussed here have substantial potential for advancing research on integrated vortex beam emission.

In the second piece of simulation work, I have studied and numerically tested a new metasurface design approach aimed at extracting a guided THz wave into free space and shaping its wavefront. This design utilises meta-atoms with a gradient in their light scattering amplitude, achieved by adjusting the gap size between the central waveguide and its side pillars. Unlike the commonly employed phase gradient design approach, this novel amplitude gradient design approach offers distinct advantages. As this approach can compensate for the energy decay in the energy feeding guided mode, a large number of meta-atoms can be accommodated along a single waveguide, as demonstrated in several 100- and 1000-unit devices. Consequently, I demonstrate three distinct off-chip wavefront shaping functionalities: (1) the generation of a plane wave, where the beam width can reach $275\lambda_0$, equivalently a factor above 900 in width

expansion; (2) the generation of a Bessel-beam focus with a FWHM of $0.59\lambda_0$; (3) the generation of OAM-carrying vortex beams, with tunable topological charges ranging from -5 to -30. These three light shaping functionalities demonstrated here could be used in a range of different applications, such as THz imaging [188], molecular sensing [189], and 6G communications [190]. All the meta-devices demonstrated here have a relatively straightforward configuration of the meta-atoms (all identical and evenly distributed) and the waveguide-pillar gap (changing at a constant step along the waveguide). More complicated configurations (e.g., obtained by incorporating methods such as inverse design [130]) could lead to other types of wavefront shaping and functionalities.

In my experimental work, I have designed and fabricated three different types of devices: a conventional integrated vortex beam emitter, a microring resonator using the monolithic fabrication method, and a transmissive metasurface for generating vortex beams. The conventional integrated emitter can serve as a test device for the asymmetric vortex beam emission discussed in Chapter 3. The second device was designed to simplify the fabrication process and the experimental measurement procedure. Due to the challenges in building the experiment setup, I decided to fabricate a transmissive metasurface, as it requires fewer optical components. All the devices have been successfully fabricated, as seen in the SEM images.

6.2 Future work

Further research is necessary to explore the potential application of integrated vortex beam emitters, particularly in LiDAR applications. Various design features can be investigated to enhance the performance of the emitter. For the asymmetric vortex beam emitter, the OAM purity of the emitted vortex beam and the emission efficiency can be improved. The following part will discuss future work related to the desired improvement of the vortex beam emitter.

To enhance the emission efficiency of the proposed asymmetric vortex beam emitter, several adjustments can be applied to the device: (1) an aluminum thin film can be placed under the integrated microring emitter to concentrate the main lobe of the emitted beams and reduce the side lobes intensity; (2) increasing the coupling efficiency of the microring through optimising the gap between the Si access waveguide and the microring waveguide; (3) reducing the bending loss of the microring by using a larger microring; and (4) optimising the thickness of the SiO_2 isolation layer to increase the emission efficiency.

List of References

1. L. Allen, M. W. Beijersbergen, R. J. C. Spreeuw, and J. P. Woerdman, "Orbital angular momentum of light and the transformation of Laguerre-Gaussian laser modes," Physical Review A **45**, 8185-8189 (1992).

2. Y. Ha, Y. Guo, M. Pu, X. Li, X. Ma, Z. Zhang, and X. Luo, "Monolithic - integrated multiplexed devices based on metasurface - driven guided waves," Advanced Theory and Simulations **4**, 2000239 (2021).

3. H. Huang, A. C. Overvig, Y. Xu, S. C. Malek, C.-C. Tsai, A. Alù, and N. Yu, "Leaky-wave metasurfaces for integrated photonics," Nat Nanotechnol, 1-9 (2023).

4. X. L. Cai, J. W. Wang, M. J. Strain, B. Johnson-Morris, J. B. Zhu, M. Sorel, J. L. O'Brien, M. G. Thompson, and S. T. Yu, "Integrated Compact Optical Vortex Beam Emitters," Science **338**, 363-366 (2012).

5. D. L. Andrews and M. Babiker, *The angular momentum of light*, pp. 1 online resource (xvi, 425 pages).

6. H. Pi, "Microring resonator for vortex beam emission and their all-optical wavelength tuning," (University of Southampton, 2021).

7. M. Krenn, J. Handsteiner, M. Fink, R. Fickler, R. Ursin, M. Malik, and A. Zeilinger, "Twisted light transmission over 143 km," Proceedings of the National Academy of Sciences **113**, 13648-13653 (2016).

8. Z. Wan, Y. Shen, Z. Wang, Z. Shi, Q. Liu, and X. Fu, "Divergence-degenerate spatial multiplexing towards future ultrahigh capacity, low error-rate optical communications," Light: Science & Applications **11**, 144 (2022).

9. X. Li, H. Ma, H. Zhang, M. Tang, H. Li, J. Tang, and Y. Wang, "Is it possible to enlarge the trapping range of optical tweezers via a single beam?," Applied Physics Letters **114**(2019).

10. P. Polimeno, A. Magazzu, M. A. Iati, F. Patti, R. Saija, C. D. E. Boschi, M. G. Donato, P. G. Gucciardi, P. H. Jones, and G. Volpe, "Optical tweezers and their applications," Journal of Quantitative Spectroscopy and Radiative Transfer **218**, 131-150 (2018).

11. F. Göttfert, C. A. Wurm, V. Mueller, S. Berning, V. C. Cordes, A. Honigmann, and S. W. Hell, "Coaligned dual-channel STED nanoscopy and molecular diffusion analysis at 20 nm resolution," Biophysical journal **105**, L01-L03 (2013).

12. T. Müller, C. Schumann, and A. Kraegeloh, "STED microscopy and its applications: new insights into cellular processes on the nanoscale," ChemPhysChem **13**, 1986-2000 (2012).

13. Ł. Płocinniczak, A. Popiołek-Masajada, J. Masajada, and M. Szatkowski, "Analytical model of the optical vortex microscope," Applied optics **55**, B20-B27 (2016).

14. F. Flamini, N. Spagnolo, and F. Sciarrino, "Photonic quantum information processing: a review," Reports on Progress in Physics **82**, 016001 (2018).

15. H. Lin, X. Wang, and Z. Yao, "Single photon orbital angular momentum transfer based on information processing technology," in *Journal of Physics: Conference Series*, (IOP Publishing, 2020), 012117.

16. M. Padgett and R. Bowman, "Tweezers with a twist," Nature Photonics **5**, 343-348 (2011).

17. S. P. P. a. M. W. Davidson, "The Stimulated Emission Depletion (STED) Concept", retrieved 2024, 03 Mar, https://zeiss-campus.magnet.fsu.edu/tutorials/superresolution/stedconcept/indexflash.html.

18. F. E. Mahmouli and S. D. Walker, "4-Gbps Uncompressed Video Transmission over a 60-GHz Orbital Angular Momentum Wireless Channel," IEEE Wireless Communications Letters **2**, 223-226 (2013).

19. G. A. Turnbull, D. A. Robertson, G. M. Smith, L. Allen, and M. J. Padgett, "The generation of free-space Laguerre-Gaussian modes at millimetre-wave frequencies by use of a spiral phaseplate," Optics Communications **127**, 183-188 (1996).

20. F. Tamburini, E. Mari, B. Thidé, C. Barbieri, and F. Romanato, "Experimental verification of photon angular momentum and vorticity with radio techniques," Applied Physics Letters **99**(2011).

21. J. Li, Y. Zhang, J. Li, X. Yan, L. Liang, Z. Zhang, J. Huang, J. Li, Y. Yang, and J. Yao, "Amplitude modulation of anomalously reflected terahertz beams using all-optical active Pancharatnam-Berry coding metasurfaces," Nanoscale **11**, 5746-5753 (2019).

22. S. X. Yu, L. Li, G. M. Shi, C. Zhu, X. X. Zhou, and Y. Shi, "Design, fabrication, and measurement of reflective metasurface for orbital angular momentum vortex wave in radio frequency domain," Applied Physics Letters **108**(2016).

23. S. Iqbal, J. Luo, Q. Ma, H. Rajabalipanah, M. S. Nisar, L. Zhang, A. Abdolali, and T. J. Cui, "Power modulation of vortex beams using phase/amplitude adjustable transmissive coding metasurfaces," Journal of Physics D: Applied Physics **54**(2020).

24. W. Luo, S. Sun, H.-X. Xu, Q. He, and L. Zhou, "Transmissive Ultrathin Pancharatnam-Berry Metasurfaces with nearly 100% Efficiency," Physical Review Applied **7**(2017).

25. S. Tang, T. Cai, J. G. Liang, Y. Xiao, C. W. Zhang, Q. Zhang, Z. Hu, and T. Jiang, "High-efficiency transparent vortex beam generator based on ultrathin Pancharatnam-Berry metasurfaces," Opt Express **27**, 1816-1824 (2019).

26. Y. Wang, K. Zhang, Y. Yuan, X. Ding, B. Ratni, S. N. Burokur, and Q. Wu, "Planar Vortex Beam Generator for Circularly Polarized Incidence Based on FSS," IEEE Transactions on Antennas and Propagation **68**, 1514-1522 (2020).

27. Q. Zheng, Y. Li, Y. Han, M. Feng, Y. Pang, J. Wang, H. Ma, S. Qu, and J. Zhang, "Efficient orbital angular momentum vortex beam generation by generalized coding metasurface," Applied Physics A **125**(2019).

28. W. Wang, Y. Li, Z. Y. Guo, R. Z. Li, J. R. Zhang, A. J. Zhang, and S. L. Qu, "Ultra-thin optical vortex phase plate based on the metasurface and the angular momentum transformation," Journal of Optics **17**(2015).

29. G. Yuan, S. Cao, P. Zhang, F. Peng, Z. Peng, and Z. Wang, "Achieving wide-range photonics applications based on a compact grating-assisted silicon micro-ring resonator," Optik **183**, 887-896 (2019).

30. Y. Sebbag and U. Levy, "Arbitrarily directed emission of integrated cylindrical vector vortex beams by geometric phase engineering," Opt Lett **45**, 6779-6782 (2020).

31. J. Zhang, C. Sun, B. Xiong, J. Wang, Z. Hao, L. Wang, Y. Han, H. Li, Y. Luo, Y. Xiao, C. Yu, T. Tanemura, Y. Nakano, S. Li, X. Cai, and S. Yu, "An InP-based vortex beam emitter with monolithically integrated laser," Nat Commun **9**, 2652 (2018).

32. S. M. Li, Y. H. Ding, X. W. Guan, H. Y. Tan, Z. C. Nong, L. Wang, L. Liu, L. D. Zhou, C. C. Yang, K. Yvind, L. K. Oxenlowe, S. Y. Yu, and X. L. Cai, "Compact high-efficiency vortex beam emitter based on a silicon photonics micro-ring," Opt Lett **43**, 1319-1322 (2018).

33. M. J. Strain, X. Cai, J. Wang, J. Zhu, D. B. Phillips, L. Chen, M. Lopez-Garcia, J. L. O'Brien, M. G. Thompson, M. Sorel, and S. Yu, "Fast electrical switching of orbital angular momentum modes using ultra-compact integrated vortex emitters," Nat Commun **5**, 4856 (2014).

34. S. A. Schulz, T. Machula, E. Karimi, and R. W. Boyd, "Integrated multi vector vortex beam generator," Opt Express **21**, 16130-16141 (2013).

35. H. Zhou, H. Song, Z. Zhao, R. Zhang, H. Song, K. Pang, K. Zou, C. Liu, X. Su, N. Hu, R. Bock, B. Lynn, M. Tur, and A. E. Willner, "Modal properties of a beam carrying OAM generated by a circular array of multiple ring-resonator emitters," Opt Lett **46**, 4722-4725 (2021).

36. D. M. Fatkhiev, V. S. Lyubopytov, R. V. Kutluyarov, A. K. Sultanov, V. A. Burdin, V. A. Andreev, O. G. Morozov, A. V. Bourdine, and A. H. Sultanov, "OAM signal emitter based on a ring resonator," in *Optical Technologies for Telecommunications 2019,* (2020).

37. S. Li, Z. Nong, X. Wu, W. Yu, M. He, C. Klitis, Y. Zhu, S. Gao, J. Liu, Z. Li, L. Liu, M. Sorel, S. Yu, and X. Cai, "Orbital angular momentum vector modes (de)multiplexer based on multimode micro-ring," Opt Express **26**, 29895-29905 (2018).

38. S. M. Li, Z. C. Nong, S. Q. Gao, M. B. He, L. Liu, S. Y. Yu, and X. L. Cai, "Orbital Angular Momentum Mode Multiplexer Based on Bilayer Concentric Micro-Ring Resonator," Asia Commun Photon (2017).

39. Z. Shao, J. Zhu, Y. Zhang, Y. Chen, and S. Yu, "On-chip switchable radially and azimuthally polarized vortex beam generation," Opt Lett **43**, 1263-1266 (2018).

40. Z. Shao, J. Zhu, Y. Chen, Y. Zhang, and S. Yu, "Spin-orbit interaction of light induced by transverse spin angular momentum engineering," Nat Commun **9**, 926 (2018).

41. Q. Xiao, C. Klitis, S. Li, Y. Chen, X. Cai, M. Sorel, and S. Yu, "Generation of photonic orbital angular momentum superposition states using vortex beam emitters with superimposed gratings," Opt Express **24**, 3168-3176 (2016).

42. T. Kundu, C. A. Rohde, C. J. Naify, M. D. Guild, T. P. Martin, J. S. Rogers, D. C. Calvo, and G. J. Orris, "Acoustic vortex beam generation using a compact metamaterial aperture," in *Health Monitoring of Structural and Biological Systems 2017,* (2017).

43. J. Zhu, X. Cai, Y. Chen, and S. Yu, "Theoretical model for angular grating-based integrated optical vortex beam emitters," Opt Lett **38**, 1343-1345 (2013).

44. I. V. Stepanov, D. M. Fatkhiev, V. S. Lyubopytov, R. V. Kutluyarov, E. P. Grakhova, N. Neumann, S. N. Khonina, and A. K. Sultanov, "Wavelength-Tunable Vortex Beam Emitter Based on Silicon Micro-Ring with PN Depletion Diode," Sensors-Basel **22**(2022).

45. R. Li, X. Feng, D. Zhang, K. Cui, F. Liu, and Y. Huang, "Radially Polarized Orbital Angular Momentum Beam Emitter Based on Shallow-Ridge Silicon Microring Cavity," IEEE Photonics Journal **6**, 1-10 (2014).

46. H. Pi, W. Yu, J. Yan, and X. Fang, "Coherent generation of arbitrary first-order Poincaré sphere beams on an Si chip," Optics Express **30**, 7342-7355 (2022).

47. G. Milione, H. Sztul, D. Nolan, and R. Alfano, "Higher-order Poincaré sphere, Stokes parameters, and the angular momentum of light," Physical review letters **107**, 053601 (2011).

48. A. R. Hippel, *Dielectrics and waves* (M.I.T. Press, Cambridge, Ma., 1966).

49. M.-C. Dicaire, "Generation of vortex beam superpositions using angular gratings," (Université d'Ottawa/University of Ottawa, 2017).

50. X. Liu, K. Fan, I. V. Shadrivov, and W. J. Padilla, "Experimental realization of a terahertz all-dielectric metasurface absorber," Opt Express **25**, 191-201 (2017).

51. W. Zhu, F. Xiao, I. D. Rukhlenko, J. Geng, X. Liang, M. Premaratne, and R. Jin, "Wideband visible-light absorption in an ultrathin silicon nanostructure," Opt Express **25**, 5781-5786 (2017).

52. S. Chen, H. Cheng, H. Yang, J. Li, X. Duan, C. Gu, and J. Tian, "Polarization insensitive and omnidirectional broadband near perfect planar metamaterial absorber in the near infrared regime," Applied physics letters **99**(2011).

53. Y. Yuan, K. Zhang, B. Ratni, Q. Song, X. Ding, Q. Wu, S. N. Burokur, and P. Genevet, "Independent phase modulation for quadruplex polarization channels enabled by chirality-assisted geometric-phase metasurfaces," Nature communications **11**, 4186 (2020).

54. Y. Kim, P. C. Wu, R. Sokhoyan, K. Mauser, R. Glaudell, G. Kafaie Shirmanesh, and H. A. Atwater, "Phase modulation with electrically tunable vanadium dioxide phase-change metasurfaces," Nano letters **19**, 3961-3968 (2019).

55. O. Buchnev, N. Podoliak, K. Kaltenecker, M. Walther, and V. A. Fedotov, "Metasurface-based optical liquid crystal cell as an ultrathin spatial phase modulator for THz applications," ACS Photonics **7**, 3199-3206 (2020).

56. Z. Yue, J. Liu, J. Li, J. Li, C. Zheng, G. Wang, M. Chen, H. Xu, Q. Wang, and X. Xing, "Multifunctional terahertz metasurfaces for polarization transformation and wavefront manipulation," Nanoscale **13**, 14490-14496 (2021).

57. M. I. Khan, Z. Khalid, and F. A. Tahir, "Linear and circular-polarization conversion in X-band using anisotropic metasurface," Scientific reports **9**, 4552 (2019).

58. P. Yu, J. Li, and N. Liu, "Electrically tunable optical metasurfaces for dynamic polarization conversion," Nano Letters **21**, 6690-6695 (2021).

59. S. Y. Chang, X. X. Guo, and X. J. Ni, "Optical Metasurfaces: Progress and Applications," Annu Rev Mater Res **48**, 279-302 (2018).

60. Z. Y. Li, M. H. Kim, C. Wang, Z. H. Han, S. Shrestha, A. C. Overvig, M. Lu, A. Stein, A. M. Agarwal, M. Loncar, and N. F. Yu, "Controlling propagation and coupling of waveguide modes using phase-gradient metasurfaces," Nat Nanotechnol **12**, 675-+ (2017).

61. S. L. Sun, K. Y. Yang, C. M. Wang, T. K. Juan, W. T. Chen, C. Y. Liao, Q. He, S. Y. Xiao, W. T. Kung, G. Y. Guo, L. Zhou, and D. P. Tsai, "High-Efficiency Broadband Anomalous Reflection by Gradient Meta-Surfaces," Nano Lett **12**, 6223-6229 (2012).

62. N. F. Yu, P. Genevet, M. A. Kats, F. Aieta, J. P. Tetienne, F. Capasso, and Z. Gaburro, "Light Propagation with Phase Discontinuities: Generalized Laws of Reflection and Refraction," Science **334**, 333-337 (2011).

63. X. J. Ni, S. Ishii, A. V. Kildishev, and V. M. Shalaev, "Ultra-thin, planar, Babinet-inverted plasmonic metalenses," Light-Sci Appl **2**(2013).

64. E. Maguid, I. Yulevich, M. Yannai, V. Kleiner, M. L Brongersma, and E. Hasman, "Multifunctional interleaved geometric-phase dielectric metasurfaces," Light: Science & Applications **6**, e17027-e17027 (2017).

65. E. Hasman, V. Kleiner, G. Biener, and A. Niv, "Polarization dependent focusing lens by use of quantized Pancharatnam–Berry phase diffractive optics," Applied physics letters **82**, 328-330 (2003).

66. Y. Qiu, S. Tang, T. Cai, H. Xu, and F. Ding, "Fundamentals and applications of spin-decoupled Pancharatnam—Berry metasurfaces," Frontiers of Optoelectronics **14**, 134-147 (2021).

67. Z. Zhou, J. Li, R. Su, B. Yao, H. Fang, K. Li, L. Zhou, J. Liu, D. Stellinga, C. P. Reardon, T. F. Krauss, and X. Wang, "Efficient Silicon Metasurfaces for Visible Light," ACS Photonics **4**, 544-551 (2017).

68. M. Khorasaninejad, W. T. Chen, R. C. Devlin, J. Oh, A. Y. Zhu, and F. Capasso, "Metalenses at visible wavelengths: Diffraction-limited focusing and subwavelength resolution imaging," Science **352**, 1190-1194 (2016).

69. J. Li, T. Wu, W. Xu, Y. Liu, C. Liu, Y. Wang, Z. Yu, D. Zhu, L. Yu, and H. Ye, "Mechanisms of 2pi phase control in dielectric metasurface and transmission enhancement effect," Opt Express **27**, 23186-23196 (2019).

70. F. J. Bezares, J. P. Long, O. J. Glembocki, J. Guo, R. W. Rendell, R. Kasica, L. Shirey, J. C. Owrutsky, and J. D. Caldwell, "Mie resonance-enhanced light absorption in periodic silicon nanopillar arrays," Opt. Express **21**, 27587-27601 (2013).

71. Q. Zhao, J. Zhou, F. Zhang, and D. Lippens, "Mie resonance-based dielectric metamaterials," Materials today **12**, 60-69 (2009).

72. F. He, K. F. MacDonald, and X. Fang, "Coherent illumination spectroscopy of nanostructures and thin films on thick substrates," Opt. Express **26**, 12415-12423 (2018).

73. F. He, K. F. MacDonald, and X. Fang, "Continuous beam steering by coherent light-by-light control of dielectric metasurface phase gradient," Opt. Express **28**, 30107-30116 (2020).

74. W.-Q. Chen, D.-S. Zhang, S.-Y. Long, Z.-Z. Liu, and J.-J. Xiao, "Nearly dispersionless multicolor metasurface beam deflector for near eye display designed by a physics-driven deep neural network," Applied Optics **60**, 3947-3953 (2021).

75. N. Li, Y. H. Fu, Y. Dong, T. Hu, Z. Xu, Q. Zhong, D. Li, K. H. Lai, S. Zhu, and Q. Lin, "Large-area pixelated metasurface beam deflector on a 12-inch glass wafer for random point generation," Nanophotonics **8**, 1855-1861 (2019).

76. S. Chen, J. Huang, S. Yin, M. M. Milosevic, H. Pi, J. Yan, H. M. H. Chong, and X. Fang, "Metasurfaces integrated with a single-mode waveguide array for off-chip wavefront shaping," Opt. Express **31**, 15876-15887 (2023).

77. X. Zhang, R. Deng, F. Yang, C. Jiang, S. Xu, and M. Li, "Metasurface-based ultrathin beam splitter with variable split angle and power distribution," ACS photonics **5**, 2997-3002 (2018).

78. J. Li, H. Ye, T. Wu, Y. Liu, Z. Yu, Y. Wang, Y. Sun, and L. Yu, "Ultra-broadband large-angle beam splitter based on a homogeneous metasurface at visible wavelengths," Opt Express **28**, 32226-32238 (2020).

79. H. Zeng, Y. Zhang, F. Lan, S. Liang, L. Wang, T. Song, T. Zhang, Z. Shi, Z. Yang, and X. Kang, "Terahertz dual-polarization beam splitter via an anisotropic matrix metasurface," IEEE Transactions on Terahertz Science and Technology **9**, 491-497 (2019).

80. H. Yang, K. Ou, G. Cao, X. Shang, Y. Liu, and Y. Deng, "Polarization beam splitter with disparate functionality in transmission and reflection modes," Optics Communications **443**, 104-109 (2019).

81. J. Li, C. Liu, T. Wu, Y. Liu, Y. Wang, Z. Yu, H. Ye, and L. Yu, "Efficient polarization beam splitter based on all-dielectric metasurface in visible region," Nanoscale Research Letters **14**, 1-7 (2019).

82. R. Mao, G. Wang, T. Cai, K. Liu, D. Wang, and B. Wu, "Ultra-thin and high-efficiency full-space Pancharatnam-Berry metasurface," Opt Express **28**, 31216-31225 (2020).

83. M. Khorasaninejad and K. B. Crozier, "Silicon nanofin grating as a miniature chirality-distinguishing beam-splitter," Nature communications **5**, 5386 (2014).

84. S. Kuznetsov, V. Lenets, M. Tumashov, A. Sayanskiy, P. Lazorskiy, P. Belov, J. Baena, and S. Glybovski, "Self-complementary metasurfaces for designing terahertz deflecting circular-polarization beam splitters," Applied Physics Letters **118**(2021).

85. W. T. Chen, A. Y. Zhu, V. Sanjeev, M. Khorasaninejad, Z. Shi, E. Lee, and F. Capasso, "A broadband achromatic metalens for focusing and imaging in the visible," Nature nanotechnology **13**, 220-226 (2018).

86. Q. Cheng, M. Ma, D. Yu, Z. Shen, J. Xie, J. Wang, N. Xu, H. Guo, W. Hu, and S. Wang, "Broadband achromatic metalens in terahertz regime," Science Bulletin **64**, 1525-1531 (2019).

87. M. Wang, J. S. Lee, S. Aggarwal, N. Farmakidis, Y. He, T. Cheng, and H. Bhaskaran, "Varifocal Metalens Using Tunable and Ultralow - loss Dielectrics," Advanced Science **10**, 2204899 (2023).

88. F. He, Y. Feng, H. Pi, J. Yan, K. F. MacDonald, and X. Fang, "Coherently switching the focusing characteristics of all-dielectric metalenses," Opt. Express **30**, 27683-27693 (2022).

89. D. Ohana, B. Desiatov, N. Mazurski, and U. Levy, "Dielectric metasurface as a platform for spatial mode conversion in nanoscale waveguides," Nano letters **16**, 7956-7961 (2016).

90. L. Huang, S. Zhang, and T. Zentgraf, "Metasurface holography: from fundamentals to applications," Nanophotonics **7**, 1169-1190 (2018).

91. P. Genevet and F. Capasso, "Holographic optical metasurfaces: a review of current progress," Reports on Progress in Physics **78**, 024401 (2015).

92. X. Hong, S. Feng, H. Guo, and C. Li, "A beam deflector with dielectric metasurfaces in the terahertz region," Laser Physics **30**, 016204 (2019).

93. M. Khorasaninejad, Z. Shi, A. Y. Zhu, W.-T. Chen, V. Sanjeev, A. Zaidi, and F. Capasso, "Achromatic metalens over 60 nm bandwidth in the visible and metalens with reverse chromatic dispersion," Nano letters **17**, 1819-1824 (2017).

94. G. Zheng, H. Mühlenbernd, M. Kenney, G. Li, T. Zentgraf, and S. Zhang, "Metasurface holograms reaching 80% efficiency," Nature nanotechnology **10**, 308-312 (2015).

95. W. Wan, J. Gao, and X. Yang, "Full-Color Plasmonic Metasurface Holograms," ACS Nano **10**, 10671-10680 (2016).

96. Y. A. Vlasov and S. J. McNab, "Losses in single-mode silicon-on-insulator strip waveguides and bends," Opt. Express **12**, 1622-1631 (2004).

97. X. J. Xu, S. W. Chen, J. Z. Yu, and X. G. Tu, "An investigation of the mode characteristics of SOI submicron rib waveguides using the film mode matching method," J Opt a-Pure Appl Op **11**(2009).

98. B. Vinter, E. Rosencher, and P. G. Piva, "Waveguides," in *Optoelectronics* (Cambridge University Press, Cambridge, 2002), pp. 396-413.

99. W. Bogaerts, P. De Heyn, T. Van Vaerenbergh, K. De Vos, S. K. Selvaraja, T. Claes, P. Dumon, P. Bienstman, D. Van Thourhout, and R. Baets, "Silicon microring resonators," Laser Photonics Rev **6**, 47-73 (2012).

100. I. Demirtzioglou, C. Lacava, K. R. Bottrill, D. J. Thomson, G. T. Reed, D. J. Richardson, and P. Petropoulos, "Frequency comb generation in a silicon ring resonator modulator," Opt. Express **26**, 790-796 (2018).

101. F. He, K. F. MacDonald, and X. Fang, "Continuous beam steering by coherent light-by-light control of dielectric metasurface phase gradient," Opt. Express **28**, 30107-30116 (2020).

102. Z. Li, C. W. Wan, C. J. Dai, J. Zhang, G. X. Zheng, and Z. Y. Li, "Actively Switchable Beam-Steering via Hydrophilic/Hydrophobic-Selective Design of Water-Immersed Metasurface," Adv Opt Mater **9**, 2100297 (2021).

103. K. Koshelev, S. Lepeshov, M. Liu, A. Bogdanov, and Y. Kivshar, "Asymmetric Metasurfaces with High-Q Resonances Governed by Bound States in the Continuum," Phys. Rev. Lett. **121**, 193903 (2018).

104. Y. Zhou, Z. H. Guo, X. Y. Zhao, F. L. Wang, Z. Y. Yu, Y. Z. Chen, Z. R. Liu, S. Y. Zhang, S. L. Sun, and X. Wu, "Dual-Quasi Bound States in the Continuum Enabled Plasmonic Metasurfaces," Adv Opt Mater **10**, 2200965 (2022).

105. Y. C. Zhang, J. Gao, and X. D. Yang, "Optical Vortex Transmutation with Geometric Metasurfaces of Rotational Symmetry Breaking," Adv Opt Mater **7**, 1901152 (2019).

106. Y. T. Tang, Z. G. Liu, J. H. Deng, K. F. Li, J. F. Li, and G. X. Li, "Nano-Kirigami Metasurface with Giant Nonlinear Optical Circular Dichroism," Laser Photon Rev **14**, 2000085 (2020).

107. B. Y. Liu, B. Sain, B. Reineke, R. Z. Zhao, C. Meier, L. L. Huang, Y. Y. Jiang, and T. Zentgraf, "Nonlinear Wavefront Control by Geometric-Phase Dielectric Metasurfaces: Influence of Mode Field and Rotational Symmetry," Adv Opt Mater **8**, 1902050 (2020).

108. R. C. Devlin, A. Ambrosio, N. A. Rubin, J. B. Mueller, and F. Capasso, "Arbitrary spin-to–orbital angular momentum conversion of light," Science **358**, 896-901 (2017).

109. H. Sroor, Y.-W. Huang, B. Sephton, D. Naidoo, A. Vallés, V. Ginis, C.-W. Qiu, A. Ambrosio, F. Capasso, and A. Forbes, "High-purity orbital angular momentum states from a visible metasurface laser," Nature Photonics **14**, 498-503 (2020).

110. X. Guo, Y. Ding, X. Chen, Y. Duan, and X. Ni, "Molding free-space light with guided wave–driven metasurfaces," Sci Adv **6**, eabb4142 (2020).

111. Z. Zhang, X. Qiao, B. Midya, K. Liu, J. Sun, T. Wu, W. Liu, R. Agarwal, J. M. Jornet, and S. Longhi, "Tunable topological charge vortex microlaser," Science **368**, 760-763 (2020).

112. Z. Qiao, Z. Yuan, S. Zhu, C. Gong, Y. Liao, X. Gong, M. Kim, D. Zhang, and Y.-C. Chen, "High orbital angular momentum lasing with tunable degree of chirality in a symmetry-broken microcavity," Optica **10**, 846-853 (2023).

113. A. E. Willner, Y. Ren, G. Xie, Y. Yan, L. Li, Z. Zhao, J. Wang, M. Tur, A. F. Molisch, and S. Ashrafi, "Recent advances in high-capacity free-space optical and radio-frequency communications using orbital angular momentum multiplexing," Philosophical Transactions of the Royal Society A: Mathematical, Physical and Engineering Sciences **375**, 20150439 (2017).

114. C. He, Y. Shen, and A. Forbes, "Towards higher-dimensional structured light," Light: Science & Applications **11**, 205 (2022).

115. D. Gao, W. Ding, M. Nieto-Vesperinas, X. Ding, M. Rahman, T. Zhang, C. Lim, and C.-W. Qiu, "Optical manipulation from the microscale to the nanoscale: fundamentals, advances and prospects," Light: Science & Applications **6**, e17039-e17039 (2017).

116. S. Yin, F. He, W. Kubo, Q. Wang, J. Frame, N. G. Green, and X. Fang, "Coherently tunable metalens tweezers for optofluidic particle routing," Opt Express **28**, 38949-38959 (2020).

117. T. Li, X. Xu, B. Fu, S. Wang, B. Li, Z. Wang, and S. Zhu, "Integrating the optical tweezers and spanner onto an individual single-layer metasurface," Photonics Research **9**, 1062-1068 (2021).

118. Z. Shen, Z. Xiang, Z. Wang, Y. Shen, and B. Zhang, "Optical spanner for nanoparticle rotation with focused optical vortex generated through a Pancharatnam–Berry phase metalens," Applied Optics **60**, 4820-4826 (2021).

119. Z. Liu, X. Zhou, X. Jia, Y. Wang, W. Zheng, and Z. Wang, "Visible light perovskite-coated photonic crystal surface-emitter on SOI," Semiconductor Science and Technology **35**, 075019 (2020).

120. J. Liao, Y. Tan, Y. Gao, Z. Wang, Y. Sun, L. Ma, and X. Li, "Giant anomalous self-steepening and temporal soliton compression in silicon photonic crystal waveguides," APL Photonics **6**(2021).

121. C. Yao, Y. Wang, J. Zhang, X. Zhang, C. Zhao, B. Wang, S. C. Singh, and C. Guo, "Dielectric nanoaperture metasurfaces in silicon waveguides for efficient and broadband mode conversion with an ultrasmall footprint," Advanced Optical Materials **8**, 2000529 (2020).

122. X. Zhang, J. Li, J. F. Donegan, and A. L. Bradley, "Constructive and destructive interference of Kerker-type scattering in an ultrathin silicon Huygens metasurface," Physical Review Materials **4**, 125202 (2020).

123. J. Zhang, P. Nuño Ruano, X. Le-Roux, M. Montesinos-Ballester, D. Marris-Morini, E. Cassan, L. Vivien, N. D. Lanzillotti-Kimura, and C. A. Ramos, "Subwavelength control of photons and phonons in release-free silicon optomechanical resonators," ACS Photonics **9**, 3855-3862 (2022).

124. K. Pelka, G. Madiot, R. Braive, and A. Xuereb, "Floquet control of optomechanical bistability in multimode systems," Physical Review Letters **129**, 123603 (2022).

125. C. Huang, S. Bilodeau, T. Ferreira de Lima, A. N. Tait, P. Y. Ma, E. C. Blow, A. Jha, H.-T. Peng, B. J. Shastri, and P. R. Prucnal, "Demonstration of scalable microring weight bank control for large-scale photonic integrated circuits," APL Photonics **5**(2020).

126. C. Lian, C. Vagionas, T. Alexoudi, N. Pleros, N. Youngblood, and C. Ríos, "Photonic (computational) memories: tunable nanophotonics for data storage and computing," Nanophotonics **11**, 3823-3854 (2022).

127. H. Pi, T. Rahman, S. A. Boden, T. Ma, J. Yan, and X. Fang, "Integrated vortex beam emitter in the THz frequency range: Design and simulation," APL Photonics **5**(2020).

128. L. Massai, T. Schatteburg, J. P. Home, and K. K. Mehta, "Pure circularly polarized light emission from waveguide microring resonators," Applied Physics Letters **121**(2022).

129. X. Lu, M. Wang, F. Zhou, M. Heuck, W. Zhu, V. A. Aksyuk, D. R. Englund, and K. Srinivasan, "Highly-twisted states of light from a high quality factor photonic crystal ring," Nature Communications **14**, 1119 (2023).

130. S. So, J. Mun, J. Park, and J. Rho, "Revisiting the design strategies for metasurfaces: fundamental physics, optimization, and beyond," Advanced Materials **35**, 2206399 (2023).

131. P.-Y. Hsieh, S.-L. Fang, Y.-S. Lin, W.-H. Huang, J.-M. Shieh, P. Yu, and Y.-C. Chang, "Integrated metasurfaces on silicon photonics for emission shaping and holographic projection," Nanophotonics **11**, 4687-4695 (2022).

132. E. D. Palik, *Handbook of optical constants of solids* (Academic press, 1998), Vol. 3.

133. H. Rubinsztein-Dunlop, A. Forbes, M. V. Berry, M. R. Dennis, D. L. Andrews, M. Mansuripur, C. Denz, C. Alpmann, P. Banzer, and T. Bauer, "Roadmap on structured light," Journal of Optics **19**, 013001 (2016).

134. Y. Shen, X. Wang, Z. Xie, C. Min, X. Fu, Q. Liu, M. Gong, and X. Yuan, "Optical vortices 30 years on: OAM manipulation from topological charge to multiple singularities," Light: Science & Applications **8**, 90 (2019).

135. S. Franke - Arnold, L. Allen, and M. Padgett, "Advances in optical angular momentum," Laser & Photonics Reviews **2**, 299-313 (2008).

136. R. Wang, Q. Wu, W. Cai, Q. Zhang, H. Xiong, B. Zhang, J. Qi, J. Yao, and J. Xu, "Broadband on-Chip Terahertz Asymmetric Waveguiding via Phase-Gradient Metasurface," ACS Photonics **6**, 1774-1779 (2019).

137. L. F. Herrán, A. Algaba Brazalez, and E. Rajo-Iglesias, "Ka-band planar slotted waveguide array based on groove gap waveguide technology with a glide-symmetric holey metasurface," Scientific Reports **11**, 8697 (2021).

138. Y. Ding, X. Chen, Y. Duan, H. Huang, L. Zhang, S. Chang, X. Guo, and X. Ni, "Metasurface-Dressed Two-Dimensional on-Chip Waveguide for Free-Space Light Field Manipulation," ACS Photonics **9**, 398-404 (2022).

139. J. He, M. Wan, X. Zhang, S. Yuan, L. Zhang, and J. Wang, "Generating ultraviolet perfect vortex beams using a high-efficiency broadband dielectric metasurface," Opt Express **30**, 4806-4816 (2022).

140. Y. Kan, R. Yang, A. Zhang, Z. Lei, Y. Jiao, and J. Li, "Meta-Surface Cavity-Based Waveguide Slot Array for Dual-Circularly Polarized Dual Beam," IEEE Transactions on Antennas and Propagation **70**, 3894-3898 (2022).

141. H. Lu, B. Zheng, T. Cai, C. Qian, Y. Yang, Z. Wang, and H. Chen, "Frequency-Controlled Focusing Using Achromatic Metasurface," Advanced Optical Materials **9**, 2001311 (2021).

142. J. Wang, Y. Cheng, H. Luo, F. Chen, and L. Wu, "High-gain bidirectional radiative circularly polarized antenna based on focusing metasurface," AEU - International Journal of Electronics and Communications **151**, 154222 (2022).

143. Y. Chen, R. Zhao, H. He, X. Li, H. Zhou, N. Ullah, G. Geng, J. Li, Y. Wang, and L. Huang, "Spectrum dispersion element based on the metasurface with parabolic phase," Opt Express **30**, 32670-32679 (2022).

144. M. I. Shalaev, J. B. Sun, A. Tsukernik, A. Pandey, K. Nikolskiy, and N. M. Litchinitser, "High-Efficiency All-Dielectric Metasurfaces for Ultracompact Beam Manipulation in Transmission Mode," Nano Lett. **15**, 6261-6266 (2015).

145. Y. Q. Hu, L. Li, Y. J. Wang, M. Meng, L. Jin, X. H. Luo, Y. Q. Chen, X. Li, S. M. Xiao, H. B. Wang, Y. Luo, C. W. Qiu, and H. G. Duan, "Trichromatic and Tripolarization-Channel Holography with Noninterleaved Dielectric Metasurface," Nano Lett. **20**, 994-1002 (2020).

146. Y. Y. Shi, C. W. Wan, C. J. Dai, Z. J. Wang, S. Wan, G. X. Zheng, S. Zhang, and Z. Y. Li, "Augmented Reality Enabled by On-Chip Meta-Holography Multiplexing," Laser Photon. Rev. **16**(2022).

147. S. Sun, Q. He, J. Hao, S. Xiao, and L. Zhou, "Electromagnetic metasurfaces: physics and applications," Adv. Opt. Photonics **11**, 380 (2019).

148. M. Decker, I. Staude, M. Falkner, J. Dominguez, D. N. Neshev, I. Brener, T. Pertsch, and Y. S. Kivshar, "High-Efficiency Dielectric Huygens' Surfaces," Adv. Opt. Mater. **3**, 813-820 (2015).

149. Y. F. Yu, A. Y. Zhu, R. Paniagua-Dominguez, Y. H. Fu, B. Luk'yanchuk, and A. I. Kuznetsov, "High-transmission dielectric metasurface with 2 phase control at visible wavelengths," Laser Photon. Rev. **9**, 412-418 (2015).

150. J. Li, T. S. Wu, W. B. Xu, Y. M. Liu, C. Liu, Y. Wang, Z. Y. Yu, D. F. Zhu, L. Yu, and H. Ye, "Mechanisms of 2 pi phase control in dielectric metasurface and transmission enhancement effect," Opt. Express **27**, 23186-23196 (2019).

151. P. Lalanne and P. Chavel, "Metalenses at visible wavelengths: past, present, perspectives," Laser Photon. Rev. **11**, 1600295 (2017).

152. X. J. Ni, A. V. Kildishev, and V. M. Shalaev, "Metasurface holograms for visible light," Nat. Commun. **4**(2013).

153. G. Y. Lee, G. Yoon, S. Y. Lee, H. Yun, J. Cho, K. Lee, H. Kim, J. Rho, and B. Lee, "Complete amplitude and phase control of light using broadband holographic metasurfaces," Nanoscale **10**, 4237-4245 (2018).

154. A. C. Overvig, S. Shrestha, S. C. Malek, M. Lu, A. Stein, C. X. Zheng, and N. F. Yu, "Dielectric metasurfaces for complete and independent control of the optical amplitude and phase," Light-Sci. Appl. **8**(2019).

155. H. R. Ren, X. Y. Fang, J. Jang, J. Burger, J. Rho, and S. A. Maier, "Complex-amplitude metasurface-based orbital angular momentum holography in momentum space," Nature Nanotechnology **15**, 948-+ (2020).

156. J. Zhang, X. Z. Wei, I. D. Rukhlenko, H. T. Chen, and W. R. Zhu, "Electrically Tunable Metasurface with Independent Frequency and Amplitude Modulations," ACS Photonics **7**, 265-271 (2020).

157. C. L. Zheng, J. Li, Z. Yue, J. T. Li, J. Y. Liu, G. C. Wang, S. L. Wang, Y. T. Zhang, Y. Zhang, and J. Q. Yao, "All-Dielectric Trifunctional Metasurface Capable of Independent Amplitude and Phase Modulation," Laser Photon. Rev. **16**(2022).

158. H.-T. Chen, A. J. Taylor, and N. Yu, "A review of metasurfaces: physics and applications," Reports on Progress in Physics **79**(2016).

159. Y. Meng, Y. Z. Chen, L. H. Lu, Y. M. Ding, A. Cusano, J. A. Fan, Q. M. Hu, K. Y. Wang, Z. W. Xie, Z. T. Liu, Y. M. Yang, Q. Liu, M. L. Gong, Q. R. Xiao, S. L. Sun, M. M. Zhang, X. C. Yuan,

and X. J. Ni, "Optical meta-waveguides for integrated photonics and beyond," Light-Sci. Appl. **10**(2021).

160. Y. Y. Shi, C. W. Wan, C. J. Dai, S. Wan, Y. Liu, C. Zhang, and Z. Y. Li, "On-chip meta-optics for semi-transparent screen display in sync with AR projection," Optica **9**, 670-676 (2022).

161. A. Yulaev, W. Zhu, C. Zhang, D. A. Westly, H. J. Lezec, A. Agrawal, and V. Aksyuk, "Metasurface-Integrated Photonic Platform for Versatile Free-Space Beam Projection with Polarization Control," ACS Photonics **6**, 2902-+ (2019).

162. Z. Xie, T. Lei, F. Li, H. Qiu, Z. Zhang, H. Wang, C. Min, L. Du, Z. Li, and X. Yuan, "Ultra-broadband on-chip twisted light emitter for optical communications," Light-Sci. Appl. **7**(2018).

163. G. B. Wu, S. Y. Zhu, S. W. Pang, and C. H. Chan, "Superheterodyne-inspired waveguide-integrated metasurfaces for flexible free-space light manipulation," Nanophotonics **11**, 4499-4514 (2022).

164. X. X. Guo, Y. M. Ding, X. Chen, Y. Duan, and X. J. Ni, "Molding free-space light with guided wave-driven metasurfaces," Sci Adv **6**(2020).

165. C. K. Xie, L. R. Huang, W. B. Liu, W. Hong, J. F. Ding, W. Wu, and M. Guo, "Bifocal focusing and polarization demultiplexing by a guided wave-driven metasurface," Opt. Express **29**, 25709-25719 (2021).

166. B. Fang, Z. Z. Wang, S. L. Gao, S. N. Zhu, and T. Li, "Manipulating guided wave radiation with integrated geometric metasurface," Nanophotonics **11**, 1923-1930 (2022).

167. K. L. Xi, B. Fang, L. Ding, L. Li, S. L. Zhuang, and Q. Q. Cheng, "Terahertz Airy beam generated by Pancharatnam-Berry phases in guided wave-driven metasurfaces," Opt. Express **30**, 16699-16711 (2022).

168. R. Yang, S. Wan, Y. Y. Shi, Z. J. Wang, J. Tang, and Z. Y. Li, "Immersive Tuning the Guided Waves for Multifunctional On-Chip Metaoptics," Laser Photon. Rev. **16**(2022).

169. J. M. Liu, X. Fang, F. He, S. Q. Yin, W. Lyu, H. Geng, X. J. Deng, and X. P. Zheng, "Directional conversion of a THz propagating wave into surface waves in deformable metagratings," Opt. Express **29**, 21749-21762 (2021).

170. W. Lyu, J. M. Liu, S. Q. Yin, X. J. Deng, X. Fang, H. Geng, and X. P. Zheng, "Deep-subwavelength gap modes in all-dielectric metasurfaces for high-efficiency and large-angle wavefront bending," Opt. Express **30**, 12080-12091 (2022).

171. J. M. Dai, J. Q. Zhang, W. L. Zhang, and D. Grischkowsky, "Terahertz time-domain spectroscopy characterization of the far-infrared absorption and index of refraction of high-resistivity, float-zone silicon," J. Opt. Soc. Am. B **21**, 1379-1386 (2004).

172. M. Naftaly and R. E. Miles, "Terahertz time-domain spectroscopy for material characterization," Proc. IEEE **95**, 1658-1665 (2007).

173. P. A. Anderson, B. S. Schmidt, and M. Lipson, "High confinement in silicon slot waveguides with sharp bends," Opt. Express **14**, 9197-9202 (2006).

174. W. K. Pan, Z. Wang, Y. Z. Chen, S. Q. Li, X. Y. Zheng, X. Z. Tian, C. Chen, N. X. Xu, Q. He, L. Zhou, and S. L. Sun, "High-efficiency generation of far-field spin-polarized wavefronts via designer surface wave metasurfaces," Nanophotonics **11**, 2025-2036 (2022).

175. J. W. Goodman, *Introduction to Fourier optics*, 3rd Ed. (Roberts & Company, Englewood, 2005).

176. J. Zhu, X. Cai, Y. Chen, and S. Yu, "Theoretical model for angular grating-based integrated optical vortex beam emitters," Opt. Lett. **38**, 1343-1345 (2013).

177. S. Li, Y. Ding, X. Guan, H. Tan, Z. Nong, L. Wang, L. Liu, L. Zhou, C. Yang, K. Yvind, L. K. Oxenlowe, S. Yu, and X. Cai, "Compact high-efficiency vortex beam emitter based on a silicon photonics micro-ring," Opt. Lett. **43**, 1319-1322 (2018).

178. Ritsch-Marte and Monika, "Orbital angular momentum light in microscopy," Philosophical transactions of the Royal Society. Mathematical, physical, and engineering sciences **375**(2017).

179. T. Omatsu, K. Miyamoto, K. Toyoda, R. Morita, Y. Arita, and K. Dholakia, "A New Twist for Materials Science: The Formation of Chiral Structures Using the Angular Momentum of Light," Adv. Opt. Mater. **7**, 1801672 (2019).

180. A. Kritzinger, A. Forbes, and P. B. C. Forbes, "Optical trapping and fluorescence control with vectorial structured light," Sci Rep **12**, 17690 (2022).

181. S. Liu, Y. Lou, and J. Jing, "Orbital angular momentum multiplexed deterministic all-optical quantum teleportation," Nat. Commun. **11**, 3875 (2020).

182. X. Wang, Z. Nie, Y. Liang, J. Wang, T. Li, and B. Jia, "Recent advances on optical vortex generation," Nanophotonics **7**, 1533-1556 (2018).

183. Y. Jiang, Y. Cao, and X. Feng, "Progress in integrated devices for optical vortex emission," J. Phys. D-Appl. Phys. **53**(2020).

184. H. L. Pi, W. K. Yu, J. Z. Yan, and X. Fang, "Coherent generation of arbitrary first-order Poincare sphere beams on an Si chip," Opt. Express **30**, 7342-7355 (2022).

185. H. Zhang, J. Zeng, X. Lu, Z. Wang, C. Zhao, and Y. Cai, "Review on fractional vortex beam," Nanophotonics **11**, 241-273 (2022).

186. M. Henry, S. Walavalkar, A. Homyk, and A. Scherer, "Alumina etch masks for fabrication of high-aspect-ratio silicon micropillars and nanopillars," Nanotechnology **20**, 255305 (2009).

187. J. Parasuraman, A. Summanwar, F. Marty, P. Basset, D. E. Angelescu, and T. Bourouina, "Deep reactive ion etching of sub-micrometer trenches with ultra high aspect ratio," Microelectronic engineering **113**, 35-39 (2014).

188. W. Y. Liu, Q. L. Yang, Q. Xu, X. H. Jiang, T. Wu, K. M. Wang, J. Q. Gu, J. G. Han, and W. L. Zhang, "Multifunctional All-Dielectric Metasurfaces for Terahertz Multiplexing," Adv. Opt. Mater. **9**(2021).

189. X. Y. Liu, W. Chen, Y. J. Ma, Y. N. Xie, J. Zhou, L. G. Zhu, Y. D. Xu, and J. F. Zhu, "Enhancing THz fingerprint detection on the planar surface of an inverted dielectric metagrating," Photonics Research **10**, 2836-2845 (2022).

190. W. Tang, M. Z. Chen, J. Y. Dai, Y. Zeng, X. Zhao, S. Jin, Q. Cheng, and T. J. Cui, "Wireless Communications with Programmable Metasurface: New Paradigms, Opportunities, and Challenges on Transceiver Design," Ieee Wireless Communications **27**, 180-187 (2020).

191. CORNERSTONE, "CORNERSTONE STANDARD COMPONENTS LIBRARY", retrieved 03 Nov, 2022, https://www.cornerstone.sotonfab.co.uk/download?download=247:cornerstone-soi-standard-components-library-feb-2022.